APPLICATION OF COMPUTATIONAL FLUID DYNAMICS TO DECOMPRESSION MODELING OF CARBON DIOXIDE PIPELINES

A Dissertation

by

LEIDY TATIANA FLECHAS MORENO

Submitted to the Office of Graduate and Professional Studies of
Texas A&M University
in partial fulfillment of the requirements for the degree of

DOCTOR OF PHILOSOPHY

Chair of Committee,	Charles J. Glover
Committee Members,	James Holste
	Ioannis Economou
	Hamn C. Chen
Head of Department,	Arul Jayaraman

December 2019

Major Subject: Chemical Engineering

ABSTRACT

Pressurized liquefied gases such as carbon dioxide are transported at a pressure above their saturation pressure. Therefore, if a pipeline transporting this substance ruptures, a large decrease in pressure occurs, causing the flashing of the fluid. Computational tools that predict how fast the depressurization occurs (decompression models) are of paramount importance to assess the consequences of potential pipeline rupture scenarios. Some of the main challenges when modeling this expansion process include: capturing the choked flow at the exit plane, which initiates the propagation of a decompression wave through the fluid; and addressing the phase transition that results in a multiphase flow.

The main objective of this research is to develop a 2-D full-bore rupture decompression model to simulate the transient depressurization of a pipeline transporting pure liquefied CO_2, using ANSYS Fluent as CFD software. The scope of this work focuses on incorporating non-equilibrium phase transition while addressing the calculation of properties for the metastable liquid region. Additionally, the scope includes the comparison of the CFD model predictions when implementing the Peng-Robinson (PR) EoS, and correlations based on the Span-Wagner (SW) EoS to calculate thermodynamic properties of the liquid phase.

When comparing the CFD model results with the experimental pressure-time curves and average decompression wave speed, the best prediction of the pressure plateaus for both PR and SW approaches are obtained using small values of the mass transfer

coefficient in the source terms ($C = 8\ s^{-1}$ for PR, and $C = 7\ s^{-1}$ for SW), which highlights the importance of incorporating non-equilibrium phase transition when modeling a rapid CO_2 decompression. On the other side, a more accurate prediction of the arrival of the decompression wave front at various locations along the pipeline is obtained when implementing correlations based on data from the SW EoS, in comparison to the CFD model incorporating the PR equation.

In general, the thermodynamic approach is deemed to have a predominant effect on the arrival of the decompression wave front at different locations along the computational domain, while the mass transfer coefficient (C) governs the phase transition and the pressure plateau representing this phenomenon.

DEDICATION

To my mentor Dr. M. Sam Mannan, who inspired me to start this journey as a PhD student at Texas A&M University.

To my parents Nancy and Eduardo, whose unconditional love and support helped me to accomplish this goal.

To my husband Martin for his love and encouragement, especially on those occasions when the tunnel exit was not very bright.

To my brother Sergio, for making me laugh with his vibrant personality.

ACKNOWLEDGEMENTS

I want to offer a word of thanks to my mentor Dr. M. Sam Mannan and his family. I will always treasure Dr. Mannan's advice and kindness at the bottom of my heart. He was an inspiration to all his students and we will carry on his legacy. He was our strongest supporter and taught us to work hard to achieve our dreams.

I would like to thank my advisor and committee chair, Dr. Charles J. Glover for his guidance and support during my time at Texas A&M. I really appreciate the time and the important insights you provided into my research. Thanks for your commitment and the valuable lessons you shared with me.

My advisory committee, Dr. James Holste, Dr. Ioannis Economou, and Dr. Hamn C. Chen, I appreciate the guidance you gave me during the doctoral program.

I would like to express my thanks to the Mary Kay O'Connor Process Safety Center, and especially to Mr. T. Michael O'Connor, you are a true visionary in the process safety field. My gratitude is extended to the research scientists who assisted me on different stages of my graduate career, including Dr. Ray Mentzer, Dr. Delphine Laboureur, Dr. Logan Hatanaka, Dr. Monir Ahammad, Dr. Chad Mashuga, and Mr. Henry Goyette.

Lastly, thanks to God, my parents, my husband, and my brother. All of you gave me the strength to succeed in my PhD journey and showed me your unconditional support.

CONTRIBUTORS AND FUNDING SOURCES

Contributors

Part 1, faculty committee recognition

This work was supervised by a dissertation committee consisting of (1) Professor Dr. Charles J. Glover (advisor) of the Artie McFerrin Department of Chemical Engineering, Texas A&M University; (2) Professor Dr. James Holste of the Artie McFerrin Department of Chemical Engineering, Texas A&M University; (3) Professor Dr. Ioannis Economou of the Department of Chemical Engineering, Texas A&M University at Qatar; and (4) Professor Dr. Hamn C. Chen of the Zachry Department of Civil and Environmental Engineering, Texas A&M University.

Part 2, student/collaborator contributions

All work for the dissertation was completed independently by the student.

Funding Sources

This work was supported by the Mary Kay O'Connor Process Safety Center (Texas A&M Engineering Experiment Station - TEES) at Texas A&M University. Its contents are solely the responsibility of the author and do not necessarily represent the official views of the Mary Kay O'Connor Process Safety Center.

NOMENCLATURE

1-D	One-dimensional
2-D	Two-dimensional
FBR	Full-bore rupture
C	Mass transfer coefficient in the source terms
CCS	Carbon capture and storage
CFD	Computational fluid dynamics
EoS	Equation of state
PR	Peng-Robinson
PT	Pressure transducer
P-T	Pressure-temperature
SoS	Speed of sound
SW	Span-Wagner
UDF	User-defined function
UDRGM	User-defined real gas model

TABLE OF CONTENTS

Page

LIST OF FIGURES

Page

LIST OF TABLES

Page

1. INTRODUCTION AND LITERATURE REVIEW

Pressurized liquefied gases are usually stored or transported at a pressure above their saturation pressure, and at a temperature close to atmospheric conditions. Thus, if there is loss of containment of a vessel or pipeline, a large release of pressure will occur, causing the flashing of the fluid [1]. Depending on the toxicity and flammability of the substance released, the rupture scenario could lead to different hazardous situations. For instance, if a pipeline transporting pressurized liquefied carbon dioxide (CO_2) ruptures, near-by residents and first responders may be exposed to toxic conditions since carbon dioxide is an asphyxiant denser than air, and may be fatal at concentrations greater than 10% [2, 3]. Therefore, tools that could predict how fast the depressurization occurs in a pipeline (decompression models), the release rate (discharge models) and the atmospheric concentration of the substance released (dispersion models) are of paramount importance to assess the consequences of potential rupture scenarios. The accuracy of decompression and discharge models for high-pressure pipelines has a significant impact on the posterior dispersion calculations, and it will further affect the risk assessment [4, 5].

The research area about pipeline rupture models for pressurized liquefied CO_2 has seen a steady growth during the last decades. Different Computational Fluid Dynamics (CFD) models that can predict the fluid behavior once the pipeline ruptures have been developed by several authors [2-4, 6-12]. Some of those are focused on modeling the decompression characteristics of CO_2 [6-8, 12], others include the study of the atmospheric expansion [2, 9, 10] and dispersion [3, 4, 11]. Some of the main challenges

when modeling these pipeline releases include: capturing the choked outflow generated by the large ratio between the high pressure pipeline and the atmospheric pressure [8]; and handling the flashing process (saturation conditions are reached) which leads to a multiphase flow [4, 7].

To better understand the physics after a pressurized pipeline ruptures and to validate models' prediction, a variety of release experiments have been conducted. Shock tube tests with liquefied CO_2 (pure or rich mixtures) [13-16], in addition to medium and large-scale CO_2 experiments (CO2PipeHaz [10, 17-20], CO2PIPETRANS [21, 22], COOLTRANS [2, 23]) and LPG tests (Isle of Grain tests [24]) have provided some insight about the behavior of pressurized fluids after the rupture of a pipeline. However, the relatively high Joule-Thomson coefficient for CO_2 makes its decompression behavior more difficult to predict in comparison to propane and natural gas [11].

Decompression models for pipelines transporting liquefied CO_2 correspond to a very active research area nowadays. The development of carbon capture and storage (CCS) technologies together with enhanced oil recovery activities encourage the development of CFD decompression models that can predict the consequences when the rupture of this type of pipeline occurs.

In the following sub-sections, a literature review shows the state-of-art in decompression models for pressurized liquefied gases with emphasis on CO_2, in addition to pipeline rupture experiments. A summary of Equations of State (EoS) implemented in CO_2 decompression and discharge models, and the fundamentals of computational fluid

dynamics are also included. The literature review allowed identifying the research gaps leading to the objectives and the methodology of this work.

1.1. Decompression behavior of pressurized liquefied gases

In case of rupture of a pressurized pipeline transporting a liquefied gas, the pressure decreases drastically around the discharge area; and when the liquid reaches the saturation conditions, it will transform into vapor. Therefore, two-phases are expected to flow out of the pipeline (an in-pipe multiphase flow is generated). Determined by the triggering cause, pipeline releases cover two general categories, the more likely puncture release, or the less likely but more disastrous full-bore rupture (FBR) [17].

Most of the decompression and discharge models for flashing fluids incorporate the homogenous equilibrium assumption into its formulation [4, 8, 25-29]. In this sense, the phases flowing out are assumed to be in mechanical and thermal equilibrium during the discharge [11], besides being distributed homogeneously across the pipeline [26]. Therefore, phenomena such as phase-slip (phases traveling at different velocities) and non-equilibrium vaporization are neglected [17]. Figure 1-1 summarizes the features of the homogeneous equilibrium assumption.

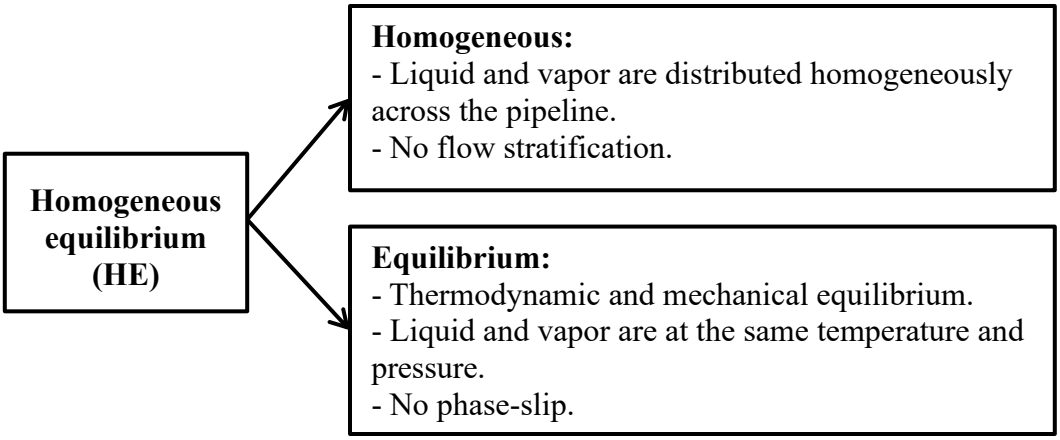

Figure 1-1. Homogeneous equilibrium assumption [11, 17, 26, 30].

Webber and Wardman (2010) [26] evaluated the performance of two software commonly used to model pipeline releases, PipeTech [25] and PipeBreak [26], both of them are based on the homogeneous equilibrium assumption. These authors compared model prediction with LPG releases [24], which included full-bore ruptures and puncture experiments. One of the main findings corresponded to an acceptable behavior of these homogeneous equilibrium models when predicting in-pipe pressure, temperature profiles, and inventory for full-bore ruptures. In contrast, both models showed predictive issues for the puncture experiment. One of the reasons that may justify the inaccuracy for the latter case is the possible non-homogeneous behavior of the in-pipe fluid during a puncture discharge, especially close to the orifice.

Other authors have highlighted the differences between full-bore ruptures and punctures. Brown *et al.* (2013) [17] analyzed some discrepancies of in-pipe flow regimes for these two cases. Flow stratification may occur during a puncture release, given the slower depressurization process in comparison to a guillotine rupture, which enables the

vapor phase to remain in the upper section of the pipeline, while the liquid flows in the lower portion. On the contrary, the more abrupt pressure drop occurring during a full-bore rupture causes the entrainment of the vapor phase with the high velocity liquid, generating a fully dispersed flow. As part of the CO2PipeHaz project, Brown *et al.* (2013) [17] published pictures of the inner flow patterns captured in a transparent pipeline section during release experiments with liquefied CO_2. These pictures allow differentiating the in-pipe flow behavior between a full-bore rupture and a puncture depressurization.

The decompression following full-bore ruptures and punctures has physical differences, which may lead to variations in the performance of modeling tools. The stratified two-phase flow may be the cause for the less accurate behavior when using homogeneous equilibrium models for punctures, in comparison to the acceptable prediction for full-bore ruptures. In the following sub-sections, models that predict the decompression behavior of liquefied gases (with emphasis on CO_2) are studied separately for each scenario.

1.1.1. Full-bore rupture models

1.1.1.1. One-dimensional models

PipeTech [25, 27, 31] is a 1-D homogeneous equilibrium model that combines partial conservation equations of mass, momentum and energy solved through the method of characteristics. Heat transfer between the fluid and the pipeline walls is included in the formulation, in addition to frictional effects (non-isentropic flow) [26, 31]. The Peng-Robinson equation of state is used to calculate the thermodynamic properties. Besides, the flow prior to the rupture is assumed to be in isothermal steady state [31]. This

homogeneous equilibrium model has been validated with the Isle of Grain LPG tests [24] and data obtained from the Piper Alpha disaster (methane gas line), showing a fair agreement for the full-bore rupture case [31].

Another model that incorporates the homogeneous equilibrium assumption is CFD-DECOM [8], which also includes a heat transfer model to calculate the heat across the pipe walls, and correlations to estimate the wall friction. A 1-D approach was selected and the conservation equations were discretized using the finite volume method. CFD-DECOM was validated using shock tube tests with gaseous and dense phase CO_2 from Cosham *et al*. (2012) [13]. The effect of CO_2 impurities, equations of state (Peng-Robinson, Peng-Robinson-Stryjek-Vera and Span-Wagner), heat transfer from the surroundings and wall friction were studied. Among the three EoS implemented to model the shock tube test with pure dense phase CO_2, the Span-Wagner EoS was found to generate the most accurate predictions of the decompression wave speed. In contrast, the Peng-Robinson EoS significantly underpredicted the speed of sound of the fluid, and therefore underpredicted a large portion of the decompression wave speed curve for this test. Lastly, the dense phase decompression was found to be more sensitive to the selection of the EoS than the gaseous depressurization.

X. Liu *et al.* (2015) [4] proposed a 1-D CFD depressurization model for the full-bore rupture of pipelines transporting high pressure CO_2 mixtures. The entire model includes three components: depressurization and source strength, atmospheric expansion, and dispersion. The results obtained at the pipeline exit serve as inlet boundary for the jet expansion model, and the atmospheric plane conditions are used for dispersion

calculations. ANSYS Fluent (CFD software) was used to simulate the depressurization and dispersion. On the other side, the jet expansion was modeled through a simplified set of conservation equations. For the purpose of calculating fluid properties in the 1-D depressurization model, a library of tables together with an interpolation scheme generated the thermodynamic properties of the mixture for any pressure and temperature; the GERG-2008 EoS was used to produce these tables. In addition, the CO_2 mixture in the pipeline was assumed to be a homogeneous equilibrium fluid which is at rest when time equals zero. Shock tube tests [13, 14] were used to validate the results obtained with the depressurization model incorporating the density-based solver in ANSYS Fluent. A significant difference between the predicted and experimental decompression wave speed was obtained, especially in the pressure plateau region representing the phase transition. X. Liu *et al.* (2015) [4] highlighted that this discrepancy may be related to the homogeneous equilibrium assumption, which neglects the non-equilibrium phase transition during the expansion, and therefore the model overpredicts the pressure associated to the evaporation process.

Several authors have developed 1-D FBR models that depart from the homogeneous equilibrium assumption. Brown *et al.* (2013) [17] developed a 1-D homogeneous relaxation model for CO_2 that accounts for non-equilibrium phase transition. However, the homogeneous assumption, *i.e.,* no stratification, and the mechanical equilibrium assumption, *i.e.,* no phase-slip, remained in the formulation. The homogeneous relaxation model includes the Peng-Robinson equation to calculate thermodynamic properties. It also incorporates frictional losses in the momentum and

energy conservation equations. Nevertheless, due to the rapid depressurization, it neglects the heat transferred between the surroundings and the pipe wall. To account for non-equilibrium phase transition, a fourth partial differential equation was included in addition to the traditional continuity, momentum and energy conservation equations for one-phase flow. This equation for the vapor mass fraction represents the delayed nucleation with respect to the equilibrium saturation conditions. For model validation, Brown *et al.* (2013) [17] used a shock tube test from the COOLTRANS project, in addition to a FBR experiment from CO2PipeHaz [18, 19]. A reasonable agreement between the prediction of the homogeneous relaxation model and the experiments was achieved.

Other authors have departed from the mechanical equilibrium assumption. Munkejord and Hammer (2015) [30] implemented a 1-D two-fluid model to capture the depressurization of pipelines transporting CO_2 mixtures. This model assumes that liquid and vapor may have different velocities during the decompression, which means that mechanical equilibrium is not attained (phase slip is modeled). On the contrary, thermodynamic equilibrium is considered in the formulation. The two-fluid model consists of one mass conservation equation for each component of the gas and liquid phases. Additionally, there is a momentum equation for each phase, and one energy equation for the liquid-gas mixture. The contribution of friction and gravitational force are included in the conservation equations. Additionally, Peng-Robinson is incorporated as equation of state. The two-fluid model performance was compared with the homogeneous equilibrium model using FBR experiments. Munkejord and Hammer (2015) concluded that a statement about which model achieves better predictions cannot be made based on

their results. However, if both models are compared based on their simplicity, the homogeneous equilibrium model may be preferred.

A number of authors have formulated and validated pipeline decompression models for full-bore ruptures using the homogeneous equilibrium assumption and other approaches, most of which correspond to one-dimensional models [4, 8, 17, 27, 30, 31]. For instance, Brown et *al.* (2013) [17] performed calculations with the homogeneous relaxation model using 500 identically sized cells along the horizontal axis of the pipeline, for the COOLTRANS shock tube test (144 m). In addition, for the CO2PipeHaz FBR experiment, the same authors divided the geometry into 100 identically sized cells along the axial direction (37 m). Munkejord and Hammer (2015) [30] implemented a two-fluid model for the FBR case using about 10 cells per meter; the effect of mesh refinement was included in the study. X. Liu *et al.* (2015) [4] adopted a 1-D mesh using different cell sizes; the elements had 0.01 m in width close to the exit plane, this measurement was progressively increased until elements reached 0.10 m in width at the closed-end of the pipeline.

1.1.1.2. Two-dimensional models

In recent years, the focus of FBR decompression models has started to move towards 2-D transient formulations that capture the behavior of variables (*e.g.*, pressure, temperature, and velocity) in both horizontal and vertical directions throughout the computational domain.

Elshahomi *et al.* (2015) [6] incorporated the GERG-2008 EoS into the formulation of a 2-D pipeline depressurization model for CO_2 mixtures using ANSYS Fluent as CFD

software. The density-based solver was used as solution strategy for the conservation equations. A homogeneous equilibrium flow was assumed, and the fluid velocity was considered to be negligible before the depressurization started. Besides, irreversible effects (non-isentropic) were considered, *e.g.,* friction effects. This model predicted the transient behavior of pressure and temperature along the pipeline, in addition to the average and local decompression wave speed; the latter is calculated as the subtraction of the outflow velocity from the speed of sound of the fluid at a specific location. Two shock tube tests [13, 14] were used for validation purposes; experimental pressure profiles at different locations along the shock tubes were compared with model predictions. The main contribution of these researchers was to implement the GERG-2008 EoS (typically used for natural gas) to calculate thermodynamic properties of CO_2 mixtures in a 2-D CFD formulation. A library of tables together with an interpolation scheme predicted the thermodynamic properties of CO_2 mixtures within specific ranges of pressure and temperature. Lastly, it is worth to mention that the model developed by Elshahomi *et al.* (2015) [6] showed a considerable overprediction of the pressure plateau representing the phase transition in the decompression wave speed curve, which may be related to neglecting the non-equilibrium evaporation process.

Rather than assuming homogeneous equilibrium when modeling the 2-D FBR case, other authors have departed to some extent from this assumption. B. Liu *et al.* (2017) [7] and B. Liu *et al.* (2018) [12] proposed a 2-D multiphase formulation based on the mixture-model, which is available in the pressure-based solver of the ANSYS Fluent software. This CFD model accounts for non-equilibrium phase transition (delayed

nucleation) and phase-slip. In addition, it implements the GERG-2008 EoS through property tables for pure CO_2 and mixtures. Besides, the phase transition is incorporated through mass and energy source terms. Although the model calculates the pressure-time profiles with certain degree of accuracy, it also shows numerical stability problems before reaching the pressure plateau, generating pronounced fluctuations in the pressure predictions. The authors [7] state that such fluctuations may be caused by assuming that after crossing the saturation line, the liquid properties are equivalent to the saturated liquid properties. This suggests that the CFD model does not address the prediction of thermodynamic properties of the superheated liquid state (metastable liquid resulting from the non-equilibrium phase transition). Despite the fluctuations, this CFD model improves the prediction of the decompression wave speed curve (especially at the pressure plateau region) in comparison to a generic homogeneous equilibrium model incorporating the GERG-2008 EoS.

1.1.2. Puncture models

Literature for the pipeline puncture case for pressurized liquefied gases is not as abundant as for the full-bore rupture scenario. Oke *et al.* (2003) [25] extended the homogeneous equilibrium model PipeTech to punctures. The model included the transient conservation equations for 1-D flow, in addition to a 2-D approach at the vicinity of the orifice. This puncture model was validated with the test P40 of the Isle of Grain LPG set [24]. For this experiment, the pipeline inner diameter (0.154 m) was almost the same as the puncture diameter (0.150 m). Therefore, Oke et *al.* (2003) used a quasi-full-bore rupture experiment to validate the puncture approach.

Woolley *et al.* (2015) [32] proposed a 1-D homogeneous relaxation model for punctures, focusing on the prediction of the heat transfer between the pipeline walls and the fluid. The importance of this approach is highlighted in the case of non-thermally insulated pipelines. A set of four conservation equations were solved for the liquid-vapor mixture, which is formed once the puncture occurs. Each of these equations incorporated a source term representing the mass, momentum, energy, or vapor flux leaving the pipeline through the puncture. The Peng-Robinson EoS was selected to predict the thermodynamic properties. A puncture experiment with pure CO_2 was used for validating model results, while two different constant values for the heat flux were tested. These authors concluded that the predictions of the model significantly depend on the heat transfer between the fluid and the walls.

Witlox *et al.* (2014) [33] presented the validation of discharge models available in the software Phast (version 6.7) with carbon dioxide puncture experiments performed in the CO2PIPETRANS project. These tests included steady state and transient releases with pressurized liquefied CO_2, and transient releases using pressurized supercritical CO_2. Phast is composed of analytical models that use the conservation equations together with an entropy balance to obtain the discharge rate and the dispersion profile [3]. Phast models include two scenarios, the leak scenario which assumes that the release occurs through an orifice in a vessel; and the full-bore rupture scenario, where the release occurs due to a guillotine rupture of a short pipe attached to a vessel. Besides, options of using a steady-state model (DISC) or a time-varying/transient model (TVDI) are available in the software. Since the experiments consisted of a vessel with a 5.5 m pipe section attached

(which ended in an orifice plate), researchers decided to neglect the pressure losses in this pipe section and used the leak scenario for modeling purposes. Different orifice sizes at the end of the pipe were used during the experiments. For both liquid and vapor releases, the model predicted the flow rate within 10% margin of error in comparison to the experimental results. This percentage was considered to be within the experimental accuracy.

Some of the orifice releases presented in Witlox *et al.* (2014) were used by X. Liu *et al.* (2014) [3] to develop a 2-D CFD model using ANSYS Fluent to predict the discharge rate and atmospheric dispersion from the rupture of high-pressure pipelines transporting CO_2. Phase transition was not included in the formulation and CO_2 was assumed to be a homogeneous fluid. The type of solver used in ANSYS Fluent (density-based or pressure-based) was not reported. Model validation was performed using two transient experiments with supercritical CO_2 of the BP dataset from the CO2PIPETRANS project [33]. The CFD geometry was composed of a pipe followed by a nozzle, which discharges to the atmosphere. It is worth noting that this geometry does not include an orifice plate or any other representation of a puncture, and therefore orifice experiments were modeled with a simplified geometry similar to a FBR case. Peng-Robinson EoS was incorporated into the formulation, showing a fairly accurate prediction of the averaged discharge rates when compared with experimental results. A considerable underprediction of the source terms was obtained with the ideal gas equation, as this EoS underpredicts the density of high-pressure CO_2. The commercial software Phast was used for comparison purposes,

calculating slightly higher discharge rates than the CFD model with Peng-Robinson, but showing smaller prediction errors than the latter.

A more recent paper from the same authors [5] proposed a 2-D formulation using the GERG-2008 EoS together with the multiphase mixture model, available in the pressure-based solver of ANSYS Fluent. Liquid and vapor phases were assumed to move at the same velocity (no phase-slip), and phase transition was incorporated through mass and energy source terms. Two orifice experiments from Witlox *et al.* (2014) were used for validation, which corresponded to steady state releases with liquefied CO_2. The geometry corresponded to a pipe followed by a nozzle, a similar arrangement to X. Liu *et al.* 2014 [3]; the main difference was the absence of the atmospheric zone at the end of the nozzle. No orifice plate or any other representation of a puncture was included in the geometry; instead, the nozzle acquired the same diameter as the orifice in the experiments. One of the main conclusions from this study was related to the appropriate selection of the mass transfer coefficient in the source terms of the phase transition model, since a higher value of this factor leads to a lower prediction of the release rate.

1.2. Fundamentals of Computational Fluid Dynamics (CFD)

Computational fluid dynamics (CFD) is the analysis of systems associated with fluid flow, heat transfer and other transport phenomena through computer-based tools. CFD codes are composed of a pre-processor, a solver and a post-processor.

The pre-processor is related to the definition of the computational domain, which includes the generation of the geometry and the mesh (also called grid); it usually covers the designation of boundary conditions as well. The grid corresponds to the division of the

geometry into smaller sub-domains (cells); the solution of the conservation equations is defined at nodes located in each cell (control volume or element) [34].

The solver takes the partial differential equations (which represent continuous functions) and discretizes them through different approaches, one of them being the finite-volume method. This discretization generates a set of algebraic equations applied to the nodes. The algebraic equations are solved through matrix solvers and the discrete solution of the transport problem is obtained. The finite volume method is used in the CFD software ANSYS Fluent [6, 35]. This method was developed based on the finite difference framework, where truncated Taylor series expansions produce finite difference approximations of derivatives, which combine the value of flow properties at each node and its neighbors. The algebraic equations for the nodes of a grid are obtained with the finite volume method through the next steps: 1. integration of the conservation equations over the control volumes of the domain, 2. discretization of the differential equations replacing the derivatives by finite difference approximations, 3. implementation of an iterative method to solve the algebraic form of the equations [34]. It should be noted that for a transient case, the conservation equations are also integrated over time in step one. Before applying the finite volume method, the Navier-Stokes equations (conservation of momentum) should be time-averaged in the case of turbulent flow. The previous statement is justified due to the fact that in the turbulent regime, the flow behavior is highly random and chaotic, and it becomes intrinsically unsteady even with constant boundary conditions [34]. Therefore, when modeling turbulent flow, the Reynolds-Averaged Navier-Stokes

(RANS) equations are used to represent the conservation of momentum in the CFD code, together with a turbulence model.

The last component of a well-established CFD software is the post-processor, which organizes and displays the data generated by the solver. Current post-processors consist of data visualization tools that produce contour plots of process variables, animations of transient simulations, vector plots, and others.

1.2.1. Pressure-based and density-based solvers in ANSYS Fluent

One of the most important decisions when modeling systems transporting compressible fluids, *e.g.,* pressurized pipelines, is related to the type of solver to use. This selection will have an impact on the solution process of the conservation equations together with the EoS. Two solvers are available in ANSYS Fluent, density-based and pressure-based, which can be used for different types of flows.

The pressure-based approach was originally designed for incompressible and mildly compressible flows at low speed, whereas the density-based solver was developed for compressible flows at high speed. Nevertheless, both approaches have been reformulated to some extent, so they can be applicable to a larger spectrum of flow conditions beyond their original scope [36].

The density-based formulation solves the continuity, momentum, energy and species equations together as a coupled set; turbulence equations are solved afterwards. The continuity equation calculates the density profile, the momentum equations determine the velocity field, and the equation-of-state is used to calculate the pressure profile [6].

Different authors [4, 6] have developed pipeline decompression models for carbon dioxide using the density-based solver in ANSYS Fluent.

Compared to the density-based approach, the pressure-based solver works differently. A pressure equation is obtained by employing the continuity and momentum equations, making sure that the velocity field (corrected by the pressure) satisfies the continuity [7]. The momentum equations calculate the velocity field and the created pressure formulation determines the pressure profile. Several multiphase models are formulated with the pressure-based solver, but are not available with the density-based formulation. Examples include the Volume of Fluid (VOF) model which is an interphase-tracking technique applied to immiscible fluids, *e.g.*, stratified flows; the mixture model, where the phases are assumed to be interpenetrating continua, *i.e.*, the phases are dispersed in the domain and there are no sharp interphases; and the Eulerian approach, which is a more elaborated version of the mixture model that solves continuity, momentum and energy equations for each phase [36]. Different authors [5, 7, 12] have developed pipeline decompression models for carbon dioxide using the pressure-based solver, implementing the multiphase mixture model in ANSYS Fluent.

1.3. Equations of state for decompression models

To model the CO_2 behavior once a pipeline ruptures, accurate means of determining the thermodynamic properties of the fluid are essential. To-date, no equation of state is considered as the reference equation for CO_2 mixtures [6]. However, thermodynamic properties of pure CO_2 are well predicted by the empirical Span-Wagner EoS [37]. Unlike Peng-Robinson and Soave-Redlich-Kwong (both of them cubic

equations), the Span-Wagner EoS is valid for temperature and pressure close to the critical region [38]; nevertheless, this EoS demands more computational resources than simpler formulations such as Peng-Robinson [39]. In the existing 1-D decompression models for CO_2, the cubic Peng-Robinson EoS is usually incorporated due to its rather simple mathematical form [8, 17, 30, 32].

Several researchers have studied the effect of different equations of state on discharge models for carbon dioxide. For instance, X. Liu *et al.* (2014) [3] compared the total discharged mass obtained in the experiments with the predictions using the ideal gas and the Peng-Robinson EoS. A significant underprediction of the total discharged mass was obtained with the ideal gas EoS, as this equation underpredicts the density of high-pressure CO_2. While the Peng-Robinson EoS showed an underprediction of around 3% from the measured mass value, the ideal gas equation showed a higher deviation (around 20-25%).

Witlox *et al.* (2014) compared the performance of Peng-Robinson, Soave-Redlich-Kwong and Span-Wagner EoS when determining the initial density (before the expansion starts) in trials using pure liquefied and super-critical CO_2. The Span-Wagner EoS provided the best density predictions when compared with the experimental values, followed by Peng-Robinson and lastly, Soave-Redlich-Kwong [38].

Jie *et al.* (2012) [8] compared the performance of three different EoS when modeling CO_2 releases, Peng-Robinson (PR), Peng-Robinson-Stryjek-Vera (PRSV) and Span-Wagner (SW). Among the three equations, the Span-Wagner EoS was found to produce the most accurate prediction of the decompression wave speed while modeling

the shock tube test with pure liquefied CO_2. In contrast, the PR and the PRSV EoS significantly underpredicted a large portion of the decompression wave speed curve for this test.

The GERG-2008 EoS, which is the current reference equation for natural gas [6], has also been incorporated in decompression models for pure CO_2 [5, 7] and CO_2 mixtures [4, 6, 12]. For some of these models, a reasonable agreement was obtained when comparing the model predictions with experimental transient pressure profiles along the pipeline [6, 7]. It is worth noting that the GERG-2008 EoS was incorporated in the previous decompression models through the use of tables with thermodynamic properties, *e.g.*, density, enthalpy, entropy, speed of sound, specific heat, and several derivatives. The decision to use tables together with an interpolation scheme, instead of a library of functions, was made due to different factors, including the high computational cost of a direct call to the library and the failure to produce properties at certain P-T values, which caused the library to crash [6]. A summary of equations of state used in different FBR pipeline decompression models for pressurized systems (mainly liquefied CO_2) is reported in Table 1-1.

Table 1-1. Equations of state in pipeline FBR decompression models.

Decompression model	**Substance**	**Equation of state**	**References**
PipeTech (1-D HE)	LPG	Peng-Robinson	[27, 31]
1-D Homogeneous relaxation model (HRM)	Pure CO_2	Peng-Robinson	[17]
1-D two-fluid model	CO_2 mixtures	Peng-Robinson	[30]

Table 1-1. Continued.

Decompression model	Substance	Equation of state	References
CFD-DECOM (1-D HE)	- Pure CO_2 - CO_2 mixtures	- Peng-Robinson - Peng-Robinson-Stryjek-Vera - Span-Wagner	[8]
Density-based solver in ANSYS Fluent (1-D HE)	CO_2 mixtures	GERG-2008	[4]
Density-based solver in ANSYS Fluent (2-D HE)	CO_2 mixtures	GERG-2008	[6]
Pressure-based mixture model in ANSYS Fluent (2-D)	- Pure CO2 - CO_2 Mixtures	GERG-2008	[7, 12]

In the following sub-sections, a summary of equations of state incorporated in this work is presented.

1.3.1. The virial equation of state

The virial equation of state can be described as an extension of the ideal gas law [40]. It uses a series expansion to define the compressibility factor (Z) in a polynomial form as a function of pressure or density [41]. The expansion with respect to density (ρ) can be written as follows:

$$Z = 1 + B\rho + C\rho^2 + D\rho^3 + E\rho^4 + \cdots \quad \textbf{(1-1)}$$

Where B, C, D and E are the virial coefficients, which depend on temperature. This equation is commonly truncated until the third virial coefficient (C) as follows:

$$Z = \frac{P}{\rho RT} = 1 + B\rho + C\rho^2 \quad \textbf{(1-2)}$$

The virial equation truncated until the third virial coefficient is typically applied for gases at low to moderate pressures [41]. Equation (1-2) results in a cubic equation with respect to the density:

$$\rho^3 + \frac{B}{C}\rho^2 + \frac{1}{C}\rho - \frac{P}{CRT} = 0 \quad \textbf{(1-3)}$$

The expression for each of the virial coefficients (*B* and *C*) as function of temperature can be obtained using data from other equation of state, as explained in Section 3.4.1.

1.3.2. The Peng-Robinson equation of state

Cubic equations of state are commonly used in industrial applications due to its simplicity. These equations are explicit in pressure and can be expressed as a third order polynomial in specific volume or density. One of the most used equations of state in hydrocarbon's applications is the Peng-Robinson EoS [42], which can be expressed as:

$$P = \frac{RT}{v - b} - \frac{a(T)}{v(v + b) + b(v - b)} \quad \textbf{(1-4)}$$

$$a(T) = 0.45724\frac{R^2T_c^2}{P_c}\left\{1 + n\left[1 - \left(\frac{T}{T_c}\right)^{0.5}\right]\right\}^2 \quad \textbf{(1-5)}$$

$$b = 0.07780\frac{RT_c}{P_c} \quad \textbf{(1-6)}$$

$$n = 0.37464 + 1.54226\omega - 0.26992\omega^2 \quad \textbf{(1-7)}$$

Where v is specific volume, T is temperature and P is pressure. R is the universal gas constant, while T_c and P_c are the critical temperature and critical pressure, respectively. Lastly, ω is the acentric factor which is specific for each substance. It is worth to mention that the first term of Equation (1-4) ($RT/(v-b)$) represents the repulsion pressure, while the second term represents the attraction pressure, and therefore $a(T)$ can be considered as a measure of the intermolecular attraction force [42].

The Peng-Robinson EoS allows predicting physical properties in the vapor and liquid regions. Since this equation is expressed as a cubic function in specific volume or density, three solutions or roots can be calculated for a specific pair of temperature and pressure. Depending on the number of phases in the system, the Peng-Robinson EoS results in one real root (in addition to two complex roots) or three real roots. Figure 1-2 illustrates a general pressure versus density diagram for a cubic equation, depicting one isotherm.

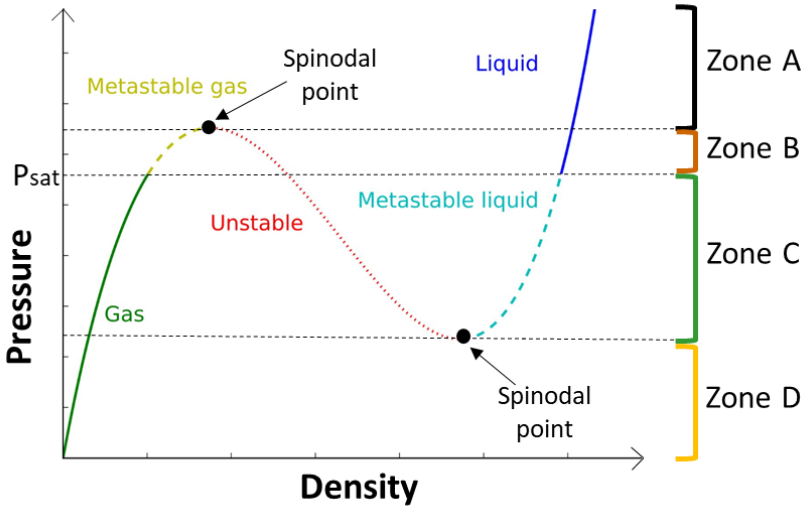

Figure 1-2. Pressure versus density diagram for a cubic EoS. Adapted from [43].

In zone A, there is one real root which represents the liquid density. One of the limits of zone A is the spinodal point to the left side of Figure 1-2. The spinodal point corresponds to the stability limit of a single-phase fluid [43], at this point $(\partial P/\partial \rho)_T = 0$.

After entering zone B (between the spinodal point and the saturation line), there are three real roots for the density of the fluid. In this case, the smallest density root represents the metastable gas density; the name 'metastable' is used because these states usually exist temporarily until phase transition occurs [36]. The largest root in this zone corresponds to the liquid density. Lastly, the root in the middle (red portion of the curve) does not have physical significance since it violates the stability criterion, showing $(\partial P/\partial \rho)_T < 0$. When the pressure corresponds to the saturation pressure, the smallest and largest roots correspond to saturated vapor and saturated liquid properties, respectively.

In zone C (below the saturation line until the spinodal point located to the right side of Figure 1-2), there are also three real roots. The smallest density root represents the gas density, while the largest corresponds to the metastable liquid density. Similar to zone B, the root in the middle (red portion of the curve) does not have physical significance since it violates the stability criterion, showing $(\partial P/\partial \rho)_T < 0$. Lastly, only one real root exists in zone D, corresponding to gas density.

In the CFD software ANSYS Fluent, the selection of the density root when implementing a cubic EoS depends on the phase specified as 'real gas phase' by the end user. For instance, if the liquid is selected as the 'real gas phase' when incorporating the Peng-Robinson EoS, ANSYS Fluent will take the largest density root in zones B and C.

Therefore, the density calculation for metastable liquid states (also called superheated liquid) is included in the CFD formulation. As explained in following sections, this feature is of great importance for the CFD model developed in this work.

In addition to density, properties as heat capacity, speed of sound, enthalpy and entropy can be derived from Peng-Robinson. This cubic EoS is implemented in ANSYS Fluent, where such properties are calculated as a combination of the ideal gas property and a residual function (to compensate for the real fluid behavior). ANSYS Fluent calculates these physical properties as a function of pressure and temperature as follows:

$$F(T,P) = F^{ideal}(T,P) + F^{r}(T,P) \quad \textbf{(1-8)}$$

Where F^{ideal} represents the ideal gas property and F^{r} is the residual property.

Before defining the residual functions for different physical properties using the Peng-Robinson EoS, is important to define the ideal gas properties. For instance, the ideal gas heat capacities at constant pressure are known for several substances, and therefore it can be expressed as a function of temperature as follows:

$$C_P{}^{ideal} = a_0 + a_1 T + a_2 T^2 + \cdots \quad \textbf{(1-9)}$$

Where a_0, a_1 and a_2 represent the coefficients obtained from a regression using experimental ideal gas heat capacities at different temperatures, and can be found in the literature. In addition, the ideal gas heat capacity at constant volume is related to the ideal gas heat capacity at constant pressure:

$$C_v{}^{ideal} = C_p{}^{ideal} - R \quad \textbf{(1-10)}$$

In the case of the ideal gas enthalpy, it is defined as:

$$H^{ideal} = H_{ref}(T_{ref}) + \int_{T_{ref}}^{T} C_p{}^{ideal} dT \quad \textbf{(1-11)}$$

In addition, the ideal gas entropy is expressed as follows:

$$S^{ideal} = S_{ref}(T_{ref}, P_{ref}) + \int_{T_{ref}}^{T} \frac{C_v{}^{ideal}}{T} dT + R \int_{v_{ref}}^{v} \frac{1}{v} dv \quad \textbf{(1-12)}$$

The enthalpy of a real gas can be defined as:

$$H = H^{ideal} + H^r \quad \textbf{(1-13)}$$

Where the residual function for enthalpy (H^r) can be derived from the Peng-Robinson EoS as follows [36]:

$$H^r(T, P) = Pv - RT + \left(\frac{T\frac{\partial a}{\partial T} - a}{2\sqrt{2}\, b} \right) Ln\left(\frac{v + b(1+\sqrt{2})}{v + b(1-\sqrt{2})} \right) \quad \textbf{(1-14)}$$

Where a and b are defined in Equation (1-5) and Equation (1-6), respectively.

The specific heat capacity at constant volume (isochoric) is expressed as:

$$C_v = C_v^{ideal} + C_v^r \quad \textbf{(1-15)}$$

At the same time, the residual heat capacity at constant volume (obtained from the PR EoS) is defined as follows:

$$C_v^r = \left(\frac{\frac{\partial a}{\partial T} + T\frac{\partial^2 a}{\partial T^2}}{2\sqrt{2}\, b} \right) Ln\left(\frac{v + b(1+\sqrt{2})}{v + b(1-\sqrt{2})} \right) \quad \textbf{(1-16)}$$

Where a and b are defined in Equation (1-5) and Equation (1-6), respectively.

The specific heat capacity at constant pressure is expressed as:

$$C_p = \left(\frac{\partial h}{\partial T}\right)_p = C_p^{ideal} + C_p^r \quad \textbf{(1-17)}$$

$$C_p^r = -C_v^r + R + T\frac{(\partial v/\partial T)^2}{\partial v/\partial P} \quad \textbf{(1-18)}$$

The entropy of a real gas can be defined as:

$$S = S^{ideal} + S^r \quad \textbf{(1-19)}$$

Where the residual function for entropy (S^r) can be derived from the Peng-Robinson EoS as follows [36]:

$$S^r = Rln\left(\frac{v-b}{v_{ref}}\right) + \frac{\left(\frac{\partial a}{\partial T}\right)}{2\sqrt{2}\,b} Ln\left(\frac{v+b\left(1+\sqrt{2}\right)}{v+b\left(1-\sqrt{2}\right)}\right) \quad \textbf{(1-20)}$$

Where a and b are defined in Equation (1-5) and Equation (1-6), respectively.

Another important thermodynamic definition is the speed of sound (w), which is the square root of the change of pressure with respect to density, at constant entropy:

$$w = \sqrt{\left(\frac{dP}{d\rho}\right)_s} \quad \textbf{(1-21)}$$

The speed of sound can be derived from an equation of state using heat capacities, and derivatives of pressure as follows [44]:

$$w = \sqrt{-\left(\frac{v^2 C_p}{C_v}\right)\left(\frac{\partial P}{\partial v}\right)_T} \qquad \textbf{(1-22)}$$

1.3.3. Equations of state based on Helmholtz free energy

Typically, equations of state are defined as functions of pressure, density and temperature. However, equations of state can also be based upon fundamental thermodynamic properties as internal energy, enthalpy, Helmholtz or Gibbs energy. In the last decades, equations based on Helmholtz free energy have been of great importance [37, 45], showing that accurate predictions can be achieved using fundamental equations. Examples of this approach are the Span-Wagner EoS [37], which represents thermodynamic properties of carbon dioxide and is known as the reference EoS for this substance; in addition to the GERG-2008 EoS for natural gas properties [45].

The Helmholtz free energy is convenient since by definition is a function of density and temperature, which are measurable properties. The Helmholtz free energy (A) can be defined as the ideal gas Helmholtz free energy (A^{ideal}) plus the residual property (A^r) at any given density and temperature, as follows [37]:

$$A(T,\rho) = A^{ideal}(T,\rho) + A^r(T,\rho) \qquad \textbf{(1-23)}$$

Where,

$$A^{ideal}(T,\rho) = \int_{T_{ref}}^{T} C_p^{ideal} dT + H_{ref} - RT - T\int_{T_{ref}}^{T} \frac{C_p^{ideal} - R}{T}\, dT - RT\left[\ln\left(\frac{\rho}{\rho_{ref}}\right)\right] - TS_{ref} \qquad \textbf{(1-24)}$$

Span and Wagner (1996) [37] and the GERG-2008 EoS [45] define the residual Helmholtz energy as an empirical equation with numerous coefficients. In addition, the thermodynamic properties are reported as dimensionless variables, which usually benefits the non-linear regression of multiple coefficients. The dimensionless Helmholtz energy for both approaches is defined as:

$$\frac{A}{RT} = \alpha(\delta, \tau) = \alpha^o(\delta, \tau) + \alpha^r(\delta, \tau) \quad \textbf{(1-25)}$$

$$\delta = \frac{\rho}{\rho_C} \qquad \tau = \frac{T_c}{T} \quad \textbf{(1-26)}$$

Where $\alpha(\delta, \tau)$ is the dimensionless Helmholtz energy, $\alpha^o(\delta, \tau)$ is the dimensionless ideal Helmholtz energy, and $\alpha^r(\delta, \tau)$ is the dimensionless residual Helmholtz energy. Besides, δ is the reduced density and τ is the inverse reduced temperature.

The residual Helmholtz energy is empirically determined since no theoretical approach is considered to be sufficiently accurate. However, given that the Helmholtz energy cannot be directly measured, an empirical expression for the residual part was developed by Span and Wagner (1996) [37], employing experimental data for different properties. Span and Wagner (1996) define the dimensionless residual Helmholtz energy as follows:

$$\alpha^r(\delta,\tau) = \sum_{i=1}^{7} n_i \delta^{d_i} \tau^{t_i} + \sum_{i=8}^{34} n_i \delta^{d_i} \tau^{t_i} \exp(-\delta^{c_i}) + \sum_{i=35}^{39} n_i \delta^{d_i} \tau^{t_i} \exp(-\alpha_i(\delta-\epsilon_i)^2 - \beta_i(\tau-\gamma_i)^2) + \sum_{i=40}^{42} n_i \Delta^{b_i} \delta \exp(-C_i(\delta-1)^2 - D_i(\tau-1)^2) \quad \textbf{(1-27)}$$

Equation (1-27) results in 42 terms, which combine different coefficients and exponents, including $n_i, d_{i,} t_i, c_i, \alpha_i, \beta_i, \gamma_i, \epsilon_i$ and others. It is worth to mention that the GERG-2008 EoS uses a similar function for the dimensionless residual Helmholtz energy. However, the number of terms, the coefficients' values and the general shape of the equation are different for both EoS.

By using thermodynamic relations, properties such as pressure, entropy, enthalpy, speed of sound and others can be derived from the Helmholtz free energy equation (Equation (1-25)).

In general, the empirical function of the residual Helmholtz energy (Equation (1-27)) offers enough flexibility to estimate physical properties in a wide range of pressure and temperature with high accuracy. However, the complexity of the equation potentially increases the computational time while calculating thermodynamic properties in robust computation fluid dynamics (CFD) models. Therefore, this work presents a new methodology to use highly accurate information extracted from the Span-Wagner EoS to develop simplified correlations applicable to a limited range of temperature and pressure. These correlations are incorporated in a CFD decompression model for pure CO_2.

1.4. Pipeline rupture experiments for pressurized liquefied gases

To better understand the depressurization process that a pipeline transporting a pressurized liquefied gas undergoes once it ruptures, different experiments have been conducted in the last decades. Richardson and Saville (1996) [24] performed full-bore rupture and puncture experiments with LPG (95% propane). The tests were conducted using two 100 m long pipelines, one was 150 mm in diameter and the other 50 mm in diameter. Steady-state and transient conditions were implemented; both types of experiments were initiated with the rupture of a disk at one end of the pipeline. This experimental set has been used to validate depressurization models proposed by different authors [25, 31].

In the context of experiments using high pressure CO_2, Pham and Rusli (2016) [46] conducted a review to summarize the experimental data sets, besides CO_2 modeling methods available in the literature. Some of the experiments corresponded to shock tube tests (pure CO_2 or rich mixtures) [13, 14], in addition to medium and large-scale experiments such as CO2PipeHaz [10, 17-20], CO2PIPETRANS [21, 22], and COOLTRANS [2, 23].

In the CO2PipeHaz project [19], experiments with different geometric arrangements were conducted, including a 9 m pipe attached to a 2 m^3 spherical vessel [10]; tests performed by Dalian University of Technology with a 256 m long pipeline [20]; experiments with a 36.70 m long, 0.04 m diameter pipeline which had a transparent section to study the in-pipe fluid flow during the expansion [17, 18]; and others.

The CO2PIPETRANS experiments [22] included full-bore rupture and puncture scenarios with a 200 m long, 0.05 m diameter pipeline. The initial pressure and temperature were set around 100 bar and between 3-15 ºC. Therefore, the initial pressure was greater than the critical pressure of CO_2 ($P_{critical}$ = 73.8 bar), but the initial temperature was below the critical temperature ($T_{critical}$ = 31 ºC).

Experiments with fast response pressure transducers that allow detecting the fluid behavior on early stages of the decompression (milliseconds time frame) were conducted by Botros *et al.* (2015) [15] and Botros *et al.* (2016) [16] for pure CO_2 and binary mixtures of CO_2-impurities, respectively.

In this work, the validation of the CFD model is performed using Test 32A from Botros *et al.* (2015) [15]. This pure CO_2 test was conducted using a shock tube with total length of 42 m and 38.1 mm of internal diameter (I.D.). The initial conditions before the full-bore rupture corresponded to pressurized liquefied CO_2 at 11.27 MPa-a and 281.89 K. Therefore, the initial conditions were above the critical pressure but below the critical temperature. A decompression wave propagated towards the closed-end of the shock tube after the burst of a rupture disk, initiating the expansion process. The monitor points in the CFD model correspond to the location of the pressure transducers (PT) in the experiment. A total of 13 fast response pressure transducers (with an uncertainty of ± 0.04 MPa each) were mounted along the spool adjacent to the rupture disk. Lastly, it is worth to mention that the shock tube was thermally insulated. Some of the features and initial fluid conditions of Test 32A are summarized in Table 1-2.

Table 1-2. Test 32A from Botros *et al.* (2015) [15].

Total length	42 m			
Internal diameter	38.1 mm			
Initial conditions	$P_{initial}$ = 11.27 MPa-a, $T_{initial}$ = 281.89 K			
Location of pressure transducers (Distance from open-end)	PT1: 0.0295 m PT1A: 0.0924 m PT1B: 0.1028 m PT2: 0.2 m	PT3: 0.35 m PT4: 0.5 m PT5: 0.7 m	PT6: 0.9 m PT7: 1.1 m PT8: 3.1 m	PT9: 5.1 m PT10: 7.1 m PT11: 9.1 m

A schematic of the experimental arrangement is illustrated in Figure 1-3.

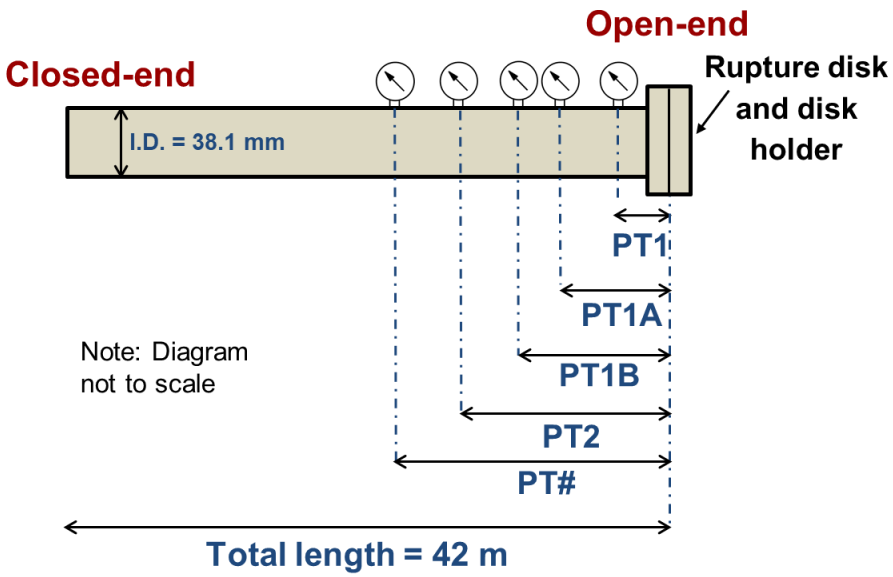

Figure 1-3. Schematic of experimental arrangement of Botros *et al.* (2015) [15].

2. RESEARCH FRAMEWORK

2.1. Problem statement and significance

The transportation of CO_2 through pipelines began in the early 1970s in the U.S. [47]. Per the 2015 U.S. Department of Energy (DOE) report [48], the CO_2 network in the U.S. consists of 50 individual pipelines with a joint length of about 4500 miles; the majority of which are related to enhanced oil recovery activities, while a small portion is employed in other sectors such as beverage manufacturing.

In the worldwide context, there is a growing interest in the transportation of compressed CO_2 by pipelines dedicated to Carbon Capture and Storage (CCS) technologies [49]. In general, there are three stages in the CCS process. Firstly, the CO_2 is captured from an industrial facility or any other anthropogenic source; secondly, it is transported by pipelines to a storage site which is typically a geological formation; and lastly it is injected and stored into this geological reservoir [50, 51]. In regard to enhanced oil recovery, the CO_2 serves an additional purpose in the CCS chain, since its injection leads to the reduction of oil viscosity and consequently an improvement in oil production [52].

The CO_2 pipelines are one of the components of CCS. Therefore, the development and growth in the implementation of these processes result in an increase of CO_2 transportation. Pressurized pipelines are commonly considered the most economical and efficient method to transport large volumes of this substance, especially when the geological formation is distant from the capture site [53, 54]. Since CO_2 is an asphyxiant

denser than air and may be fatal at concentrations greater than 10% [2, 3], there is a need to perform consequence modeling for rupture scenarios of CO_2 high-pressure pipelines.

The study of pipeline rupture releases plays a preponderant role in the process safety area. According to data collected by the U.S. Pipeline and Hazardous Materials Safety Administration (PHMSA), 92 incidents involving pipelines transporting liquefied CO_2 occurred in the U.S. from 1999 to 2018 [55]; this set of incidents resulted in one injury and no fatalities, in addition to the release of about 70500 barrels of CO_2. From this perspective, the development of accurate tools to predict the consequences of CO_2 pipeline ruptures is an important field of study.

The rupture scenario of a high-pressure pipeline is typically divided into three sections: depressurization, which predicts the flow conditions inside the pipeline during the release; then, the atmospheric expansion of the jet; and lastly, the dispersion of the toxic or flammable substance through the atmosphere. This research is focused on the depressurization stage, which serves as input for atmospheric expansion and dispersion models. Figure 2-1 illustrates the three stages of the pipeline rupture scenario.

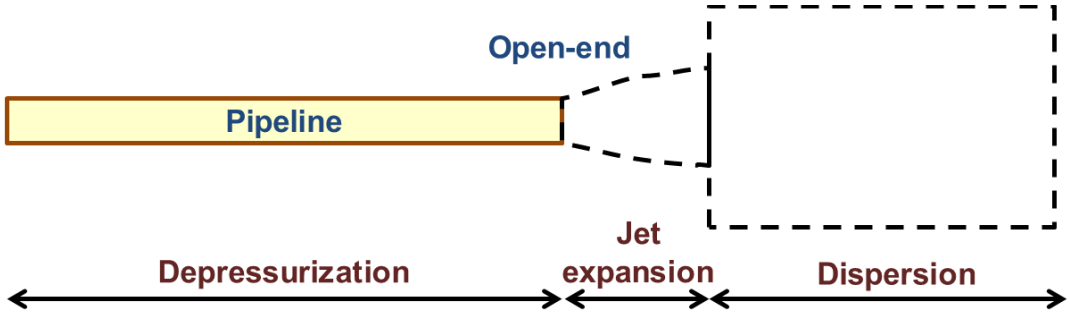

Figure 2-1. Problem schematic: rupture of a high-pressure pipeline.

The CO_2 decompression process results in a significant decrease in temperature due to the Joule-Thomson effect. Therefore, there would be solid CO_2 formation (especially close to the outlet) if the temperature reaches the triple point (216.58 K and 5.185 bar [56]) during the expansion [20, 57].

The depressurization after the failure of a pipeline transporting liquefied CO_2 is commonly assumed to be an adiabatic process due to the short durations considered in full-bore rupture models [17]. Additionally, the isentropic simplifying assumption is generally implemented when modeling this phenomenon [13].

An almost instantaneous choked flow at the exit plane occurs after the pipeline ruptures [57], initiating the propagation of a decompression wave through the fluid. This expansion wave moves towards the intact end of the pipeline. The arrival of the wave at a specific location results in the acceleration of the fluid in the opposite direction of the wave trajectory [11]. This process explains the loss of containment from the system. It is worth to mention that the velocity of the decompression wave is equal to the local speed of sound of the fluid minus the local outflow velocity [13]. Therefore, the equation of state used to predict the speed of sound in a decompression model has an important effect on the prediction of the expansion wave speed. An accurate calculation of the wave speed is necessary to predict how quick the pipeline empties, in addition to assess if a propagating fracture may occur within the pipeline material.

The expansion process usually leads to a phase transition resulting in a two-phase flow in the pipeline. In the case of a full-bore rupture, Brown *et al.* (2013) [17] reported that video recording of the flow patterns inside the pipeline showed the entrainment of the

produced vapor with the liquid phase. Therefore, a full-bore depressurization is commonly associated with fully dispersed flow (no stratification of the liquid and vapor phases). In addition to multiphase patterns, decompression experiments with pure liquefied CO_2 have shown that phase transition can occur at a pressure below the equilibrium saturation conditions [13, 15]. This may happen due to the high speed of the expansion process, so the liquid may temporarily become superheated, and a mass transfer between the metastable liquid and the vapor phase would be expected.

In general, modeling the depressurization of a pipeline transporting liquefied CO_2 is a complex problem due to the various phenomena involved. The propagation of the decompression wave drives the expansion process, while the non-equilibrium phase transition leads to a multiphase flow. Traditional decompression models assume one-dimensional flow and homogeneous equilibrium, where the two-phase mixture generated during the expansion is treated as a pseudo-fluid governed by the conservation equations of one-phase flow [8]. Therefore, homogeneous equilibrium models assume that the phase transition is an instantaneous process that occurs at saturation conditions, and hence the vapor and liquid phases do not co-exist [12].

Recently, two-dimensional CO_2 decompression models that depart from the equilibrium assumption have been developed in the Computational Fluid Dynamics (CFD) context [7, 12, 58]. However, to date, a systematic study on the impact of different equations of state on the decompression model predictions is lacking in the literature. In addition, some of these models do not address the prediction of thermodynamic properties for the superheated liquid state, and show numerical stability problems when predicting

the pressure-temperature trajectories and the pressure-time traces along the pipeline [7, 12].

This research aims to develop a CO_2 decompression model incorporating non-equilibrium phase transition and addressing the calculation of properties for the metastable liquid region. Additionally, the scope includes the comparison of the CFD model predictions when implementing the Peng-Robinson (PR) EoS and correlations based on the Span-Wagner (SW) EoS to calculate thermodynamic properties of the liquid phase.

2.2. Objectives

The main objective of this research is to develop a 2-D full-bore rupture decompression model to simulate the transient depressurization of a pipeline transporting pure liquefied CO_2, using ANSYS Fluent as CFD software. The scope of this work focuses on two specific objectives:

1. Study the effect of the non-equilibrium phase transition assumption on the predictions of the CFD decompression model.
    1.1 Incorporate non-equilibrium phase transition through mass and energy source terms in the conservation equations of the multiphase mixture approach.
    1.2 Analyze the effect of varying the mass transfer coefficient (C) of the source terms.
    1.3 Conduct the validation of the CFD model using the shock tube test 32A from Botros *et al.* (2015) [15].
2. Study the effect of the thermodynamic approach on the predictions of the CFD decompression model.

2.1 Develop correlations for the thermodynamic properties of the liquid (including the superheated liquid region) and vapor phases based on data from the Span and Wagner EoS.

2.2 Program the correlations through User-Defined Functions (UDFs) and a User-Defined Real Gas Model (UDRGM) written in the C programming language.

2.3 Compare the model predictions with the Peng-Robinson EoS to the results obtained with correlations based on the Span-Wagner EoS, both used to calculate the properties of the liquid phase.

2.3. Methodology

Figure 2-2 illustrates the methodology to achieve the objectives of this research. The development of the CFD decompression model is explained in Section 3, where the assumptions, geometry, mesh, the multiphase mixture approach and the calculation of the thermodynamic properties are described in detail. Section 4 is dedicated to the discussion of the results with the CFD model using the PR EoS for the liquid phase properties, together with a combination of the Virial EoS and correlations based on the SW EoS to calculate the properties of the vapor phase. Section 5 describes the results of the CFD model implementing SW correlations for both liquid and vapor, in addition to the Virial EoS to predict the vapor density. Section 4 and Section 5 are also focused on studying the effect of the non-equilibrium phase transition assumption on the model predictions. Lastly, Section 6 summarizes the main findings of this work and provides recommendations for future research.

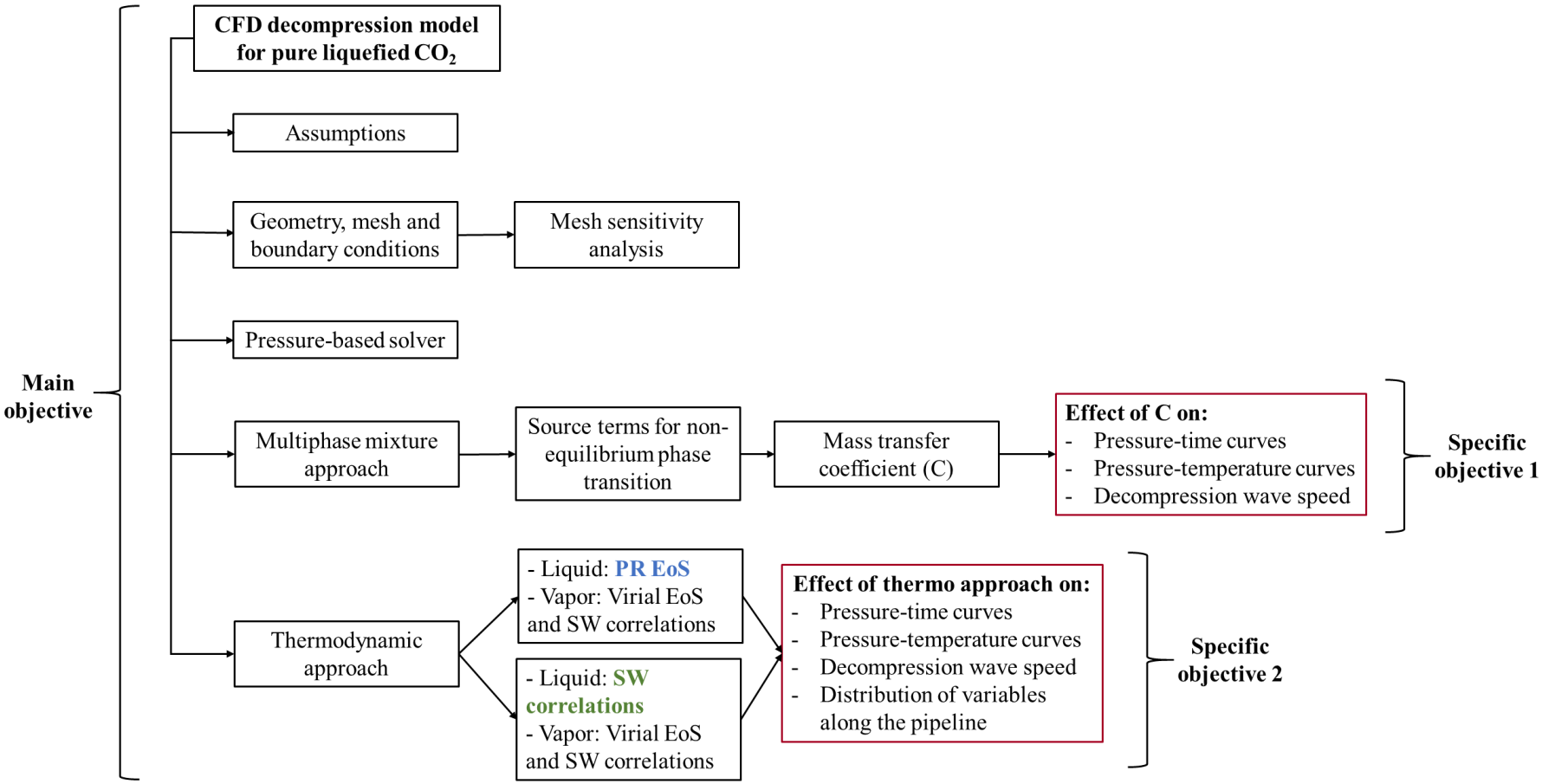

Figure 2-2. Research methodology.

3. DEVELOPMENT OF CFD DECOMPRESSION MODEL FOR LIQUEFIED CARBON DIOXIDE

3.1. Model assumptions

The system under study corresponds to the full-bore rupture of a horizontal pipeline filled with pure liquefied CO_2 under pressure. One of the ends of the pipeline is the closed-end (intact side) and the other is the open-end where the fluid exits the pipeline. It should be noted that the CFD model only represents the pipeline depressurization process; the jet expansion and dispersion are not included in the scope. The validation of the CFD methodology is performed with the results of the shock tube test 32A conducted by Botros *et al.* (2015) [15], in which the decompression behavior of pure liquefied CO_2 was experimentally studied.

The ANSYS Fluent software was used to develop the computational model. Different assumptions are implemented in ANSYS Fluent, which are related to the geometry, fluid properties, boundary conditions, solution initialization, and others. Some of the most important assumptions are listed below:

- The 2-D axisymmetric geometry is a rectangle with no subdivisions, although the shock tube test conducted by Botros *et al.* (2015) [15] consisted of four cylindrical pipe sections. The length (42 m) and width (19.05 mm) of the rectangle correspond to the total length and internal radius of the shock tube, respectively.
- To capture the abrupt change in flow properties during the unsteady depressurization, a time step of 10^{-6} s is incorporated in the model.

- Solution initialization is performed assuming that the fluid is at rest before the rupture. The fluid velocity when time equals zero is assumed to be negligible in comparison to the post-rupture velocity. In addition, the initial temperature (281.89 K) and pressure (11.27 MPa-a) are defined based on the initial conditions of the experiment. Also, the initial liquid volume fraction is equal to one throughout the CFD domain.
- An instantaneous rupture is assumed; nevertheless, it could have taken some time to completely burst the rupture disk while originating the open-end during the experiment.
- Adiabatic pipeline walls are included in the computational domain. Heat transfer between the fluid and the surroundings is neglected because of the short period of time considered in this study (milliseconds). In addition, the no-slip condition is implemented at the walls.
- Non-isentropic flow is assumed since friction effects are considered.
- Non-equilibrium phase transition is incorporated through the multiphase mixture model available in the pressure-based solver of ANSYS Fluent.
- Liquid and vapor phases are assumed to be compressible.
- Phase-slip is allowed. Therefore, the velocity of the liquid and vapor phases are different once the phase transition starts.
- The gravity effect is neglected due to the assumption of dispersed bubbly flow. The vapor that is formed is assumed to be dispersed over the high velocity liquid

exiting the system. Thus, the flow stratification phenomenon typically associated with pipeline puncture scenarios [17] is not included in the study.

- The realizable k-ε turbulence model is selected since previous researchers have implemented this formulation for high-speed decompression processes [5, 6].

The overall process of developing a CFD model in ANSYS Fluent consists of defining the computational domain with the creation of the geometry and mesh, choosing the solver (density-based or pressure-based), selecting the equations to solve, stablishing the materials, boundary conditions, solution methods, convergence criteria, and other assumptions. Once all the specifics have been incorporated in ANSYS Fluent, the next step is to initialize the numerical solution while monitoring model stability, to ensure that the residuals of the conservation equations reach certain threshold (convergence). Lastly, model accuracy is evaluated while comparing the CFD model predictions with corresponding experimental data. It should be emphasized that the previous description corresponds to a very general explanation of the methodology to develop a CFD model. The process usually involves significant challenges while defining the assumptions, creating the mesh, predicting accurate thermodynamic properties, programming User-Defined Functions (UDF) to add subroutines, and other subjects.

3.2. Solver selection

The description of the density-based and pressure-based solvers in ANSYS Fluent is reported in Section 1. In general, the density-based solver is used for high-speed flows with a strong dependence of density on pressure changes (compressible flows); therefore, its name derives from considering the density as a primary variable [59]. For low Mach

numbers (ratio of sound speed to flow speed), the density-based solver has proven to have significant accuracy issues and slow convergence [60]. On the other side, the pressure-based solver was originally developed for low speed incompressible flows, where pressure is considered a main dependent variable [59]. Nevertheless, the formulation of the pressure-based approach has been extended to solve compressible and incompressible flows from subsonic to supersonic conditions [61]. Besides, different multiphase models have been developed on the basis of the pressure-based formulation, including the volume-of-fluid (VOF) model [62, 63], the mixture model [5, 7, 12, 58] and the Eulerian multiphase approach [64].

Once the pipeline ruptures, the flow is expected to be subsonic inside the system, and sonic or supersonic at the outlet [65]. Therefore, the pressure-based solver is selected due to the variety of conditions to be modeled, in addition to its compatibility with multiphase formulations.

3.3. The multiphase mixture model

After the solver selection, the next step in the methodology is to choose the most appropriate multiphase approach based on their assumptions and formulation. In general, the volume-of-fluid model is used to track the interface between immiscible fluids. Its main focus is to model the position of the interface, being well used to capture the behavior of stratified flows (*e.g.*, air and water [66], oil and water [67]). In contrast, the mixture model is specialized in dispersed flows, such as continuous liquid with bubbles (bubbly flow), or continuous gas with droplets (droplet flow). Lastly, the Eulerian model is the most robust of the multiphase formulations available in ANSYS Fluent [36], considering

that it solves a set of continuity, momentum and energy equations for each phase. Similar to the mixture model, the Eulerian multiphase approach is recommended for dispersed flows.

The multiphase mixture model is implemented in this study since it is less computationally expensive (a smaller number of conservation equations is solved) and potentially more stable than the Eulerian multiphase approach, in addition to being more widely used in the literature on carbon dioxide depressurization.

3.3.1. Conservation equations

The multiphase mixture model solves a continuity, momentum and energy equations for the mixture of liquid and vapor. In addition, it solves a volume fraction equation for the secondary phase. In this study, the primary phase (continuous phase) is the liquid and the secondary phase (dispersed phase) is the vapor. The set of governing equations solved in ANSYS Fluent is shown next [36, 68]. The continuity equation for the mixture is:

$$\frac{\partial \rho_m}{\partial t} + \nabla \cdot (\rho_m \vec{u}_m) = 0 \qquad \textbf{(3-1)}$$

Where the subscript m refers to the mixture properties. Therefore, ρ_m is the mixture density and $\vec{u}_m$ is the mass-averaged velocity of the mixture. For a two-dimensional system, Equation (3-1) can be expressed as:

$$\frac{\partial \rho_m}{\partial t} + \frac{\partial}{\partial x}(\rho_m u_{m-x}) + \frac{\partial}{\partial y}\left(\rho_m u_{m-y}\right) = 0 \qquad \textbf{(3-2)}$$

Where the subscripts x and y correspond to the horizontal and vertical coordinate, respectively. Thus, u_{m-x} is the mixture velocity in x-direction and u_{m-y} is the mixture velocity in y-direction. The mixture density and the mixture velocity are defined as:

$$\rho_m = \sum_{k=1}^{2} \alpha_k \rho_k = \alpha_l \rho_l + \alpha_v \rho_v \quad \textbf{(3-3)}$$

$$\alpha_l + \alpha_v = 1 \quad \textbf{(3-4)}$$

$$\vec{u}_m = \frac{\sum_{k=1}^{2} \alpha_k \rho_k \vec{u}_k}{\rho_m} = \frac{\alpha_l \rho_l \vec{u}_l + \alpha_v \rho_v \vec{u}_v}{\rho_m} \quad \textbf{(3-5)}$$

$$u_{m-x} = \frac{\alpha_l \rho_l u_{l-x} + \alpha_v \rho_v u_{v-x}}{\rho_m} \quad \textbf{(3-6)}$$

$$u_{m-y} = \frac{\alpha_l \rho_l u_{l-y} + \alpha_v \rho_v u_{v-y}}{\rho_m} \quad \textbf{(3-7)}$$

Where the subscript k refers to each of the two phases. Additionally, α_l, α_v, ρ_l, ρ_v, $\vec{u}_l$, $\vec{u}_v$ are the liquid and vapor volume fractions, densities and velocities. It should be noted that the CFD model assumes that phase-slip occurs in both horizontal and vertical directions. Therefore, the velocity of the liquid and vapor phases are different once the phase transition starts. Nevertheless, the discrepancy between the liquid and vapor velocities in the horizontal direction (u_{l-x} and u_{v-x}) is expected to be more significant than the difference between the radial velocities (u_{l-y} and u_{v-y}).

The momentum equation for the mixture takes the form:

$$\frac{\partial(\rho_m \vec{u}_m)}{\partial t} + \nabla \cdot (\rho_m \vec{u}_m \vec{u}_m) = -\nabla P + \nabla \cdot [\mu_m (\nabla \vec{u}_m + \nabla \vec{u}_m^T)] + \rho_m \vec{g} +$$

$$\vec{F} + \nabla \cdot \left(\sum_{k=1}^{2} \alpha_k \rho_k (\vec{u}_k - \vec{u}_m)(\vec{u}_k - \vec{u}_m) \right) \quad \textbf{(3-8)}$$

Where $\rho_m \vec{g}$ and $\vec{F}$ are the gravitational body force and external body forces (*e.g.*, electric or magnetic fields), respectively; the contribution of the last two terms is assumed to be negligible. The liquid and vapor pressures are considered to be equal and identical to the mixture pressure (∇P). In addition, the last term of Equation (3-8) represents the momentum source term due to the phase-slip, where the subscript k refers to each of the phases (liquid and vapor). Lastly, μ_m is the viscosity of the mixture and is calculated as:

$$\mu_m = \sum_{k=1}^{2} \alpha_k \mu_k = \alpha_l \mu_l + \alpha_v \mu_v \quad \textbf{(3-9)}$$

The energy equation for the mixture is:

$$\frac{\partial}{\partial t} \sum_{k=1}^{2} (\alpha_k \rho_k E_k) + \nabla \cdot \sum_{k=1}^{2} \left(\alpha_k \vec{u}_k (\rho_k E_k + P) \right) = \nabla \cdot \left(k_{eff} \nabla T \right) +$$

$$\nabla \cdot \left(\bar{\bar{\tau}}_{eff} \cdot \vec{u} \right) + S_h \quad \textbf{(3-10)}$$

Where k_{eff} is the effective conductivity, which includes the ordinary and turbulent thermal conductivities; S_h is the heat source term related to the energy involved in the phase transition process. The term, $\nabla \cdot \left(\bar{\bar{\tau}}_{eff} \cdot \vec{u} \right)$, represents the viscous dissipation, which is important for high velocity systems due to the conversion of kinetic energy into internal

energy, leading to a potential heating of the fluid (viscous heating). Since the research scope does not include a multi-component flow, the transport of enthalpy due to species diffusion is not included. Additionally, there is no energy source term related to chemical reaction. In Equation (3-10), the total energy for each phase (E_k) is defined as follows:

$$E_k = i_k + \frac{u_k^2}{2} \rightarrow \ Since \ i_k = \ h_k - \frac{P}{\rho_k} \rightarrow E_k = h_k - \frac{P}{\rho_k} + \frac{u_k^2}{2} \qquad \textbf{(3-11)}$$

Where h_k and i_k are the specific enthalpy and specific internal energy for phase k, respectively.

A continuity equation for the secondary phase (vapor) is included in the mixture model formulation to obtain the volume fraction for this phase:

$$\frac{\partial}{\partial t}(\alpha_v \rho_v) + \nabla \cdot (\alpha_v \rho_v \vec{u}_m) = -\nabla \cdot \left(\alpha_v \rho_v \vec{u}_{dr,v}\right) + (S_e - S_c) \qquad \textbf{(3-12)}$$

Where $\vec{u}_{dr,v}$ is the drift velocity for the vapor phase, which is included in the equation due to the phase-slip assumption; S_e is the evaporation mass source term and S_c is the condensation mass source term. For a 2-D system, the second and third terms of Equation (3-12) are equal to:

$$\nabla \cdot (\alpha_v \rho_v \vec{u}_m) = \frac{\partial}{\partial x}(\alpha_v \rho_v u_{m-x}) + \frac{\partial}{\partial y}\left(\alpha_v \rho_v u_{m-y}\right) \qquad \textbf{(3-13)}$$

$$\nabla \cdot \left(\alpha_v \rho_v \vec{u}_{dr,v}\right) = \frac{\partial}{\partial x}\left(\alpha_v \rho_v u_{dr,v-x}\right) + \frac{\partial}{\partial y}\left(\alpha_v \rho_v u_{dr,v-y}\right) \qquad \textbf{(3-14)}$$

Where $u_{dr,v-x}$ and $u_{dr,v-y}$ are the drift velocities for the vapor phase in the horizontal and vertical direction, respectively. In addition, the drift velocity ($\vec{u}_{dr,v}$) is defined as the relative velocity ($\vec{u}_r$) minus the velocity of the mixture ($\vec{u}_m$). Lastly, the relative velocity is specified as the velocity of the secondary phase (vapor) relative to the velocity of the primary phase (liquid):

$$\vec{u}_{dr,v} = \vec{u}_r - \vec{u}_m \quad \textbf{(3-15)}$$

$$\vec{u}_r = \vec{u}_v - \vec{u}_l \quad \textbf{(3-16)}$$

For a two-dimensional system:

$$u_{dr,v-x} = u_{r-x} - u_{m-x} = (u_{v-x} - u_{l-x}) - \left(\frac{\alpha_l \rho_l u_{l-x} + \alpha_v \rho_v u_{v-x}}{\rho_m}\right) \quad \textbf{(3-17)}$$

$$u_{dr,v-y} = u_{r-y} - u_{m-y} = \left(u_{v-y} - u_{l-y}\right) - \left(\frac{\alpha_l \rho_l u_{l-y} + \alpha_v \rho_v u_{v-y}}{\rho_m}\right) \quad \textbf{(3-18)}$$

An algebraic formulation is used to obtain the relative velocity (also called slip velocity) in each direction. The details of how ANSYS Fluent calculates the slip velocity are explained in Manninen *et al.* (1996) [68].

In summary, the multiphase mixture model considers the mixture of liquid and vapor as a whole, formulating four mixture conservation equations of mass, momentum (horizontal and vertical directions) and energy, together with a fifth equation representing the continuity for the secondary (dispersed) phase [69].

3.3.2. Mass and energy source terms

The multiphase mixture model allows pieces of code called User-Defined Functions (UDFs) to be included to customize features of the CFD model. The UDFs are written in the C programming language. In this study, UDFs were programmed to model the volumetric source terms related to the phase transition. The evaporation (S_e) and condensation (S_c) mass source terms are incorporated in the continuity equation for the vapor phase (Equation (3-12)), while the energy source term (S_h) is included in the energy equation for the two-phase mixture (Equation (3-10)). The UDFs representing the source terms are based on pressure-driven mass and energy transfer terms, which are shown in Table 3-1. An example of a UDF is reported in Appendix A, which indicates how to calculate the mass transfer from the liquid to the vapor during the phase transition process.

Table 3-1. Mass and energy source terms.

Condition	Mass source term	Energy source term
$P \leq P_{sat}$	$S_e = C\alpha_l\rho_l \frac{P_{sat} - P}{P_{sat}}$ **(3-19)**	$S_h = -h_{lv}S_e$ **(3-21)**
$P > P_{sat}$	$S_c = C\alpha_v\rho_v \frac{P - P_{sat}}{P_{sat}}$ **(3-20)**	$S_h = h_{lv}S_c$ **(3-22)**

When $P \leq P_{sat}$ evaporation occurs and the mass source term (S_e) is equal to the mass transfer coefficient (C) times the volume fraction (α_l) and the density (ρ_l) of the liquid. This is further multiplied by the driving force of the interphase mass transfer, which is a normalized difference between the saturation pressure and the system's pressure. It is worth noting that the units of the evaporation and condensation mass source terms are

kg/m^3-s, while the mass transfer coefficient's unit is s^{-1}. In addition, the mass source terms in Equations (3-19) and (3-20) correspond to positive numbers, since the appropriate signs were previously incorporated in the continuity equation for the vapor phase.

The energy source term is equal to the mass source term times the heat of vaporization (h_{lv}) and has the units J/m^3-s. The heat of vaporization is the enthalpy of vapor at saturation conditions ($h_{v_{sat}}$) minus the enthalpy of saturated liquid ($h_{l_{sat}}$). The UDFs representing the source terms include expressions for both the heat of vaporization and the saturation pressure. The heat of vaporization is calculated as a function of temperature, using a second-order polynomial developed in this work, as follows:

$$h_{lv} = h_{v_{sat}} - h_{l_{sat}} = -22.4\,T^2 + 9200.6\,T - 614274.0 \qquad \textbf{(3-23)}$$

Equation (3-23) was obtained from a quadratic regression using the saturated liquid and saturated vapor enthalpies from 250 K to 280 K, employing data from the NIST Reference Fluid Thermodynamic and Transport Properties Database (REFPROP) [56], which incorporates the Span and Wagner EoS for CO_2 properties [37]. The units of h_{lv} are J/kg and the temperature in the polynomial is in Kelvin.

The correlation for the saturation pressure in MPa takes the following form:

$$P_{sat} = A_P + \frac{B_P}{T_r} + \frac{C_P}{T_r^2} + \frac{D_P}{T_r^3} + E_P\,T_r^2 \qquad \textbf{(3-24)}$$

Where T_r is the reduced temperature, defined as the ratio of temperature to critical temperature ($T_c = 304.128\,K$). In addition, the shape and the coefficients (A_P, B_P, C_P, D_P, E_P) of Equation (3-24) were obtained from a nonlinear regression using

data from the Span and Wagner EoS for CO_2, provided by NIST REFPROP; the data covered the temperature range from 250 K to 290 K. This method includes the comparison of the coefficient value with its standard error to verify that the former is significantly greater than the latter, ensuring that the 95% confidence interval of each coefficient does not go through zero. The values of the coefficients are as follows, A_P=-794.23, B_P=1230.76, C_P=-730.19, D_P=156.49, E_P=144.51. The details of how the correlation for the saturation pressure and other thermodynamic properties were developed are described in Section 3.4.

Despite the fact that evaporation and condensation mass source terms are included in the CFD model formulation, the analysis of the initial conditions ($\alpha_{v_{initial}} = 0$, $P_{initial} > P_{sat}$) show that since there is no initial vapor in the system, condensation would not occur, which is consistent with the evaporation source terms (Equations (3-19) and (3-21)) controlling the mass and energy interphase transport calculations.

This study incorporates non-equilibrium liquid vaporization through the mass and energy transfer involved in the phase transition. The evaporation source terms are equal to zero when saturation conditions are reached. Therefore, phase transition starts when $P < P_{sat}$, corresponding to non-equilibrium evaporation from the superheated liquid state. The prediction of thermodynamic properties at metastable conditions are explained in Section 3.4.

Literature suggests that the rupture of pipelines transporting liquefied CO_2 may lead to a phase transition occurring at a lower pressure than the equilibrium condition [70]. This may happen due to the extremely rapid expansion process, which may cause the

liquid to become temporarily superheated, with mass transfer between metastable liquid and vapor. Due to the short period of time modeled in this study (milliseconds), the non-equilibrium liquid-vapor transition is a phenomenon that should be considered.

Shock tube experiments with pure liquefied CO_2 have shown that phase change may occur at a pressure below equilibrium [13, 15], and thus previous researchers [12] have suggested that the value of the mass transfer coefficient (C) is an important parameter when modeling this non-equilibrium phase transition. However, it should be noted that the specific name, nomenclature and a comprehensive definition of this coefficient are not consistent throughout the literature. Liu *et al.* (2016) [5] referred to C as a 'time relaxation factor' employed to control the mass transfer from the liquid to the vapor phase. Giacomelli *et al.* (2018) [58] called it 'accommodation coefficient' or 'evaporation factor', mentioning that it can be understood as a relaxation time.

Different values of the mass transfer coefficient have been used for a variety of modeling applications. Wei *et al.* (2011) [71] implemented the volume-of-fluid method to model the boiling of water using a mass transfer coefficient of 100 s^{-1}, applying source terms where the driving force for the phase transition was the difference between the temperature and the saturation temperature. The same C value was incorporated by Yang *et al.* (2008) [63] to model the boiling of a refrigerant in a coiled tube. On the other hand, Wu *et al.* (2007) [64] implemented a coefficient equal to 0.1 s^{-1} while using the Eulerian multiphase model to study the flow of a boiling refrigerant. In the context of carbon dioxide, mass transfer coefficients have ranged from 10 s^{-1} to 1000 s^{-1} when implementing

pressure-driven interphase mass transfer [5, 12]; by contrast, it has achieved values as high as 10^5 s^{-1} when incorporating temperature-driven source terms [58].

In summary, the mass transfer coefficient (C) in the evaporation source terms may represent the evaporation rate, therefore, it has an impact on the amount of mass transferred from the liquid to the vapor phase. The influence of this coefficient on the predictions of the CFD model is further discussed in Section 4 and 5.

3.4. Thermodynamic and transport properties

The multiphase mixture model allows specification of thermodynamic and transport properties of the liquid and vapor phases separately. In this work, the properties of the vapor phase are predicted with a virial equation of state (vapor density) together with a series of correlations developed using data from the NIST Reference Fluid Thermodynamic and Transport Properties Database (REFPROP) [56], which incorporates the Span and Wagner (SW) EoS for CO_2 properties [37]. Additionally, two different approaches are implemented to predict the liquid phase properties. The first uses the Peng-Robinson EoS, while the second approach incorporates a series of correlations developed in this work, which are based on data from the Span and Wagner EoS.

3.4.1. Properties of the vapor phase

The density of the vapor phase is calculated with a virial equation of state using second and third virial coefficients, leading to a density-cubic equation (in three equivalent forms) as follows:

$$Z = 1 + B\rho_v + C\rho_v^2 \qquad \textbf{(3-25)}$$

$$\frac{P}{\rho_v RT} = 1 + B\rho_v + C\rho_v^2 \quad \textbf{(3-26)}$$

$$\rho_v^3 + \frac{B}{C}\rho_v^2 + \frac{1}{C}\rho_v - \frac{P}{CRT} = 0 \quad \textbf{(3-27)}$$

Where Z is the compressibility factor, ρ_v is the density of the vapor phase, and B and C are the second and third virial coefficients respectively, which are commonly expressed as expansions of the reciprocal reduced temperature $(1/T_r)$ [72-74]. In this study, the expressions for the second and third virial coefficients were obtained through data fitting using the nonlinear least-squares solver in Matlab. To perform the data fitting, five isotherms were used (250 K, 260 K, 275 K, 282 K and 290 K), with each isotherm spanning the pressure range from 0.1 MPa to the saturation pressure. The gas density data to develop the correlations was obtained from NIST REFPROP database which implements the SW EoS for CO_2 properties [37]. The virial coefficients take the following form:

$$B = \frac{B_{dim}}{\rho_c} \qquad C = \frac{C_{dim}}{{\rho_c}^2} \quad \textbf{(3-28)}$$

$$B_{dim} = x_1 + x_2\tau + x_3\tau^2 \quad \textbf{(3-29)}$$

$$C_{dim} = x_4 + x_5\tau \quad \textbf{(3-30)}$$

$$\tau = \frac{1}{T_r} = \frac{T_c}{T} \quad \textbf{(3-31)}$$

Where B_{dim} and C_{dim} are the dimensionless second and third virial coefficients, ρ_c and T_c are the critical density and critical temperature for CO_2 respectively, τ is the reciprocal of the reduced temperature, and x_1 to x_5 are the dimensionless coefficients obtained from the data fitting which are reported in Table 3-2.

Figure 3-1 illustrates the comparison between the vapor density calculated with the virial equation of state (this work) and the prediction of the SW EoS for the isotherms used to perform the fit.

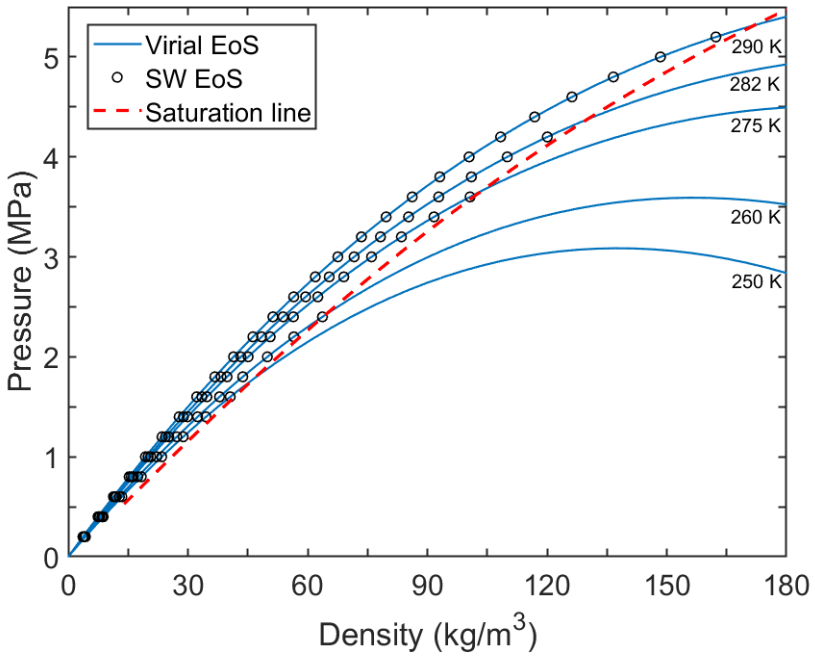

Figure 3-1. Vapor density: comparison between virial and SW EoS.

It should be highlighted that the thermodynamic and transport properties for the vapor phase were programmed in UDFs and compiled in ANSYS Fluent. Therefore, once the virial coefficients are calculated, the next step in the code is to determine the density roots of Equation (3-27). This is performed through an analytical scheme calculating a

discriminant, which allows identifying the number of real roots for the density function. If the discriminant is less than zero, three real roots exist and the code will take the smallest root as the vapor density. In contrast, if the discriminant is positive, only one real root is possible. Since the production of vapor starts when the pressure is below the saturation pressure (non-equilibrium phase transition assumption), three density roots will exist for pressures right below the saturation pressure to the spinodal point, while one real root will occur below the latter.

The correlation for the speed of sound of the vapor phase was obtained from data fitting through the nonlinear least-squares function in Matlab, using the same set of isotherms and pressure ranges as the ones used to develop the expressions for the second and third virial coefficients. Furthermore, data from the SW EoS was employed to obtain the optimal coefficients. The speed of sound correlation for the vapor phase is expressed as follows:

$$w_v = A_{sos,v} + B_{sos,v}\rho_r + C_{sos,v}\rho_r^2 \quad \textbf{(3-32)}$$

$$A_{sos,v} = y_1 + y_2 T_r + y_3 {T_r}^2 \quad \textbf{(3-33)}$$

$$B_{sos,v} = y_4 + y_5 T_r \quad \textbf{(3-34)}$$

$$C_{sos,v} = y_6 + y_7 T_r \quad \textbf{(3-35)}$$

Where w_v is the speed of sound of the vapor phase in m/s, ρ_r (ρ_v/ρ_c) and T_r (T/T_c) are the reduced vapor density and reduced temperature respectively, and y_1 to y_7 are the optimal coefficients obtained from the data fitting. Figure 3-2 shows the comparison

between the vapor speed of sound calculated with the correlation and the predictions of the SW EoS for the isotherms used to perform the data-fitting. As it is depicted in the figure, the speed of sound increases when the vapor density decreases.

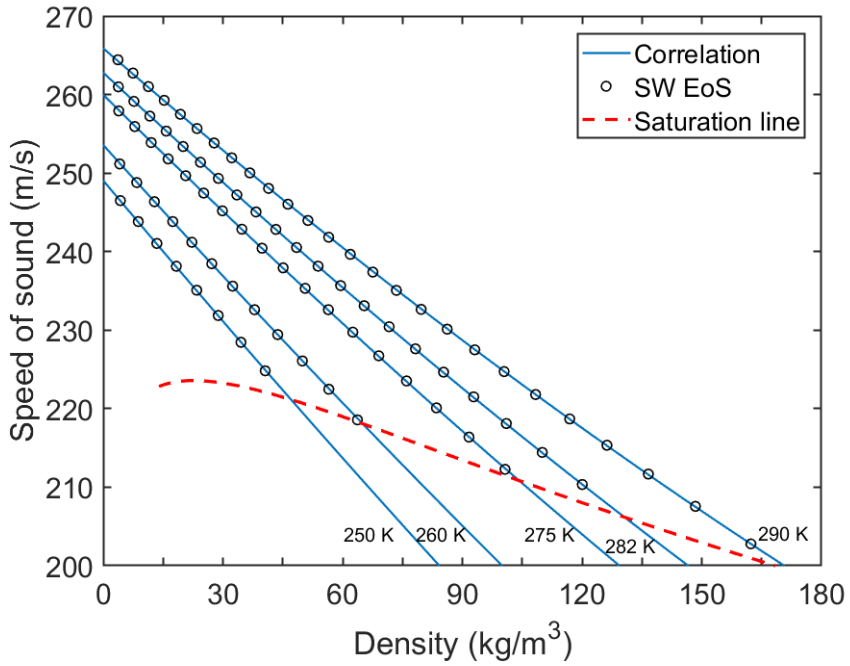

Figure 3-2. Vapor speed of sound: comparison between correlation and SW EoS.

The correlation for the specific heat of the vapor phase (C_{p_v}) was obtained from a fit using data from the SW EoS, covering the temperature range from 250 K to 290 K. The correlation for this thermodynamic property is as follows:

$$C_{p_v} = z_1 + \frac{z_2}{T_r} + \frac{z_3}{T_r^2} + \frac{z_4}{T_r^3} + z_5 T_r^2 \qquad \textbf{(3-36)}$$

C_{p_v} is the specific heat of the vapor phase in kJ/kg-K and z_1 to z_5 are the coefficients obtained from the data fitting. When programming the heat capacity correlation in the

UDF, a limitation of the macro used for such objective was identified. The DEFINE_SPECIFIC_HEAT macro in ANSYS Fluent only allows specification of a temperature-dependent function, so the specific heat cannot be a function of both the reduced density and reduced temperature as originally intended in this study. Therefore, to develop Equation (3-36), this work assumes that C_{p_v} is equivalent to the heat capacity of saturated vapor. Additionally, this macro automatically defines the enthalpy and entropy of the vapor phase as temperature integrals of the specific heat correlation. Figure 3-3 illustrates the comparison between the specific heat of saturated vapor calculated with the correlation and the prediction of the SW EoS.

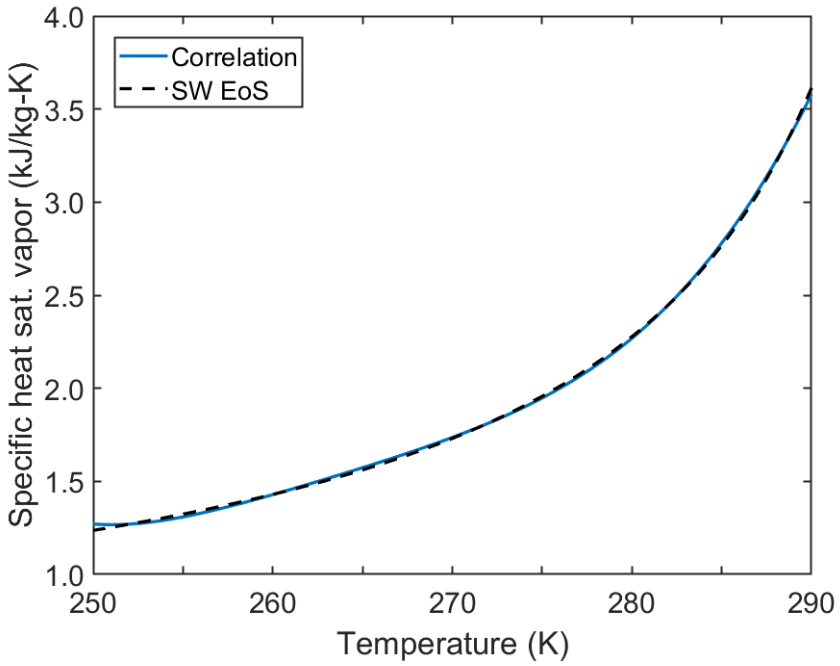

Figure 3-3. Saturated vapor specific heat: comparison between correlation and SW EoS.

For simplicity, the correlation for the thermal conductivity of the vapor phase was decided to be a function of temperature only. Hence, a correlation was developed from a fit using data from Vesovic *et al.* (1990) [75], covering the temperature range from 250 K to 290 K, assuming that the thermal conductivity of the vapor phase is equivalent to the conductivity of saturated vapor. The correlation takes the following form:

$$K_v = j_1 + j_2 T_r + j_3 {T_r}^2 + j_4 {T_r}^3 \qquad \textbf{(3-37)}$$

Where K_v is the thermal conductivity of the vapor phase in W/m-K and j_1 to j_4 are the optimal coefficients obtained from the fit. Figure 3-4 shows the comparison between the thermal conductivity of saturated vapor calculated with the correlation and the predictions of Vesovic *et al.* (1990) [75], the data for the latter is obtained from NIST REFPROP [56].

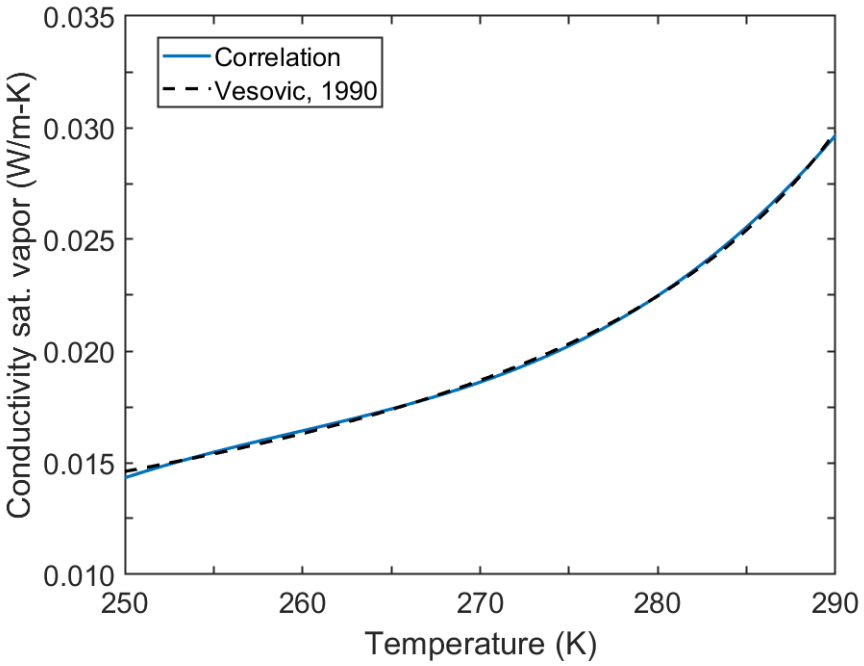

Figure 3-4. Saturated vapor thermal conductivity: comparison between correlation and Vesovic *et al.* (1990).

The same assumption used to obtain the thermal conductivity expression was applied when developing the correlation for the vapor viscosity. Therefore, the viscosity of the vapor phase is assumed to be equivalent to the vapor property at saturation conditions. A correlation was developed using data from Fenghour *et al.* (1998) [76] from 250 K to 290 K and it is expressed as:

$$\mu_v = f_1 + f_2 T_r + f_3 {T_r}^2 + f_4 {T_r}^3 \qquad \textbf{(3-38)}$$

Where μ_v is the viscosity of the vapor phase in g/cm-s and f_1 to f_4 are the optimal coefficients obtained from the data fitting. Figure 3-5 illustrates the comparison between the viscosity of saturated vapor calculated with the correlation and the predictions of Fenghour *et al.* (1998) [76], the data for the latter is obtained from NIST REFPROP [56].

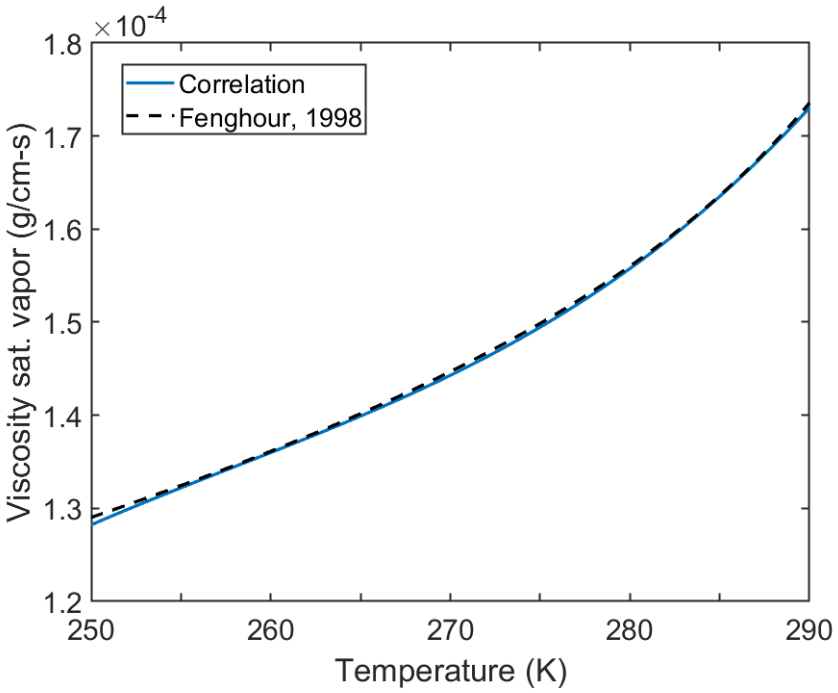

Figure 3-5. Saturated vapor viscosity: comparison between correlation and Fenghour *et al.* (1998).

The values of the coefficients in the correlations for the thermodynamic and transport properties of the vapor phase are reported in Table 3-2.

Table 3-2. Coefficients in correlations for the vapor phase.

Vapor phase property	Coefficients in correlation
Density (kg/m^3)	$x_1 = -0.864$ $x_2 = 1.956$ $x_3 = -2.348$ $x_4 = 0.439$ $x_5 = 0.128$
Speed of sound (m/s)	$y_1 = 67.582$ $y_2 = 300.750$ $y_3 = -97.301$ $y_4 = -759.370$ $y_5 = 579.11$ $y_6 = -12.035$ $y_7 = 89.187$
Specific heat (kJ/kg-K)	$z_1 = -26728.014$ $z_2 = 46229.372$ $z_3 = -29992.160$ $z_4 = 6919.492$ $z_5 = 3579.668$
Thermal conductivity (W/m-K)	$j_1 = -4.741$ $j_2 = 16.611$ $j_3 = -19.398$ $j_4 = 7.577$
Viscosity (g/cm-s)	$f_1 = -0.008$ $f_2 = 0.027$ $f_3 = -0.031$ $f_4 = 0.012$

In this work, it was decided to use the reduced temperature as one of the independent variables for the vapor correlations since it usually provides less order of magnitude coefficients, in comparison to the coefficients from a data-fitting using the temperature.

In summary, a total of four UDFs were programmed and compiled in the CFD model to predict thermodynamic and transport properties for the vapor phase. Since the speed of sound correlation can be included in the same computational code as the gas density, one UDF consists of the previous two properties, while the specific heat, thermal conductivity and viscosity are programmed in separate codes. Appendix B shows the UDFs developed in the C programming language for the calculation of the vapor properties. It should be noted that ANSYS Fluent requires the use of specific units for the outputs of the correlations, consequently the last lines of the UDFs include appropriate conversion factors.

Considering that the vapor phase is the secondary or dispersed phase in the multiphase model, in addition to the short period of time studied (milliseconds), the vapor volume fraction is expected to be significantly lower than the liquid fraction along the majority of the computation domain. Therefore, the accuracy of the prediction of the liquid properties may have a more significant impact on the CFD model calculations. In this work, one thermodynamic approach is incorporated to predict the vapor properties, which was explained in the current section. However, two thermodynamic approaches are implemented to understand the effect of the liquid properties' accuracy on the expansion predictions.

3.4.2. Properties of the liquid phase

This work includes two different thermodynamic approaches to predict the liquid phase properties in the CFD decompression model. The first uses the Peng-Robinson EoS as basis, the second comprises correlations developed from data fitting using the Span-Wagner EoS.

3.4.2.1. Implementation of Peng-Robinson EoS

The Peng-Robinson EoS is implemented to calculate the density, speed of sound and heat capacity of the liquid phase. The default version of the Peng-Robinson EoS available in ANSYS Fluent is chosen since it allows obtaining properties of metastable superheated liquid for pressure below the saturation conditions to the spinodal point [36]. Additionally, the enthalpy and entropy of the liquid phase are also derived from Peng-Robinson. The description of how different thermodynamic properties are calculated with this density-cubic equation is reported in Section 1.3.2. It should be highlighted that the PR EoS was implemented in the CFD model because of its relatively simple mathematical form, which potentially reduces the computational time. Nevertheless, the Span-Wagner EoS is widely known as the reference equation for pure CO_2. Therefore, this section compares the PR EoS predictions with the SW EoS to assess the accuracy of the former.

Figure 3-6 illustrates the liquid density predicted by the PR EoS (blue lines) compared to data from the SW EoS (black dots) obtained from NIST REFPROP [56]; five isotherms are used in the comparison (250 K, 260 K, 275 K, 282 K and 290 K). Besides, the saturation conditions predicted by the SW EoS are shown as a red dotted line, so the metastable liquid states correspond to the region below it. It is important to note that the

comparison does not extend to the CO_2 supercritical region, where the temperature is higher than 304.128 K and the pressure is higher than 7.377 MPa [56]. For the temperature and pressure ranges in Figure 3-6, discrepancies between the liquid density calculated with the PR and the SW EoS are observed.

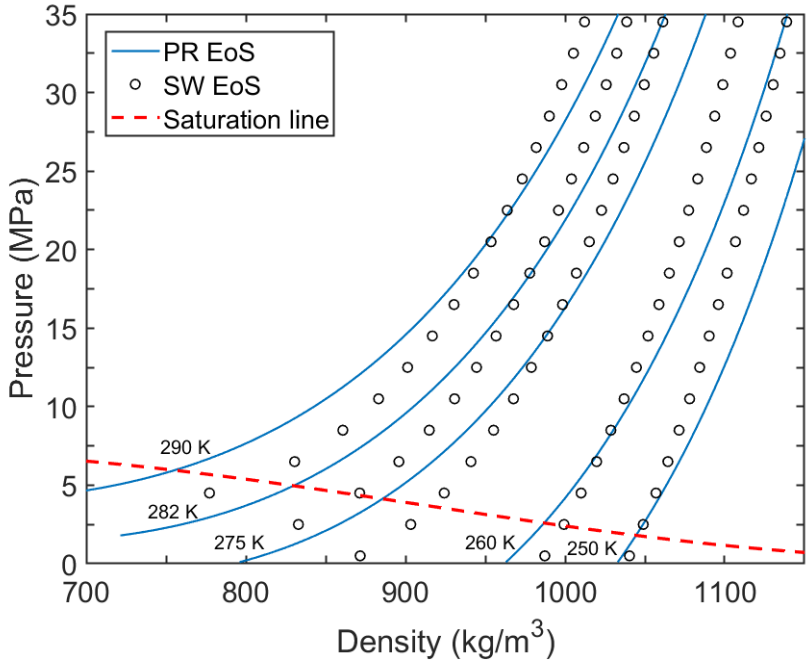

Figure 3-6. Liquid density: comparison between PR and SW EoS.

Figure 3-7 shows the comparison between the liquid speed of sound calculated with the PR and the SW EoS. The saturation conditions predicted by SW (saturated liquid density and speed of sound) are shown with a red dotted line. The PR EoS significantly underpredicts the liquid-phase speed of sound for densities higher than 900 kg/m^3.

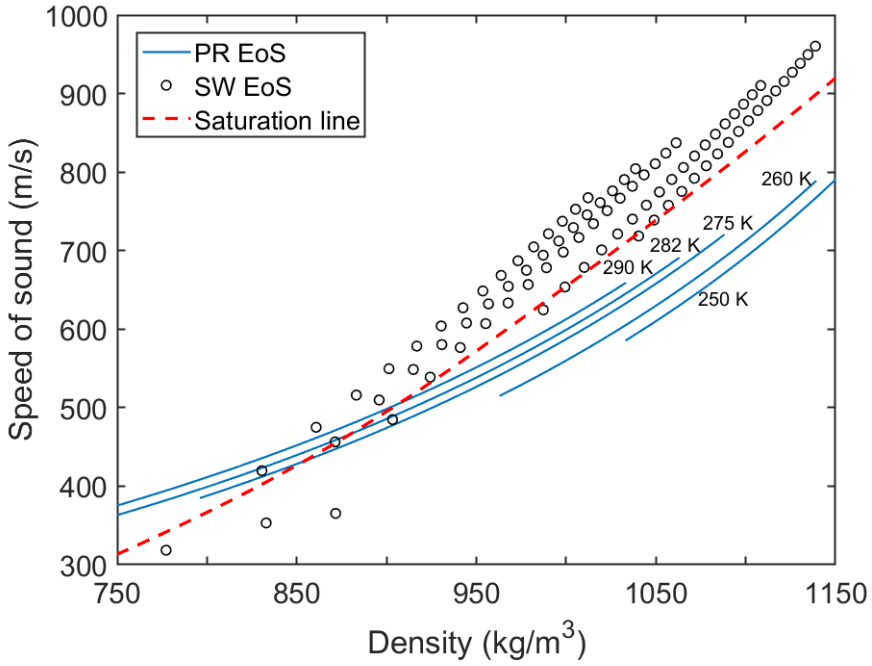

Figure 3-7. Liquid speed of sound: comparison between PR and SW EoS.

The comparison between the specific heat predicted by the PR and the SW EoS is depicted in Figure 3-8. The metastable liquid states correspond to the region above the red dotted line (SW saturation conditions). The PR EoS calculates the specific heat through the ideal gas heat capacity (C_p^{ideal}) and the residual function (C_p^r). The latter is derived from the EoS, while the former can be expressed as a function of temperature. In this work, the C_p^{ideal} (J/kg-K) is obtained from the following linear function, which was developed for a temperature range from 250 K to 290 K:

$$C_p^{ideal} = 1.09\,T + 518.67 \qquad \textbf{(3-39)}$$

$$C_p = C_p^{ideal} + C_p^r \qquad \textbf{(3-40)}$$

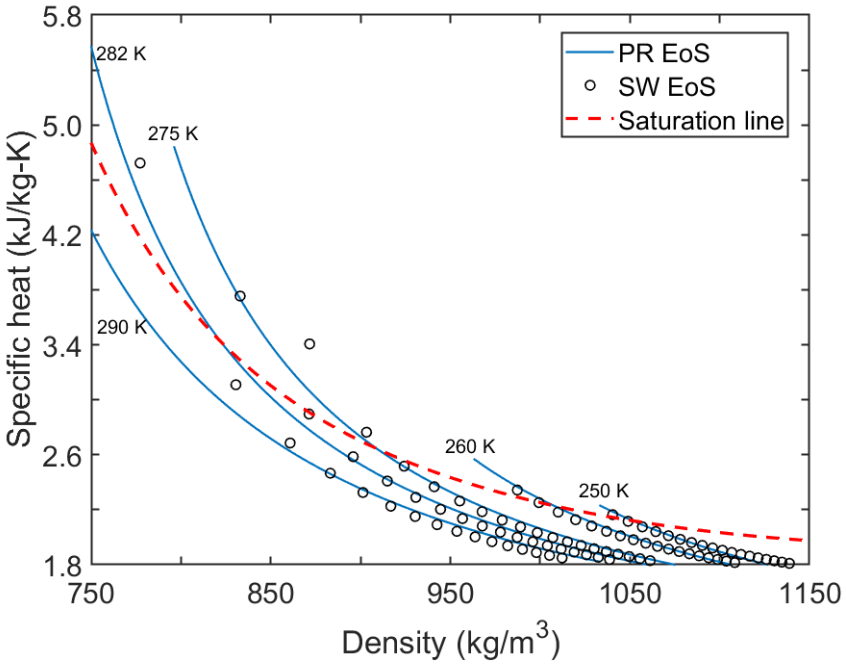

Figure 3-8. Liquid specific heat: comparison between PR and SW EoS.

The CFD model implementing the PR EoS also requires the prediction of transport properties for the liquid phase. Therefore, a correlation for the thermal conductivity of the liquid was developed as a function of temperature, assuming that this property is equivalent to the conductivity of saturated liquid. Vesovic *et al.* (1990) [75] was employed for the data fitting process, covering the temperature range from 250 K to 290 K. The correlation takes the following form:

$$K_l = u_1 + u_2 T_r \qquad \textbf{(3-41)}$$

Where K_l is the thermal conductivity of the liquid phase in W/m-K and u_1 to u_2 are the optimal coefficients obtained from the fit.

The assumption made to obtain the thermal conductivity expression was also applied when developing the correlation for the liquid viscosity. Thus, the viscosity of the liquid phase is assumed to be equivalent to the liquid property at saturation conditions. A correlation was developed using data from Fenghour *et al.* (1998) [76] from 250 K to 290 K and it is expressed as:

$$\mu_l = e_1 + e_2 T_r + e_3 {T_r}^2 + e_4 {T_r}^3 \qquad \textbf{(3-42)}$$

Where μ_l is the viscosity of the liquid phase in g/cm-s and e_1 to e_4 are the coefficients obtained from the data fitting.

The values of the coefficients in the correlations for the transport properties are reported in Table 3-3.

Table 3-3. Coefficients in correlations for the transport properties of the liquid phase.

Liquid phase property	Coefficients in correlation
Thermal conductivity (W/m-K)	$u_1 = 0.444$ $u_2 = -0.371$
Viscosity (g/cm-s)	$e_1 = 0.046$ $e_2 = -0.132$ $e_3 = 0.133$ $e_4 = -0.047$

3.4.2.2. Implementation of correlations based on Span-Wagner EoS

Since the accuracy of thermodynamic properties has a potential impact on the CFD model predictions, an important focus of this work is to model the CO_2 properties for the liquid phase (primary or continuous phase) through an efficient and reliable method. Consequently, a second approach was developed through the implementation of a series of correlations to predict the liquid properties based on data from the Span and Wagner EoS [37] collected from NIST REFPROP [56]. After the correlations were developed, these were programmed in a User-Defined Real Gas Model (UDRGM), which consists of a group of C programming language functions created by the ANSYS Fluent user. A total of 8 thermodynamic correlations as functions of reduced temperature (T_r) and reduced density (ρ_r) were developed and programmed in the UDRGM. These correlations were formulated based on data from 5 isotherms (250 K, 260 K, 275 K, 282 K and 290 K), while the pressure range extended from the spinodal point located below saturation conditions up to 35 MPa. Therefore, the process of developing correlations included data for the metastable liquid region, which were obtained from NIST REFPROP. The details of how to find metastable fluid states in NIST REFPROP are discussed in Lemmon *et al.* (2013) [56].

In addition to thermodynamic properties, the UDRGM for the liquid phase includes correlations for thermal conductivity and viscosity. The same correlations implemented in the PR CFD model for these liquid transport properties (Equations 3-41 and 3-42) were incorporated in the UDRGM approach.

In summary, correlations for the thermodynamic properties listed in Table 3-4 were developed for the liquid phase as functions of reduced temperature and reduced density, using the nonlinear least-squares function in Matlab. In contrast, correlations for the transport properties in Table 3-4 were developed as a function of temperature at saturated liquid conditions.

Table 3-4. Correlations in the UDRGM for the liquid phase.

Thermodynamic properties	• Density (ρ_l) • Enthalpy (h_l) • Entropy (s_l) • Specific heat at constant pressure (C_{p_l}) • Speed of sound (w_l) • $\left(\frac{\partial \rho}{\partial T}\right)_{P=const.}$ • $\left(\frac{\partial \rho}{\partial P}\right)_{T=const.}$ • $\left(\frac{\partial h}{\partial P}\right)_{T=const.}$
Transport properties	• Thermal conductivity (K_l) • Viscosity (μ_l)

It is worth noting that ANSYS Fluent allows compiling only one UDRGM when implementing multiphase approaches such as the mixture model. Since the liquid is assumed to be the continuous phase, a UDRGM was developed for the liquid while the properties of the vapor phase were calculated as described in Section 3.4.1. One of the most important advantages when implementing a UDRGM instead of multiple UDFs is

based on the fact that the former allows defining the specific heat, enthalpy and entropy not only as a function of temperature (as in the UDF approach), but as a two-variable function, *e.g.*, heat capacity as a function of temperature and density.

In the UDRGM, the density of the liquid phase is calculated with the following cubic correlation, using 16 coefficients:

$$P = A_{rho,l} + B_{rho,l}\rho_r + C_{rho,l}\rho_r^2 + D_{rho,l}\rho_r^3 \quad \textbf{(3-43)}$$

$$B_{rho,l} = x_1 + x_2\tau + + x_3\tau^2 + x_4\tau^3 \quad \textbf{(3-44)}$$

$$C_{rho,l} = x_5 + x_6\tau + x_7\tau^2 + x_8\tau^3 \quad \textbf{(3-45)}$$

$$D_{rho,l} = x_9 + x_{10}\tau + x_{11}\tau^2 + x_{12}\tau^3 \quad \textbf{(3-46)}$$

$$A_{rho,l} = x_{13} + x_{14}\tau + + x_{15}\tau^2 + x_{16}\tau^3 \quad \textbf{(3-47)}$$

$$\rho_r = \frac{\rho_l}{\rho_c} \qquad \tau = \frac{1}{T_r} = \frac{T_c}{T} \quad \textbf{(3-48)}$$

Where P is the pressure in MPa, ρ_r is the reduced liquid density, τ is the reciprocal of the reduced temperature, and x_1 to x_{16} are the optimal coefficients obtained from the data fitting which are reported in Appendix C. The roots of Equation (3-43) are dimensionless, therefore, the units of the density depend on the selected critical density. The largest root multiplied by the critical density represents the density of the liquid phase.

Figure 3.9 shows the liquid density predicted by the correlation developed in this work (blue lines) compared to data from the SW EoS (black dots) obtained from NIST REFPROP [56]; five isotherms are used in the comparison. The saturation conditions

predicted by the SW EoS are shown as a red dotted line, so the metastable liquid states correspond to the region below it. For the temperature and pressure ranges presented in Figure 3-9, the correlation successfully predicts the liquid density.

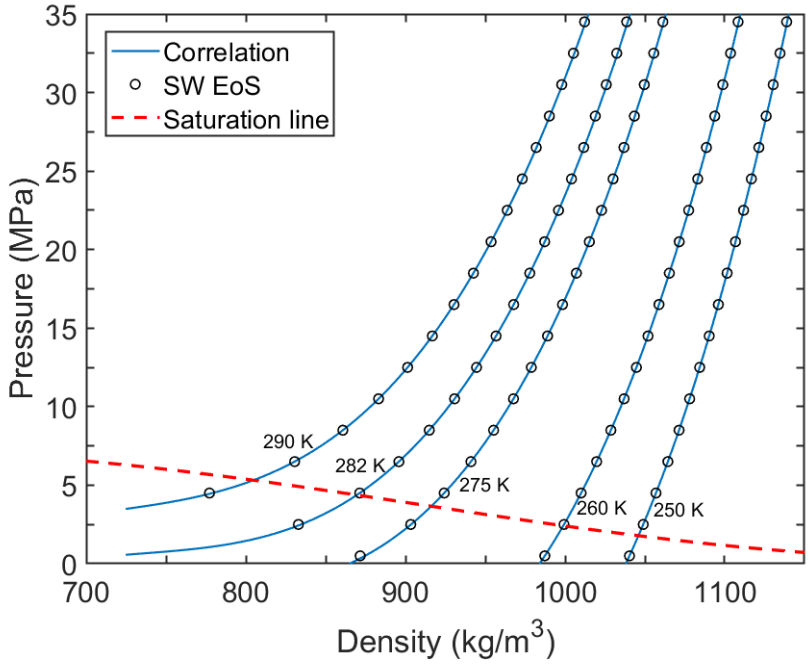

Figure 3-9. Liquid density: comparison between correlation and SW EoS.

The enthalpy of the liquid is calculated with the following correlation, implementing 12 coefficients:

$$h_l = A_{h,l} + B_{h,l}\rho_r + C_{h,l}\rho_r^2 + D_{h,l}\rho_r^3 \quad \textbf{(3-49)}$$

$$B_{h,l} = y_1 + y_2\tau + y_3\tau^2 \quad \textbf{(3-50)}$$

$$C_{h,l} = y_4 + y_5\tau + y_6\tau^2 \quad \textbf{(3-51)}$$

$$D_{h,l} = y_7 + y_8\tau + y_9\tau^2 \quad \textbf{(3-52)}$$

$$A_{h,l} = y_{10} + y_{11}\tau + y_{12}\tau^2 \quad \textbf{(3-53)}$$

Where h_l is the enthalpy of the liquid in kJ/kg and y_1 to y_{12} are the coefficients obtained from the data fitting. The reference enthalpy is added to the results of the correlation. In ANSYS Fluent, this reference value corresponds to the standard enthalpy of formation of CO_2 at 298.15 K ($\Delta_f h°_{gas}$ = -8943.64 kJ/kg). The comparison between the liquid enthalpy predicted by the correlation and the SW EoS is illustrated in Figure 3-10. The metastable liquid states correspond to the region to the left of the saturation line. For the temperature and density ranges in Figure 3-10, the correlation successfully predicts the liquid enthalpy. It should be noted that the reference enthalpy was added to the comparison.

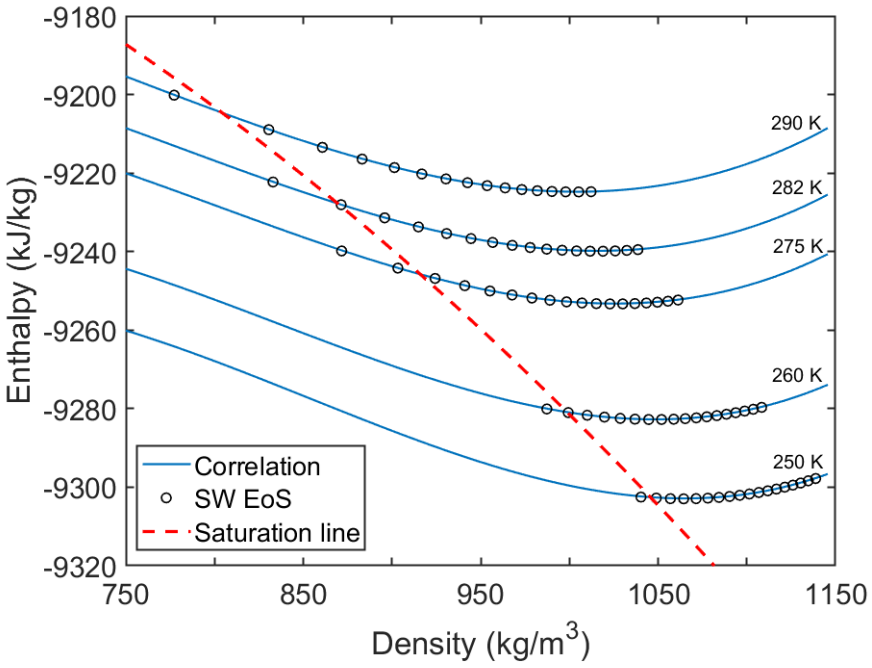

Figure 3-10. Liquid enthalpy: comparison between correlation and SW EoS.

The correlation to calculate the liquid entropy is expressed as:

$$s_l = A_{s,l} + B_{s,l}\rho_r + C_{s,l}\rho_r^2 \quad \textbf{(3-54)}$$

$$B_{s,l} = z_1 + z_2\tau + z_3\tau^2 + z_4\tau^3 \quad \textbf{(3-55)}$$

$$C_{s,l} = z_5 + z_6\tau + z_7\tau^2 + z_8\tau^3 \quad \textbf{(3-56)}$$

$$A_{s,l} = z_9 + z_{10}\tau + z_{11}\tau^2 \quad \textbf{(3-57)}$$

Where s_l is the entropy of the liquid in kJ/kg-K and z_1 to z_{11} are the optimal coefficients obtained from the data fitting. The reference entropy is added to the results of the correlation. In ANSYS Fluent, this reference value corresponds to the standard state entropy of CO_2 at 298.15 K and 1 bar ($s°_{gas}$= 4.86 kJ/kg-K). Figure 3-11 shows the comparison between the liquid entropy calculated with the correlation and the SW EoS. The correlation successfully predicts the entropy for the pressure and density ranges in Figure 3-11. It is worth to mention that the reference entropy was added to the comparison.

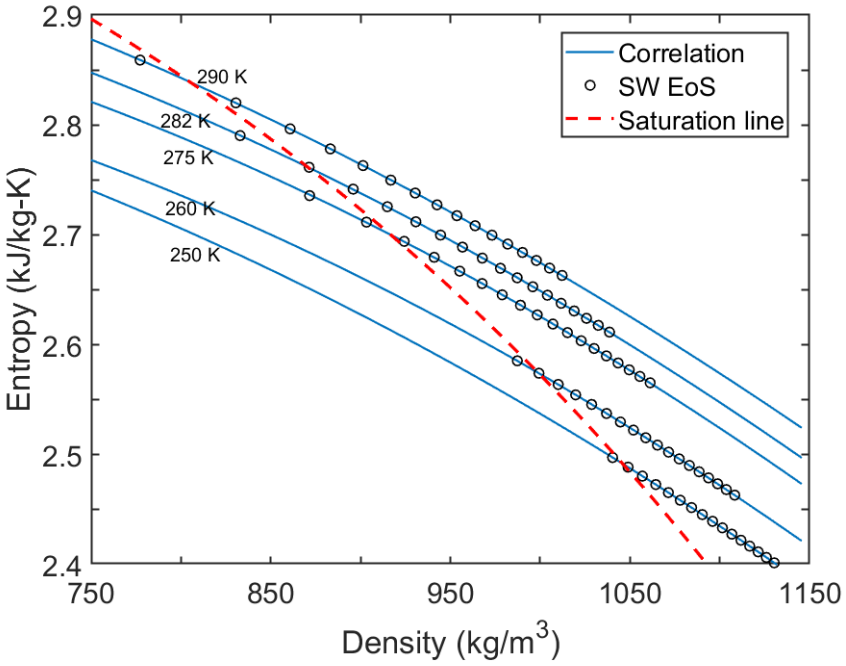

Figure 3-11. Liquid entropy: comparison between correlation and SW EoS.

The correlation for the specific heat of the liquid phase takes the following form:

$$C_{p_l} = A_{C_{p,l}} + B_{C_{p,l}}\rho_r + C_{C_{p,l}}\rho_r^2 + D_{C_{p,l}}\rho_r^3 + E_{C_{p,l}}\rho_r^4 + F_{C_{p,l}}\rho_r^5 \quad \textbf{(3-58)}$$

$$B_{C_{p,l}} = m_1 + m_2\tau + m_3\tau^2 \quad \textbf{(3-59)}$$

$$C_{C_{p,l}} = m_4 + m_5\tau + m_6\tau^2 \quad \textbf{(3-60)}$$

$$D_{C_{p,l}} = m_7 + m_8\tau^2 \quad \textbf{(3-61)}$$

$$E_{C_{p,l}} = m_9 + m_{10}\tau + m_{11}\tau^2 \quad \textbf{(3-62)}$$

$$F_{C_{p,l}} = m_{12} + m_{13}\tau + m_{14}\tau^2 \quad \textbf{(3-63)}$$

$$A_{C_p,l} = m_{15} + m_{16}\tau + m_{17}\tau^2 \quad \textbf{(3-64)}$$

Where C_{p_l} is the specific heat of the liquid in kJ/kg-K, and m_1 to m_{17} are the coefficients obtained from the data fitting. The comparison between the specific heat predicted by the correlation and the SW EoS is depicted in Figure 3-12. For the temperature and density ranges in the figure, the correlation predicts the liquid specific heat satisfactorily; some discrepancies are observed in the metastable liquid region above the saturation line.

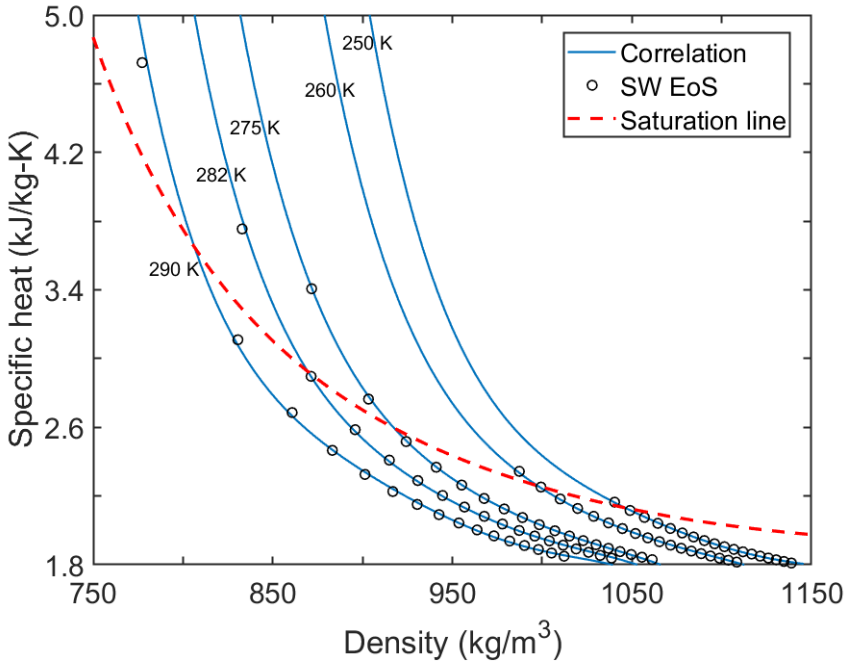

Figure 3-12. Liquid specific heat: comparison between correlation and SW EoS.

The speed of sound of the liquid phase is calculated with the following correlation:

$$\frac{1}{w_l} = A_{w,l} + B_{w,l}\rho_r + C_{w,l}\rho_r^2 + D_{w,l}\rho_r^3 + E_{w,l}\rho_r^4 \quad \textbf{(3-65)}$$

$$B_{w,l} = n_1 + n_2\tau + n_3\tau^2 \quad \textbf{(3-66)}$$

$$C_{w,l} = n_4 + n_5\tau + n_6\tau^2 \quad \textbf{(3-67)}$$

$$D_{w,l} = n_7 + n_8\tau \quad \textbf{(3-68)}$$

$$E_{w,l} = n_9 + n_{10}\tau + n_{11}\tau^2 \quad \textbf{(3-69)}$$

$$A_{w,l} = n_{12} + n_{13}\tau + n_{14}\tau^2 \quad \textbf{(3-70)}$$

Where w_l is the speed of sound of the liquid in m/s and n_1 to n_{14} are the optimal coefficients obtained from the data fitting. Figure 3-13 shows the comparison between the liquid speed of sound calculated with the correlation and the SW EoS. The correlation predicts the speed of sound satisfactorily for the pressure and density ranges in Figure 3-13; some discrepancies are observed in the metastable liquid region below the saturation line. The correlation improves the prediction of the liquid speed of sound in comparison to the Peng-Robinson EoS (Figure 3-7).

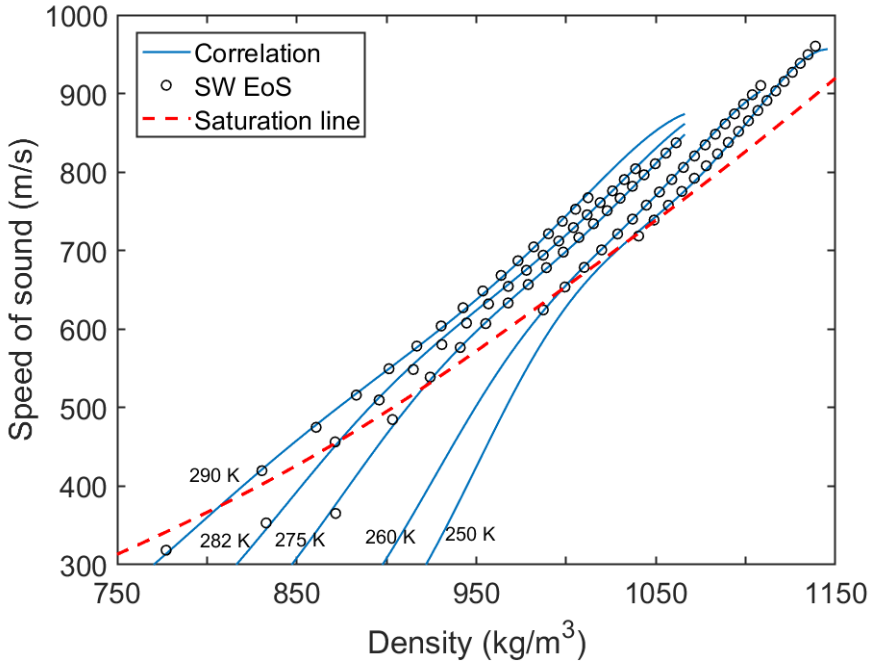

Figure 3-13. Liquid speed of sound: comparison between correlation and SW EoS.

The correlation for $\left(\frac{\partial \rho}{\partial T}\right)_P$ takes the following form:

$$\frac{1}{\left(\frac{\partial \rho}{\partial T}\right)_P} = A_{d\rho dT,l} + B_{d\rho dT,l}\rho_r + C_{d\rho dT,l}\rho_r^2 + D_{d\rho dT,l}\rho_r^3 + E_{d\rho dT,l}\rho_r^4 \quad \textbf{(3-71)}$$

$$B_{d\rho dT,l} = o_1 + o_2\tau + o_3\tau^2 \quad \textbf{(3-72)}$$

$$C_{d\rho dT,l} = o_4 + o_5\tau + o_6\tau^2 \quad \textbf{(3-73)}$$

$$D_{d\rho dT,l} = o_7 + o_8\tau + o_9\tau^2 \quad \textbf{(3-74)}$$

$$E_{d\rho dT,l} = o_{10} + o_{11}\tau + o_{12}\tau^2 \quad \textbf{(3-75)}$$

$$A_{d\rho dT,l} = o_{13} + o_{14}\tau + o_{15}\tau^2 \quad \textbf{(3-76)}$$

Where the units of $\left(\frac{\partial \rho}{\partial T}\right)_P$ are kg/m^3-K and o_1 to o_{15} are the optimal coefficients obtained from the data fitting.

The correlation for $\left(\frac{\partial \rho}{\partial P}\right)_T$ is expressed as:

$$\frac{1}{\left(\frac{\partial \rho}{\partial P}\right)_T} = A_{d\rho dP,l} + B_{d\rho dP,l}\rho_r + C_{d\rho dP,l}\rho_r^2 + D_{d\rho dP,l}\rho_r^3 + E_{d\rho dP,l}\rho_r^4 \quad \textbf{(3-77)}$$

$$B_{d\rho dP,l} = p_1 + p_2\tau + p_3\tau^2 \quad \textbf{(3-78)}$$

$$C_{d\rho dP,l} = p_4 + p_5\tau + p_6\tau^2 \quad \textbf{(3-79)}$$

$$D_{d\rho dP,l} = p_7 + p_8\tau + p_9\tau^2 \quad \textbf{(3-80)}$$

$$E_{d\rho dP,l} = p_{10} + p_{11}\tau + p_{12}\tau^2 \quad \textbf{(3-81)}$$

$$A_{d\rho dP,l} = p_{13} + p_{14}\tau + p_{15}\tau^2 \quad \textbf{(3-82)}$$

Where the units of $\left(\frac{\partial \rho}{\partial P}\right)_T$ are kg/m^3-MPa and p_1 to p_{15} are the coefficients from the fit.

The correlation for $\left(\frac{\partial H}{\partial P}\right)_T$ takes the following form:

$$\left(\frac{\partial H}{\partial P}\right)_T = A_{dHdP,l} + B_{dHdP,l}\rho_r + C_{dHdP,l}\rho_r^2 + D_{dHdP,l}\rho_r^3 + E_{dHdP,l}\rho_r^4 \quad \textbf{(3-83)}$$

$$B_{dHdP,l} = q_1 + q_2\tau + q_3\tau^2 \quad \textbf{(3-84)}$$

$$C_{dHdP,l} = q_4 + q_5\tau + q_6\tau^2 \quad \textbf{(3-85)}$$

$$D_{dHdP,l} = q_7 + q_8\tau + q_9\tau^2 \quad \textbf{(3-86)}$$

$$E_{dHdP,l} = q_{10} + q_{11}\tau + q_{12}\tau^2 \quad \textbf{(3-87)}$$

$$A_{dHdP,l} = q_{13} + q_{14}\tau + q_{15}\tau^2 \quad \textbf{(3-88)}$$

Where the units of $\left(\frac{\partial H}{\partial P}\right)_T$ are kJ/kg-MPa and q_1 to q_{15} are the optimal coefficients obtained from the data fitting.

The correlations for the liquid transport properties (thermal conductivity and viscosity) incorporated in the UDRGM correspond to Equations 3-41 and 3-42. In addition, the values of the coefficients in the correlations presented in this section are reported in Appendix C.

3.5. Full-bore rupture geometry and boundary conditions

The 2-D axisymmetric geometry representing the full-bore rupture depressurization was created using ANSYS DesignModeler, it consists of the interior of the pipeline, closed-end, open-end, upper wall and axis of symmetry. Figure 3-14 illustrates the geometry and boundary conditions.

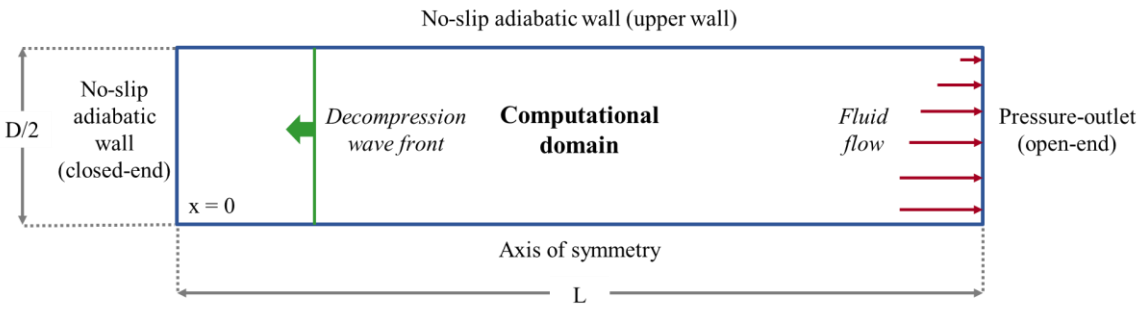

Figure 3-14. Geometry and boundary conditions in the CFD model.

To reduce computational time, the geometry is assumed to be axisymmetric with respect to the horizontal axis. Therefore, the CFD domain includes the upper half of the pipeline diameter, considering that the lower half is a mirror image of the former. Since a full-bore depressurizations is commonly associated with fully dispersed flow inside the pipeline (no flow stratification) [17], the axisymmetric condition is an appropriate assumption. This research addresses the transport phenomena in the pipeline, and thus the following boundary conditions were incorporated in the CFD model:

- Closed-end: No-slip wall and heat flux equal zero (adiabatic).
- Upper wall: No-slip wall and heat flux equal zero (adiabatic).
- Axis of symmetry.
- Open-end: Pressure-outlet boundary condition. The fluid is assumed to be exposed to ambient pressure (0.101325 MPa) at this borderline.

As depicted in Figure 3-14, once the pipeline ruptures, carbon dioxide flows from left to right, while a decompression wave is generated at the outlet and moves in the

opposite direction of the flow. This decompression wave initiates a pressure decrease when arriving at different locations along the pipeline.

To validate the CFD model, the geometry corresponds to the shock tube dimensions reported by Botros *et al.* (2015) [15]. The total length is 42 m and the internal radius is 19.05 mm. However, it should be noted that when performing the CFD simulations, the length of the geometry was reduced with the purpose of minimizing computational time, ensuring that the decompression wave would not reflect at the closed-end during the simulated time. This is accomplished by calculating a generic decompression wave speed, dividing the length traveled by the wave front, by the time taken to reach that location. Then, this generic expansion wave speed is multiplied by the targeted time, and thus the minimum geometry length is obtained. The previous approach is implemented to create the geometries to achieve the results in Section 4 and Section 5. This method has significant benefits since the computational time is considerably reduced, avoiding the use of high-performance computing clusters. Because the post-processing of the results does not include integrals over the computational domain, the predictions of the CFD model are not impacted by the shorter length of the geometry, as illustrated in Appendix D.

For the CFD formulation incorporating the Peng-Robinson EoS to predict thermodynamic properties of CO_2 liquid phase, the length of the computational domain is 5.5 m, so the model reached 10.5 ms (modeling time) without the decompression wave reflecting at the closed-end. As will be discussed in Section 5, the results using the CFD model implementing correlations based on Span-Wagner EoS showed an improvement in

the predictions, therefore, a larger geometry was created for the SW approach to reach longer modeling times; a 9 m long geometry was used to reach 15 ms. Although the length of the geometry depends on the thermodynamic approach and the aimed modeling time, the width of the rectangular domain equals the internal radius of the shock tube experimental set-up for all cases (19.05 mm).

Monitor points corresponding to the locations of pressure transducers in the shock tube test 32A from Botros *et al.* (2015) [15] are created in ANSYS Fluent to record the transient behavior of variables along the pipeline, including the pressure, temperature, velocity, speed of sound, liquid volume fraction, and others. The data obtained with these monitor points is used to compare model performance with experimental results (model validation), in addition to conduct further analysis of the decompression phenomenon. The discussion of the results is reported in Section 4 and Section 5.

3.6. Mesh description and sensitivity analysis

The mesh or grid, which is the domain used to solve the algebraic form of the conservation equations is created using ANSYS Meshing. The modeling of highly transient high-speed flows such as the full-bore rupture of a pressurized pipeline demands a very fine mesh and a small time step [3]. As a meshing strategy, smaller cells are created at the open-end and upper wall, due to the high pressure and velocity gradients at those regions once the depressurization starts. The mesh is constructed using inflation layers to generate smooth changes in the cell size. In addition, a mesh sensitivity analysis was performed to confirm that a mesh independent solution is obtained.

3.6.1. Mesh configuration

To build the mesh for this study, the geometry was divided into 4 sections using a face split function. These divisions simplified the application of different inflation options in each of those areas, which allowed the creation of smaller cells at the outlet and at the upper wall. Adjacent to the outlet, 13 layers of cells were created to capture the abrupt change in flow properties once the expansion starts. Simultaneously, 8 layers of cells were built next to the upper wall to capture the large velocity gradient. The first layer was set at 0.5 mm from both the outlet and the upper wall. The length and width of the first layer were inflated using a growth rate of 1.2, meaning that the dimensions increase 20% with respect to the adjacent element. To build the mesh beyond the inflation layers B. Liu *et al.* (2018) [12] was used as guidance, and thus the cells' dimensions remained constant with 2 mm in the vertical direction and 5 mm in the horizontal direction. It is worth to mention that all cells in the domain are quadrilateral. The approach adopted to build the mesh is summarized in Figure 3-15.

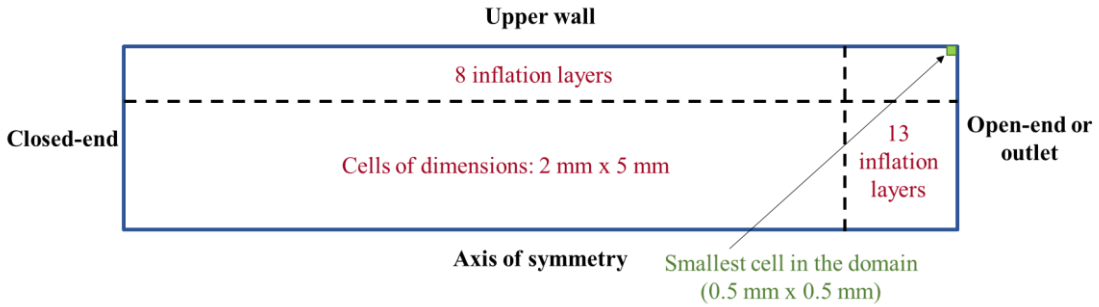

Figure 3-15. Approach to create the mesh.

The previous meshing strategy was implemented to create the grid for both the CFD model incorporating the Peng-Robinson EoS and the one implementing correlations

based on the Span-Wagner EoS to predict thermodynamic properties of the liquid. As described in Section 3.5., the length of the geometry was reduced in comparison to the shock tube length (42 m) reported by Botros *et al.* (2015) [15] for the purpose of minimizing computational time. Therefore, the length of the computational domain is 5.5 m for the PR model and 9.0 m for the SW approach. Consequently, the total number of cells in the mesh varies in these two models. For the PR approach, the mesh consisted of 15,526 cells, while the model incorporating SW correlations implemented a mesh of 25,326 elements. Figure 3-16 shows the two-dimensional mesh near the open-end; the complete length of the domain is not depicted in the figure. This mesh configuration is common for both thermodynamic approaches.

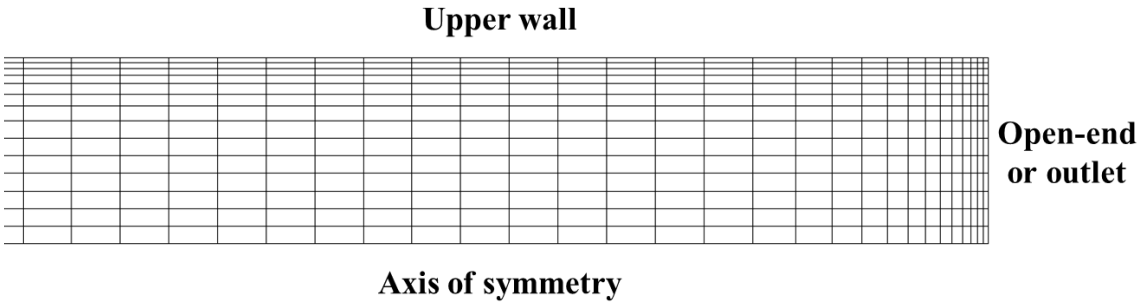

Figure 3-16. Two-dimensional mesh near the open-end.

3.6.2. Mesh sensitivity analysis

The mesh configuration in Section 3.6.1. was chosen after conducting a mesh sensitivity analysis using the PR approach, incorporating three different meshes. The smallest cell in the domain, located where the upper wall and open-end intersect was varied, and therefore the configuration of the inflation layers in the horizontal and vertical directions. Beyond the inflation layers, the cells' dimensions remained constant (2 mm x

5mm) for all tested meshes. Table 3-5 reports the description of the grids used in the sensitivity analysis. It is worth to mention that the mesh described in Section 3.6.1. corresponds to Mesh #2. The comparison of the results at PT1 location (0.0295 m from open-end) using the PR model and different meshes is illustrated in Figure 3-17.

Table 3-5. Meshes for sensitivity analysis.

Mesh #	First element	Growth rate	Cells at the bulk	Number of elements (42 m)	Stability
1	1.0 mm	1.2	2 mm x 5 mm	92455	Stable residuals
2	0.5 mm	1.2	2 mm x 5 mm	117726	Stable residuals
3	0.1 mm	1.2	2 mm x 5 mm	185174	Stable residuals

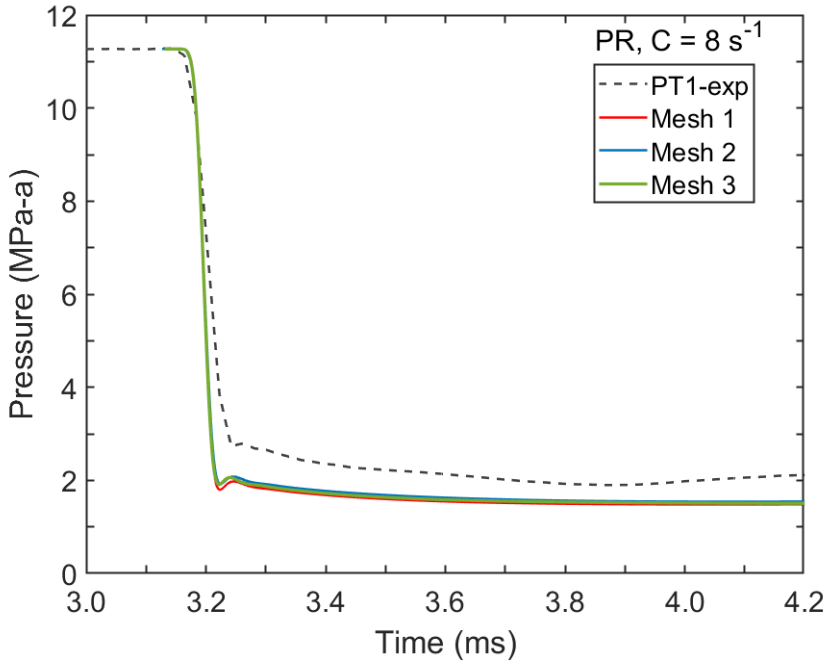

Figure 3-17. Comparison of predictions at PT1 using different meshes, C = 8 s^{-1}.

Although Mesh #3 is the most refined grid, Figure 3-17 shows that there is no significant difference between the results obtained employing Mesh #2 and Mesh #3. Therefore, Mesh #2 allows obtaining a prediction with sufficient resolution, and consequently the configuration of this mesh is employed in this work.

3.7. Summary

Figure 3-18 summarizes how the CFD decompression model based on the multiphase mixture approach allows performing a study on the effect of the accuracy of the liquid thermodynamic properties and the impact of the mass transfer coefficient (C) on the model predictions.

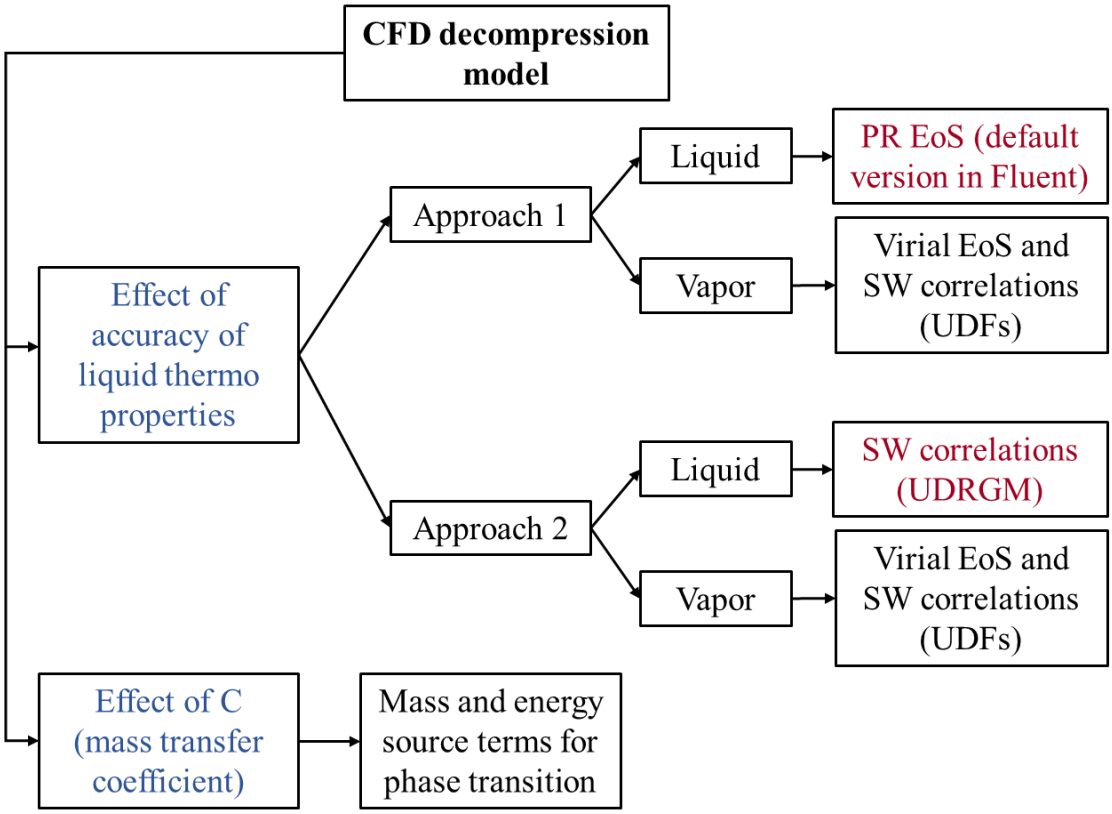

Figure 3-18. CFD decompression model approach.

4. CFD DECOMPRESSION MODEL IMPLEMENTING PENG-ROBINSON EOS

4.1. Thermodynamic approach

In this section, the results corresponding to the CFD model that implements a set of thermodynamic and transport properties through independent UDFs for the vapor phase, and the Peng-Robinson EoS for the liquid are discussed.

4.2. Model results

4.2.1. Model validation: pressure-time traces

The validation of the CFD model is conducted using test 32A from Botros *et al.* (2015) [15]. This pure CO_2 test was performed using a shock tube with total length of 42 m and 38.1 mm of internal diameter. The initial conditions before the full-bore rupture corresponded to pressurized liquefied CO_2 at 11.27 MPa-a and 281.89 K. For the transient pressure profiles, Botros *et al.* (2015) [15] noted that time zero was arbitrary; data acquisition during the experiment started before the rupture of the burst disk at the front end of the shock tube. Therefore, the time when the pressure starts to decrease at the PT1 location (3.1 ms) was used as a reference point to compare the CFD results of this work with the experimental pressure-time traces.

Figure 4-1 to Figure 4-4 show the comparison between model predictions (solid lines) and experimental results (dotted lines) for the pressure-time profiles out to 5 ms. The multiphase CFD model included four different values for the mass transfer coefficient, C = 8 s^{-1}, 25 s^{-1}, 100 s^{-1} and 1000 s^{-1}. This comparison includes the

experimental measurements at five pressure transducers near the exit plane (PT1, PT1A, PT1B, PT2 and PT3). The location of the monitor points is reported in Table 4-1.

Table 4-1. Location of pressure transducers in test 32A from Botros *et al.* (2015) [15].

Location	Distance from open-end (m)
PT1	0.0295
PT1A	0.0924
PT1B	0.1028
PT2	0.2
PT3	0.35
PT4	0.5
PT5	0.7
PT6	0.9
PT7	1.1
PT8	3.1
PT9	5.1
PT10	7.1
PT11	9.1

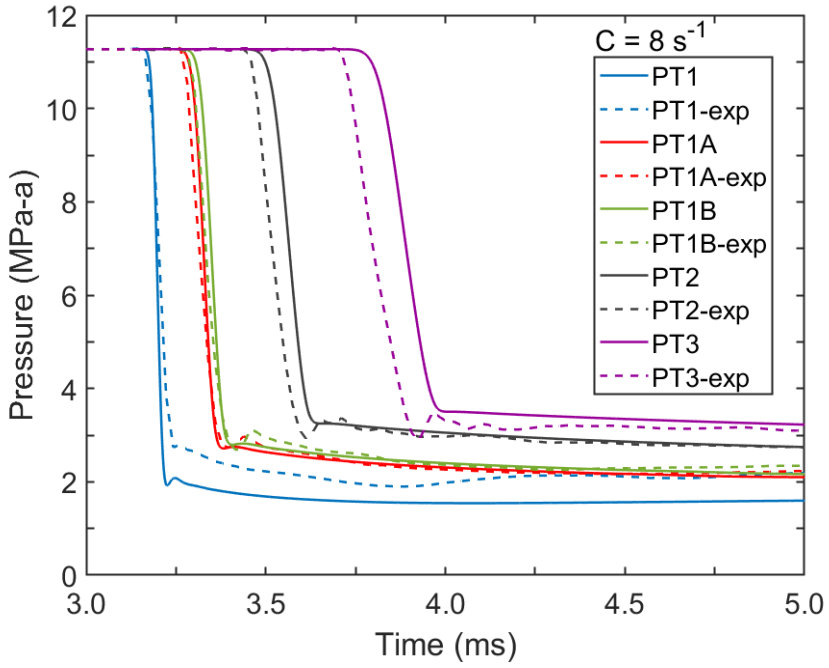

Figure 4-1. Comparison of predicted and experimental pressure-time curves at different positions, C = 8 s^{-1}.

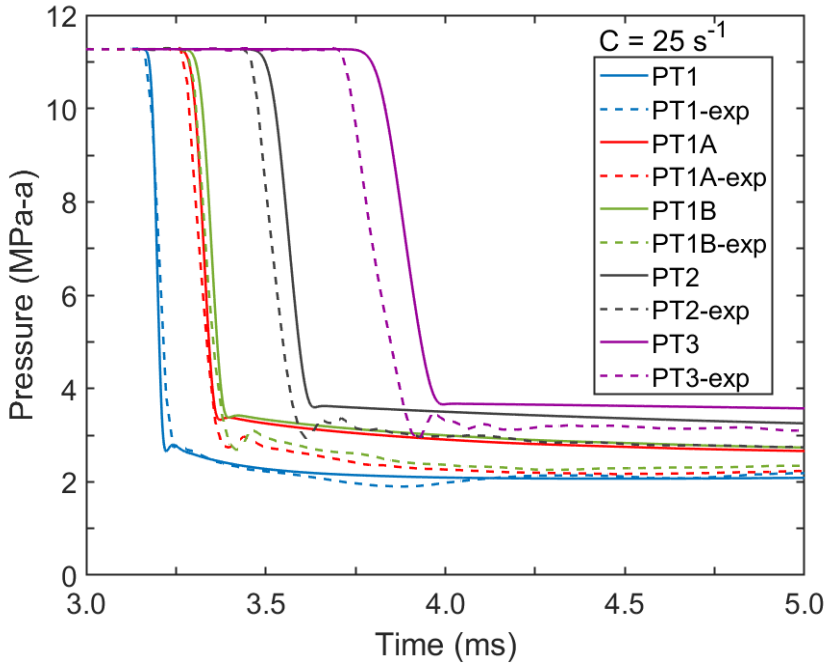

Figure 4-2. Comparison of predicted and experimental pressure-time curves at different positions, C = 25 s^{-1}.

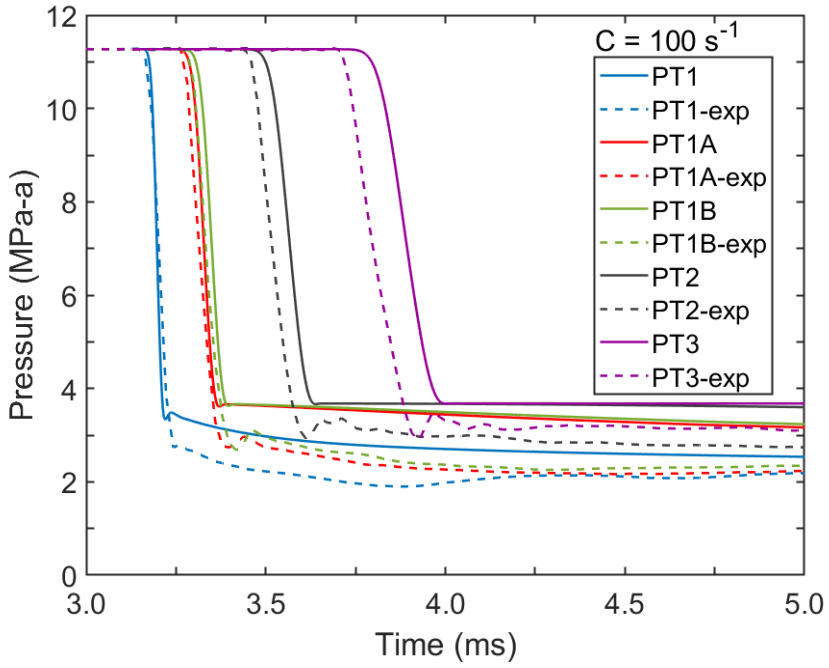

Figure 4-3. Comparison of predicted and experimental pressure-time curves at different positions, C = 100 s^{-1}.

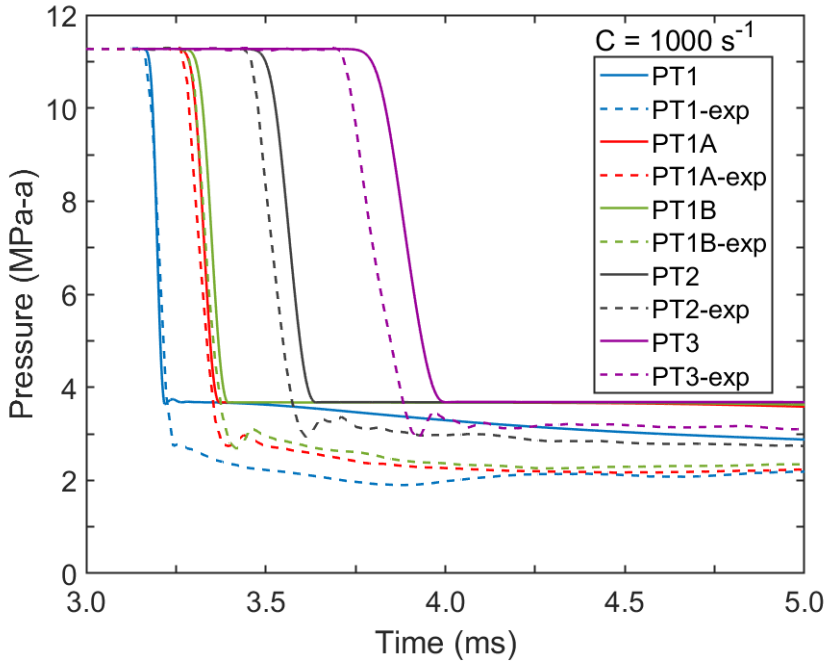

Figure 4-4. Comparison of predicted and experimental pressure-time curves at different positions, C = 1000 s^{-1}.

Both predicted and experimental pressure profiles show an initial fast pressure drop, which corresponds to the arrival of the decompression wave at each of the pressure transducers' locations. The time taken by the wave front to arrive at each transducer does not vary significantly for different values of the mass transfer coefficient (C). For example, the model predicts that the pressure drop at PT2 starts around 3.5 ms, independently of the C value incorporated in the CFD formulation. Therefore, the mass transfer coefficient may not have a significant impact on the arrival time of the wave front at each monitor point.

Discrepancies between predicted and measured pressure-time traces are evidenced in the region corresponding to the initial pressure drop. The model prediction shows a delay in the arrival time of the decompression wave at the pressure transducers compared to the measured data. A greater delay is observed as the distance from the open-end increases. For pressure transducers located farther from the outlet (*e.g.*, PT2 and PT3), there is a greater delay in the model prediction with respect to the experimental data. A discussion about the reasons for this delay is reported in following sections of this work.

After the initial pressure drop, a pressure plateau is formed. This plateau corresponds to the phase transition phenomenon. According to the CFD model, the mass transfer coefficient has a significant effect on the development of this pressure response. A higher value of C results in pressure plateaus that are higher in pressure, corresponding to a faster phase transition from liquid to vapor. In general, the results show that small C values ($C \leq 25\ s^{-1}$) lead to better agreement with the experiment. On the contrary, a significant over-prediction of the plateaus at the five monitor points' locations is observed when $C = 100\ s^{-1}$ and $C = 1000\ s^{-1}$.

Previous researchers have discussed the importance of modeling the depressurization using a fine-tuned C value that matches the experimental results [7, 12]. This work shows that during the first 5 ms, the mass transfer coefficient that better predicts the pressure plateau at locations PT1A, PT1B, PT2 and PT3 corresponds to C = 8 s^{-1}. On the other hand, the best C value that matches PT1 profile during this time interval is C = 25 s^{-1}.

To better understand the behavior of the CFD model in latter stages of the depressurization, a simulation was performed to analyze the pressure-time traces out to 12 ms. The results implementing a mass transfer coefficient C = 8 s^{-1} are shown in Figure 4-5. After 12 ms, the expansion wave has traveled to the PT8 location. Consistent with Figure 4-1 through Figure 4-4, as the distance from the open-end to the pressure transducer increases, there is (as would be expected) an increase in the arrival time of the decompression wave but also, there is an increasingly longer delay between the predicted and the measured decompression wave. Therefore, the CFD model incorporating the Peng-Robinson EoS predicts longer arrival times of the expansion wave in comparison to the experiment, showing more significant discrepancies as the distance from the open-end to the monitor point increases.

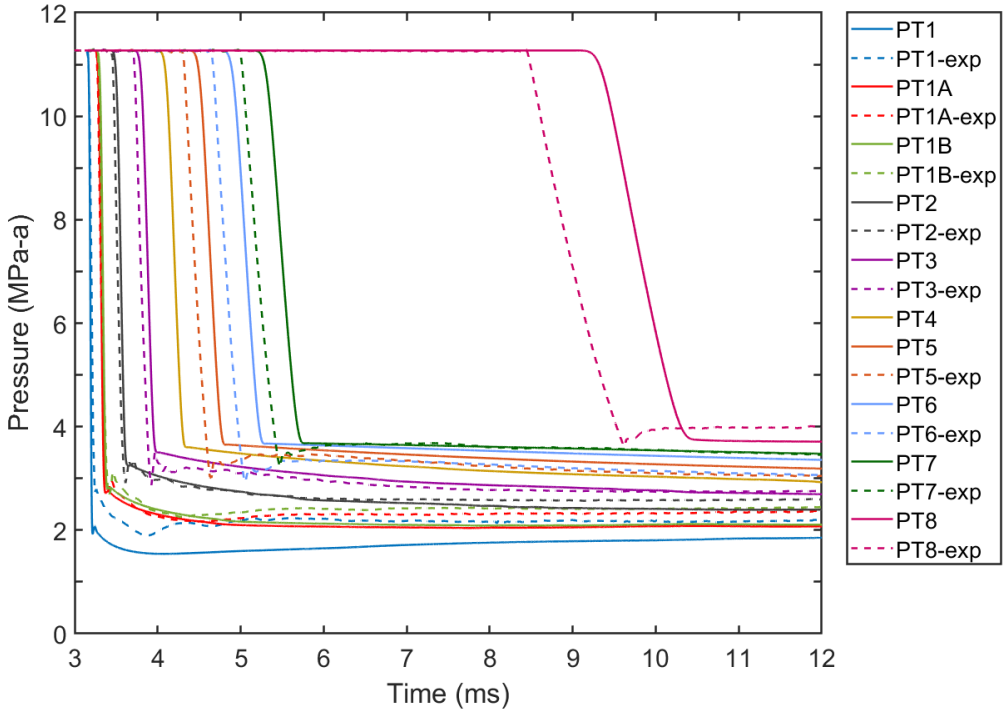

Figure 4-5. Comparison of predicted and experimental pressure-time curves, 12 ms, C = 8 s^{-1}.

It is worth noting that Botros et *al.* (2015) [15] did not report experimental results for PT4 location. In addition, the uncertainty of the pressure transducers used in the shock tube test corresponds to ± 0.04 MPa. Furthermore, as data acquisition started before the rupture of the burst disk at the front end of the shock tube, experimental time-zero represents a state prior to the discharge. In contrast, the CFD model takes time-zero as the rupture. When comparing the predicted and experimental pressure-time traces, 3.1 ms were added to the model's time scale to match the experimental decrease in pressure at PT1 location (reference point). Therefore, the time scale of Figure 4-1 through Figure 4-5 corresponds to experimental values. In case of comparing the pressure-time traces with

figures in following sections, 3.1 ms must be subtracted from the time reported in the pressure-time profile to obtain the model time scale, which is used in the rest of the analysis.

4.2.2. Pressure-temperature trajectories

Figure 4-6 shows the CFD calculated pressure-temperature curves at PT1, PT1A, PT1B, PT2 and PT3 during the first 10.5 ms of the depressurization, using C = 8 s^{-1}. It should be noted that no experimental results for the temperature were reported by Botros *et al.* (2015) [15]. Therefore, a comparison with P-T measured data is not possible.

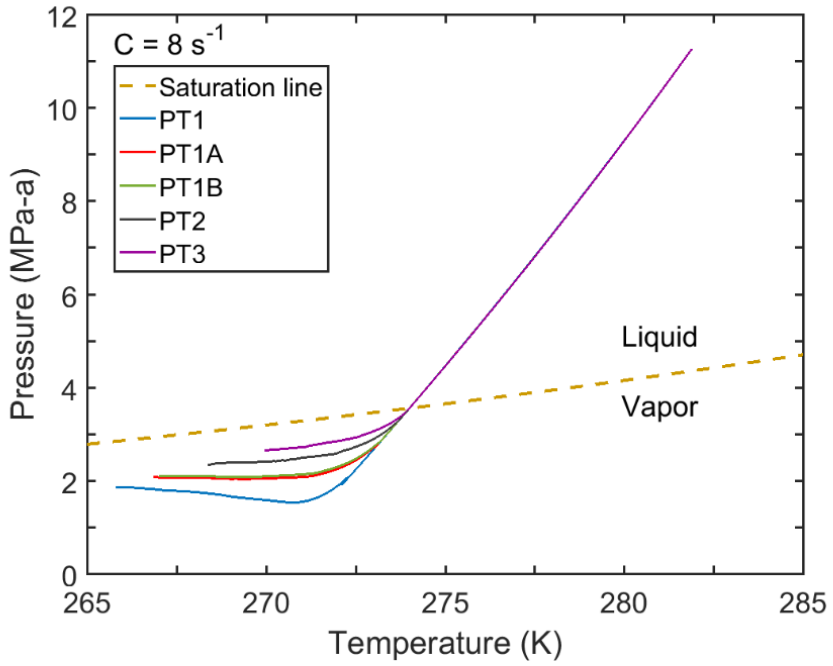

Figure 4-6. Pressure-temperature curves at various locations, 10.5 ms, C = 8 s^{-1}.

The initial conditions in the pipeline are 11.27 MPa-a and 281.89 K, which correspond to carbon dioxide in the liquid phase. The pressure-temperature trajectories from the initial conditions to the saturation line are identical for different locations of

pressure transducers. During this initial stage of the decompression, phase transition does not occur in the system.

After equilibrium saturation conditions are reached (yellow line), the CFD model calculations show differences in temperature at a given pressure for the various locations of the pressure transducers. For locations closer to the pipeline open-end (*e.g.*, PT1, PT1A and PT1B), the model predicts a larger maximum deviation from the saturation line in comparison to the deviations at farther transducers. This deviation is related to non-equilibrium vapor generation, which means that the liquid fails to begin evaporation when reaching the equilibrium saturation conditions [77]. The non-equilibrium phase transition leads to metastable liquid conditions (*i.e.*, superheated liquid) during the expansion.

Cosham *et al.* (2012) [13] showed that during CO_2 depressurization experiments with a shock tube, the pressure where the plateau starts to appear is higher as the distance from the outlet increases, which leads to a 'rising plateau' for pressure transducers located farther from the open-end. The previous behavior is captured by the current CFD model using the test 32A conducted by Botros *et al.* (2015) [15]. The 'rising plateau' results in Figure 4-6 are related to less delayed nucleation with respect to the equilibrium saturation conditions, at locations farther away from the pipeline outlet.

Benintendi (2014) [78] discussed how a rapid CO_2 expansion leads to a strong change of the molecular energy levels of a system (translational, vibrational, rotational), which may result in a non-equilibrium phenomenon. Therefore, closer to the pipeline outlet, a stronger modification of the molecular energy levels may occur given the faster

change in fluid properties, resulting in a stronger deviation from equilibrium saturation conditions when compared to locations farther from the exit plane.

An alternative explanation for the ‘rising plateau’ may be related to a more abrupt decrease in pressure at locations closer to the pipeline outlet due to their proximity to the surroundings, where atmospheric conditions predominate. In contrast, farther into the pipeline, the shock tends to be less severe since those locations are not in the vicinity of ambient conditions.

The concept of relaxation is discussed by Benintendi (2014) [78]. Relaxation refers to the recovery of the equilibrium after a previous equilibrium state is modified. Thus, relaxation is intrinsically related to non-equilibrium phase transition (*e.g.*, delayed bubble formation) and metastability. Although Figure 4-6 describes that various locations along the pipeline report different deviation from the equilibrium saturation line, Figure 4-6 also suggests a trend towards the recovery of equilibrium over time, as the curves approach the saturation conditions.

The mass transfer coefficient (C) included in the source terms representing the phase transition has an effect on the pressure-temperature curves predicted by the CFD model. Figure 4-7 shows the pressure-temperature trajectories predicted at PT1 location during the first 10.5 ms of the expansion, using C = 8 s^{-1}, C = 25 s^{-1}, C = 100 s^{-1} and C = 1000 s^{-1}.

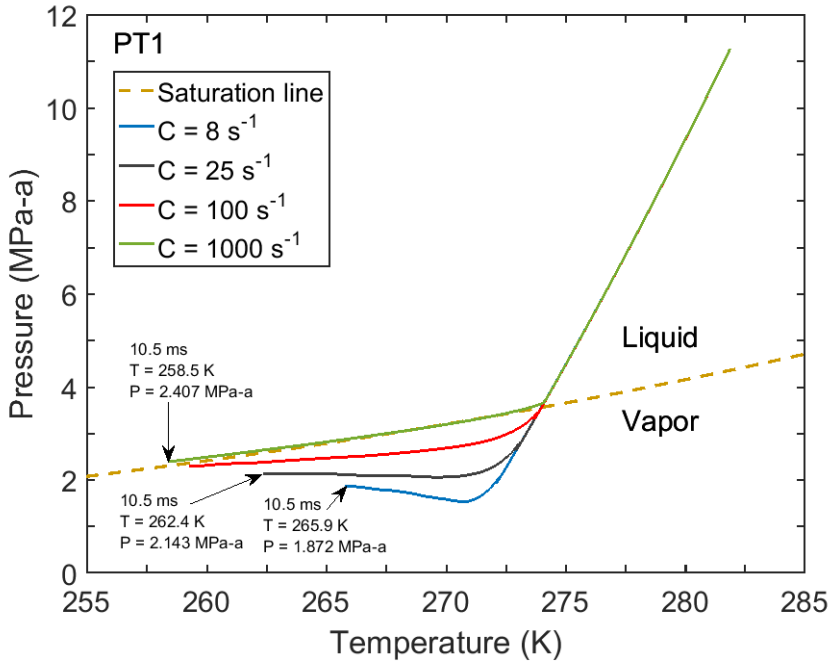

Figure 4-7. Pressure-temperature curves at PT1, 10.5 ms, C = 8, 25, 100, 1000 s^{-1}.

For different C values, the pressure-temperature trajectories from the initial conditions (11.27 MPa-a, 281.89 K) to the saturation line are identical. Therefore, the mass transfer coefficient does not have a significant impact on the trajectory before reaching the saturation. However, after crossing the equilibrium saturation conditions, the model prediction starts to show different behavior for the various values of C. A smaller mass transfer coefficient predicts a larger deviation from the saturation line, this deviation represents the non-equilibrium evaporation process. A more prominent delayed nucleation (with respect to the saturation conditions) occurs as the C value decreases.

On the contrary, for C = 1000 s^{-1} (green curve in Figure 4-7), the model prediction overlaps the saturation line. Thus, equilibrium vapor generation is obtained when the mass transfer coefficient is as large as 1000 s^{-1}. Nevertheless, when comparing the predicted

and experimental pressure-time curves (Figure 4-1 to Figure 4-4), it is observed that C = 1000 s^{-1} generates a significant over-prediction of the pressure plateau, while using a smaller coefficient (*e.g.*, C = 8 s^{-1}) leads to better agreement with the experiment.

Because a mass transfer coefficient significantly smaller than 1000 s^{-1} generates a model prediction that agrees better with the observed delayed nucleation, incorporating the non-equilibrium assumption while modeling a rapid carbon dioxide decompression is deemed to be important.

Despite diverse C values leading to different deviations from the equilibrium saturation line, a trend towards the recovery of equilibrium is observed as the curves representing various mass transfer coefficients approach the saturation line over time. In addition, the last portion of the pressure-temperature curves show that a higher C value leads to a lower temperature at 10.5 ms (See text boxes with data at 10.5 ms in Figure 4-7). Appendix E depicts model predictions for the vapor volume fractions after simulating 10.5 ms using different values of the mass transfer coefficient (C) at PT1 and PT1A locations. Since the mass transfer coefficient may be interpreted as an evaporation rate, a higher C value leads to a faster phase transition from liquid to vapor, and as a result, a higher vapor volume fraction is obtained adjacent to the open-end after a specific period of time. Therefore, the system spends more energy in the phase transition process as more vapor is produced, and the temperature decreases more significantly.

In contrast, the last portion of the pressure-temperature curves in Figure 4-7 show that a higher C value leads to a higher pressure at 10.5 ms. Since vapor density tends to be lower than liquid density, a larger production of vapor (higher C value) may result in a

significant decrease in the density of the two-phase mixture close to the pipeline outlet, where the phase transition starts. Therefore, the mass flow rate exiting the system tends to be lower. Less amount of fluid discharging translates into less reduction in pressure when incorporating a higher C value.

4.2.3. Average decompression wave speed

When a pipeline transporting pressurized carbon dioxide ruptures, a decompression wave propagates through the fluid in the opposite direction from the exit plane [13]. The sudden rupture often results in sonic [57] or supersonic flow at the pipeline opening [65]. The velocity of the expansion wave is equal to the local speed of sound of the fluid less the local outflow velocity [12, 13, 65]. The decompression of the fluid occurs behind the front edge of this wave [13].

To analyze the behavior of the decompression wave speed, it is important to understand the factors that have an impact on the speed of sound of the fluid and its outflow velocity [65]. However, the decompression wave speed is primarily governed by the speed of sound [29]. The previous statement may be related to the larger order of magnitude of the speed of sound in comparison to the fluid velocity inside the pipeline, for a system transporting liquefied CO_2. Although there is a sonic or supersonic flow at the outlet, the conditions inside the pipeline correspond to subsonic flow [65].

To study the decompression behavior of a fluid, a shock tube is commonly used. This device is described as a straight pipe of constant cross-sectional area, usually closed at one end, while the opposite side contains a rupture disc that bursts to represent the open-end. Fast response pressure transducers are mounted along the shock tube to measure the

change in fluid pressure and detect the propagation of the expansion wave [13]. It should be noted that shock tube experiments do not provide the local decompression wave speed (local speed of sound minus local outflow velocity) [6, 12]. Instead, an average decompression wave speed is obtained by collecting the times at which specific pressure values are reached at various locations, which usually correspond to the pressure transducers' locations. Then, the slope of the 'location vs. time' plot is calculated for each isobar. This slope represents the decompression wave speed related to such pressure level [6, 15]. To obtain the 'pressure vs. average decompression wave speed' plot, the previous process is repeated for the complete pressure range. This method can be performed using the experimental results or the predictions of the decompression model.

Figure 4-8 depicts an example of a linear regression to obtain the average decompression wave speed at 10 MPa-a, using the model prediction at locations corresponding to the four closest pressure transducers to the open-end (PT1, PT1A, PT1B and PT2). The average decompression wave speed predicted by the CFD model corresponds to 497.29 m/s (slope). The mass transfer coefficient in the previous example is $C = 8\ s^{-1}$.

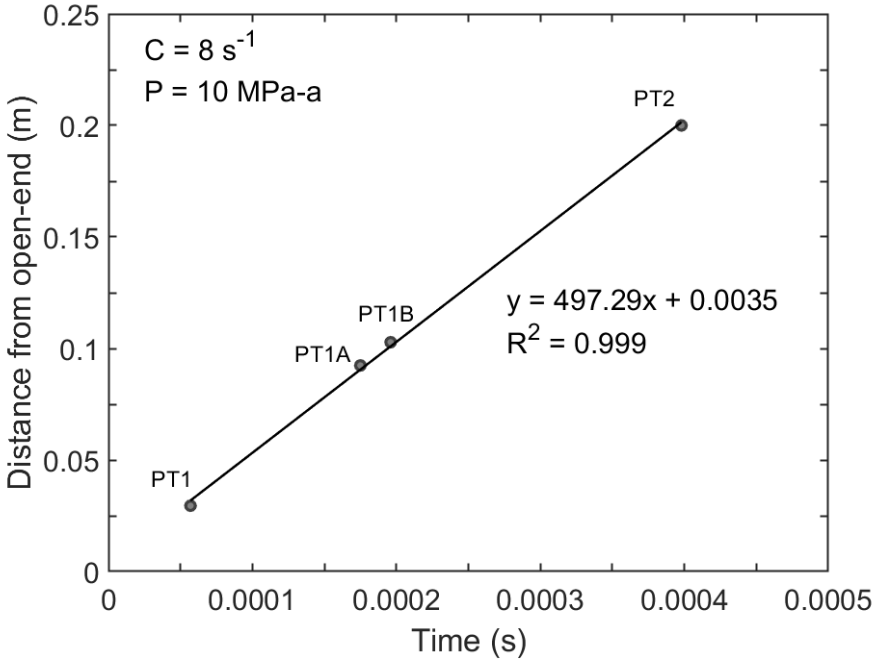

Figure 4-8. Example of linear regression to obtain average decompression wave speed at specific pressure.

While calculating the average decompression wave speed predicted by the model, it is observed that results depend on the number of pressure transducers' locations included in the linear regressions. Figure 4-9 illustrates the average decompression wave speed calculated using 3, 4 and 5 pressure transducers' locations closest to the open-end. In addition, the average decompression wave speed reported by Botros *et al.* (2015) [15] for the shock tube test 32A is used to validate the model results.

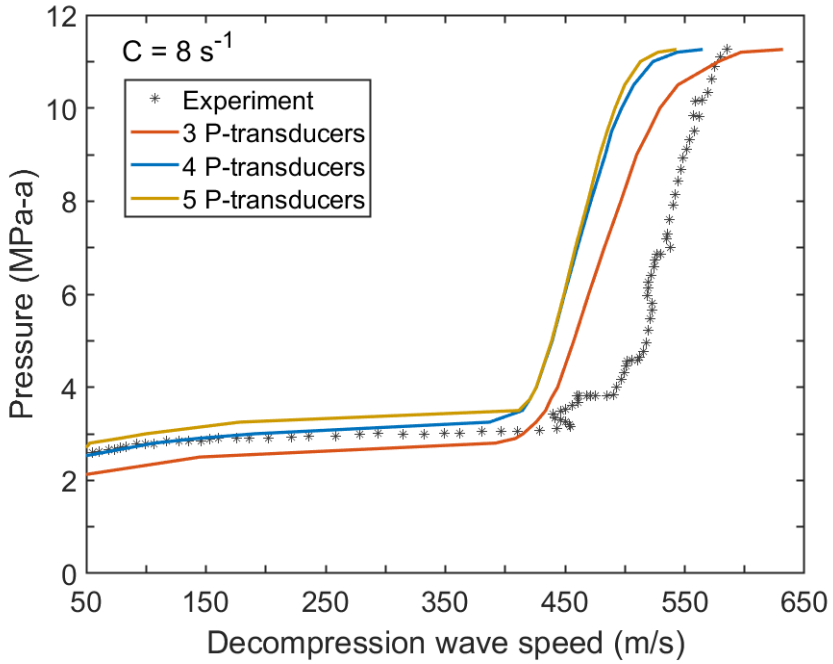

Figure 4-9. Average decompression wave speed prediction with different number of pressure transducers, C = 8 s^{-1}.

Figure 4-9 shows that as the number of pressure transducers increases, which means that the linear regressions included more locations farther from the pipeline outlet, the initial average decompression wave speed decreases, while the pressure corresponding to the horizontal plateau becomes higher. An explanation for the lower initial decompression wave speed may be related to the fact that the expansion wave takes more time to arrive at pressure transducers that are farther from the open-end. Therefore, the slope of the 'location vs. time' plot will be less, and this will translate into a lower decompression wave speed when including locations that are more distant from the pipeline exit.

Furthermore, literature suggests that the results of the average decompression wave speed depend on the locations used to calculate the slopes of the isobars. Botros *et al.* (2004) [65] observed that when using pressure transducers closer to the open-end, the calculated decompression wave speed tends to be higher than that calculated using transducers farther from the outlet. The previous behavior may be due to frictional effects while the expansion wave travels in the opposite direction from the exit plane.

In addition, the reason for the higher pressure plateau with the increment on the number of pressure transducers may be related to the 'rising plateau' phenomenon reported by Cosham *et al.* (2012) [13]. As the distance from the outlet increases, the pressure where the plateau starts to appear tends to be higher in the pressure-time curves (See Figure 4-1). This occurs due to less deviation with respect to the equilibrium saturation conditions, at locations further away from the pipeline outlet. Hence, when calculating the decompression wave speed, the 'average plateau' in Figure 4-9 tends to be higher when incorporating farther pressure transducers' locations.

The pressure plateau of the decompression wave speed curve is a major feature in fracture propagation control of pipelines transporting fluids that undergo a two-phase decompression [79]. To accurately predict the toughness adequate to arrest a propagating fracture, the determination of the pressure plateau is crucial [6]. In the case of Figure 4-9, the best prediction of the plateau corresponds to the curve using the four closest pressure transducers to the outlet. Therefore, this work calculates the average decompression wave speed using the locations corresponding to PT1, PT1A, PT1B and PT2.

Figure 4-10 illustrates the comparison between the experimental average decompression wave speed and the predicted curves using different values for the mass transfer coefficient C. The shape of both types of curves (predicted and experimental) corresponds to an initial fast pressure drop followed by a stable period where the pressure plateau appears. Although the shapes of the profiles are similar, the CFD model underpredicts the initial decompression wave speed in comparison to the experimental results. Independent of the C value, the model using the Peng-Robinson EoS predicts an initial average decompression wave speed of 565 m/s. In contrast, the initial expansion wave speed related to the shock tube test is 585 m/s.

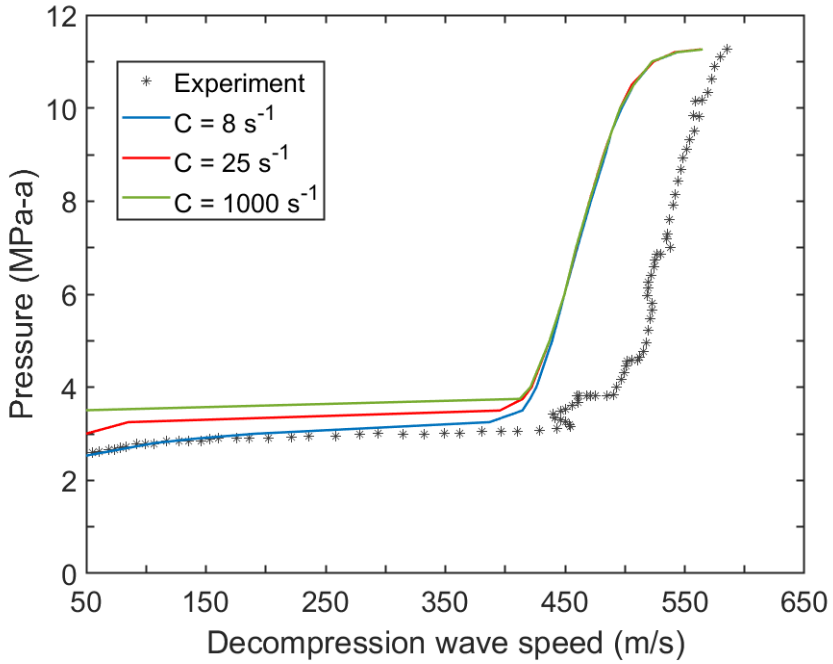

Figure 4-10. Comparison of predicted and experimental average decompression wave speed.

In addition, the model significantly underpredicts the decompression wave speed in the region corresponding to the fast pressure drop. From 11 MPa-a to 4 MPa-a, the decompression wave speed calculated with the CFD results is on average 13% lower than the experimental data. Besides, this region shows that for a specific value of decompression wave speed, the predicted pressure is higher than the experimental pressure, indicating that a slower depressurization is simulated with the CFD model. As a result, there is a delay between calculated and measured pressure-time traces, as reported in Figure 4-5. Since the decompression wave speed is primarily governed by the speed of sound of the fluid [29], the Peng-Robinson EoS may be underpredicting the sound speed of the liquid, which is the only phase during the initial stage of the expansion. The underprediction of the liquid speed of sound with the Peng-Robinson EoS is discussed in Section 3.4.2.1.

In Figure 4-10, it is worth noting that different values of C generate the same model prediction for the decompression wave speed in the region corresponding to the fast pressure drop (11 MPa-a to 4 MPa-a). Since phase transition has not started in this section of the curves (pressure above the saturation conditions), different values of the interphase mass transfer coefficient representing the evaporation rate do not affect the model prediction.

Similar to the plateau in the pressure-time curves, the plateau in Figure 4-10 represents the phase transition. A lower C leads to a plateau at lower pressure as the system deviates more from the equilibrium saturation conditions. The previous statement is justified based on the pressure-temperature curves for different C values, which were

previously discussed. The best agreement between the model and the experimental plateau in Figure 4-10 is obtained when C = 8 s^{-1}. Despite the difference between predicted and measured decompression wave speed in the fast pressure drop region while using the Peng-Robinson EoS, the model is capable of accurately predicting the pressure plateau due to the incorporation of non-equilibrium phase transition.

The importance of studying the decompression wave speed is related to a safety concern called running ductile fracture. When an initial fracture occurs, the high pressure in the pipeline may lead to its fast growth along the fracture line. Therefore, fracture propagation control focuses on designing a pipeline that avoids this growth [29]. To determine the toughness that would arrest a propagating fracture, the prediction of the decompression behavior of the fluid is needed [13].

Literature suggests that the Battelle Two-Curve Model (BTCM) is generally used to estimate the appropriate pipeline toughness to arrest a running ductile fracture. The previous method compares the decompression wave speed with the fracture propagation speed for different toughness values. These curves are contrasted in a 'pressure vs. speed' plot. The toughness associated with the fracture speed tangent to the decompression wave speed represents the minimum toughness needed for fracture arrest [6].

4.2.4. Local decompression wave speed

Although shock tube experiments provide an average decompression wave speed using a specific number of pressure transducers' locations, the CFD model can predict the local decompression wave speed at any location along the pipeline. This local expansion

wave speed is defined as the local speed of sound of the fluid minus the local outflow velocity [6, 12, 16]:

$$W_{local} = c - u \quad \textbf{(4-1)}$$

Because the local and average decompression wave speeds are calculated using different methods, their comparison should be carefully conducted.

Figure 4-11 illustrates the model prediction for the local decompression wave speed and the speed of sound of the fluid at 0.2 m from the pipeline outlet (PT2 location). In addition, this plot shows the average decompression wave speed reported by Botros *et al.* (2015) [15] for the shock tube test 32A. It is observed that the local decompression wave speed at PT2 and the average expansion wave speed calculated with the experimental results have the same shape, which corresponds to an initial fast pressure drop followed by a stable period where a pressure plateau appears. However, since the behavior of the local decompression wave speed varies with position (specifically the pressure plateau region of the curve), a point-by-point comparison with the average decompression speed is not suitable.

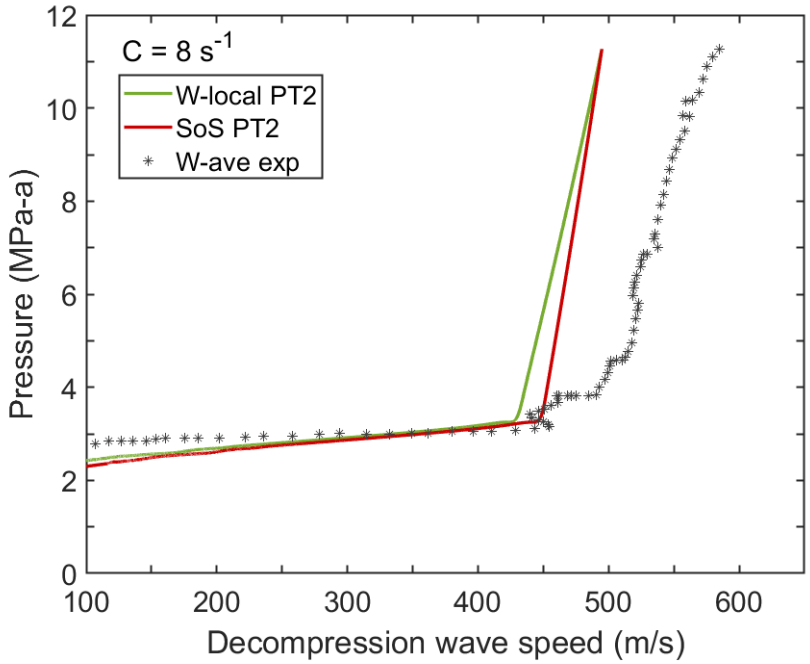

Figure 4-11. Comparison between decompression wave speed and speed of sound.

When the local decompression wave speed at PT2 is contrasted with the speed of sound of the fluid at the same location, it is observed that initially (time zero), both of them are equal. The reason for this behavior is the zero outflow velocity before the rupture. Furthermore, Figure 4-11 depicts that the cause of the pressure plateau in the decompression wave speed curve is related to the discontinuity of the speed of sound occurring with the phase transition. A sharp drop in the speed of sound happens when the liquid crosses the phase boundary. In general, the local decompression wave speed and the speed of sound at the same location show a very similar behavior along the expansion process.

Figure 4-12 shows the pressure vs. velocity curve at PT2 location. As the expansion progresses, the pressure decreases drastically while the velocity magnitude

increases. A pressure plateau associated with the phase transition is also depicted in this figure. Compared to the order of magnitude of the speed of sound in Figure 4-11, the outflow velocity at PT2 location is significantly lower. This fact emphasizes that the decompression wave speed is predominantly governed by the speed of sound of the fluid.

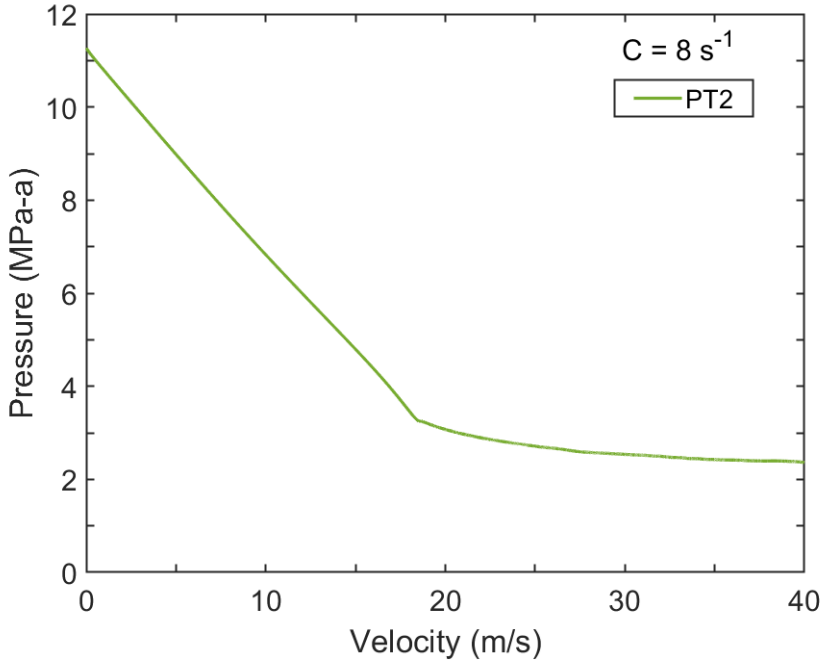

Figure 4-12. Pressure vs. velocity at PT2 location.

Although the average and local decompression wave speeds should not be compared point-by-point, the general trend of the curves can be analyzed in Figure 4-11. A significant difference between the local decompression wave speed at PT2 and the experimental average speed is observed in the region corresponding to the fast pressure drop, from 11 MPa-a to 4 MPa-a. Since the decompression wave speed is mainly driven by the speed of sound of the fluid, this noticeable discrepancy is related to the underprediction of the speed of sound of the liquid phase when implementing the Peng-

Robinson EoS. It should be noted that in the region of rapid pressure drop, liquid CO_2 is the only phase since saturation conditions have not been reached.

The underprediction of the liquid and metastable liquid speed of sound by the Peng-Robinson EoS leads to lower values of decompression wave speed, and therefore a delay in the wave front arrival at the pressure transducers' locations is expected. Farther from the exit plane, a stronger delay occurs. As a result, discrepancies between predicted and measured pressure-time traces in the region of fast pressure drop (Figure 4-1 to Figure 4-4) are caused by a delay in the arrival of the decompression wave, which is a consequence of the predictive limitations when incorporating the Peng-Robinson EoS in the CFD model.

4.3. Conclusions

In this work, the effect of the mass transfer coefficient (C) on the CFD decompression model was studied. Some of the most important findings are as follows:

- The mass transfer coefficient proves to have a predominant impact on the pressure plateau representing the phase transition. A smaller value of C translates into a more pronounced deviation with respect to the saturation conditions, and thus a plateau at lower pressure is expected.
- The prediction of the CFD decompression model overlaps the saturation line when C is as high as 1000 s^{-1}. However, a mass transfer coefficient C = 8 s^{-1} generates a model prediction that agrees better with the experiment. Therefore, incorporating the non-equilibrium assumption while modeling a rapid carbon dioxide decompression is deemed to be important.

- The mass transfer coefficient does not seem to have a significant effect on the arrival of the decompression wave front at different pressure transducers' locations. Since C may represent the evaporation rate, its value would not have an effect before the phase transition starts, which is related to the fast pressure drop region of the curves (P-time, P-T, P-decompression wave speed) before reaching the saturation conditions.

In addition to the effect of the mass transfer coefficient on the model predictions, Section 4 shows that the CFD model implementing the Peng-Robinson EoS (for the liquid phase properties) significantly underpredicts the decompression wave speed, which leads to a delay in the arrival time of the expansion wave front at the pressure transducers' locations. This may be related to the underprediction of the liquid-phase speed of sound by the Peng-Robinson EoS. Therefore, it is important to incorporate a more accurate approach to calculate thermodynamic properties of the liquid, which is the primary phase in early stages of the depressurization.

5. CFD DECOMPRESSION MODEL IMPLEMENTING CORRELATIONS BASED ON SPAN-WAGNER EOS

5.1. Thermodynamic approach

In this section, the results corresponding to the CFD model that implements a set of thermodynamic and transport properties through independent UDFs for the vapor phase, and a UDRGM that includes correlations based on the Span-Wagner EoS for the liquid are discussed.

5.2. Model results

5.2.1. Model validation: pressure-time traces

The validation of the CFD model is conducted using test 32A from Botros *et al.* (2015) [15]. The initial conditions in the shock tube test correspond to pressurized liquefied CO_2 at 11.27 MPa-a and 281.89 K. This pure CO_2 test is also used in the validation of the CFD model incorporating the Peng-Robinson EoS to predict liquid properties.

Figure 5-1 to Figure 5-4 show the comparison between model predictions (solid lines) and experimental results (dotted lines) for the pressure-time profiles out to 5 ms. The multiphase CFD model included four different values for the mass transfer coefficient, C = 7 s^{-1}, 25 s^{-1}, 100 s^{-1} and 1000 s^{-1}. This comparison incorporates the experimental measurements at five pressure transducers near the exit plane (PT1: 0.0295 m, PT1A: 0.0924 m, PT1B: 0.1028 m, PT2: 0.2 m and PT3: 0.35 m from the open-end). The complete list of pressure transducers' locations is reported in Table 4-1.

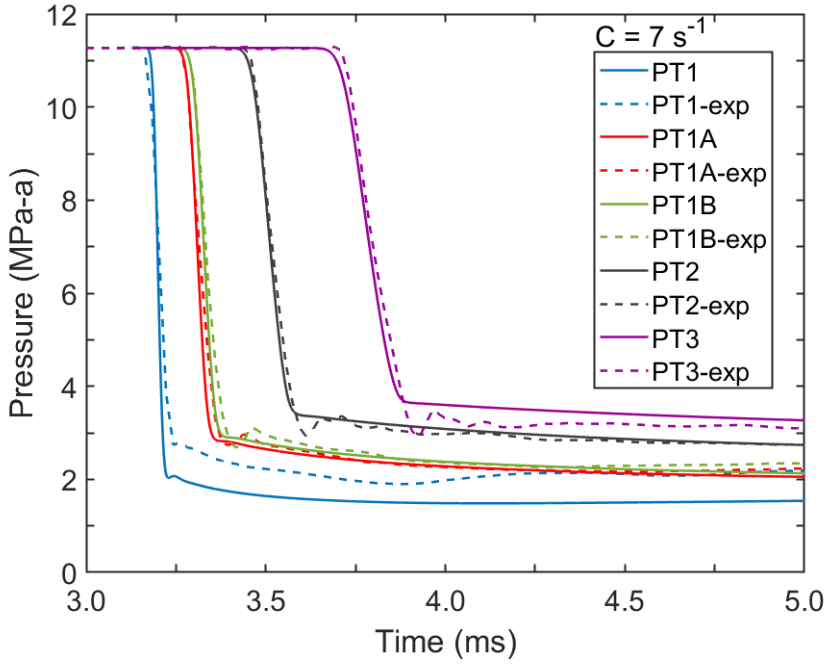

Figure 5-1. Comparison of predicted and experimental pressure-time curves at different positions, C = 7 s^{-1}.

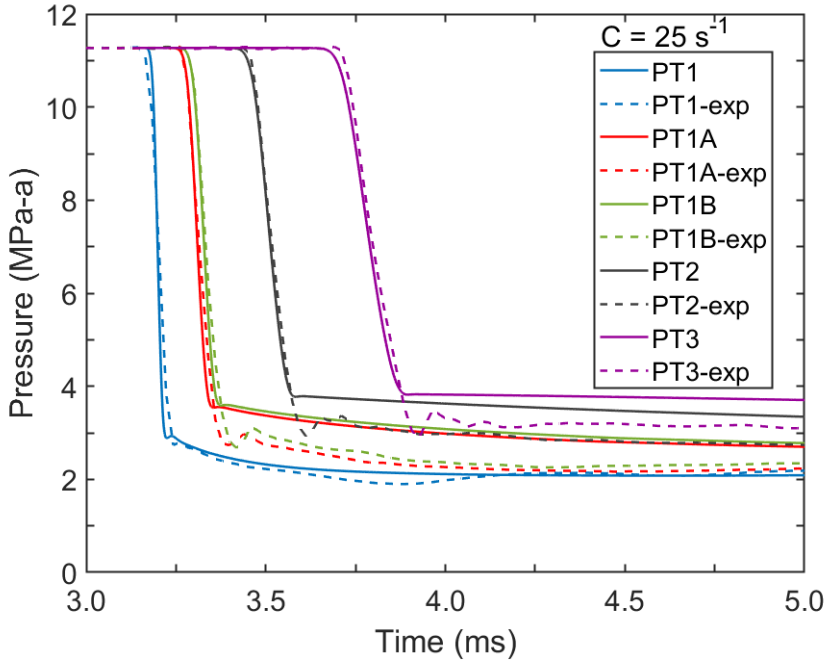

Figure 5-2. Comparison of predicted and experimental pressure-time curves at different positions, C = 25 s^{-1}.

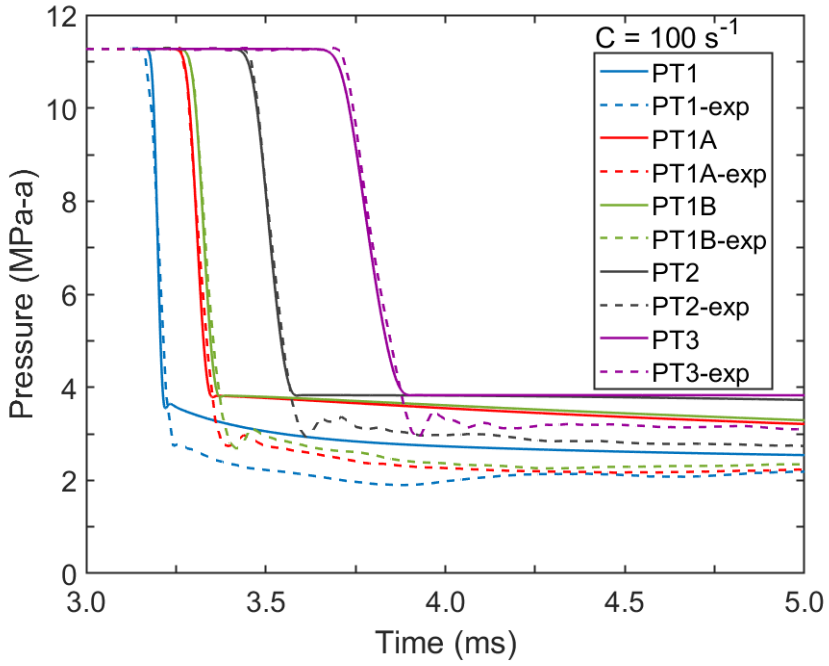

Figure 5-3. Comparison of predicted and experimental pressure-time curves at different positions, C = 100 s^{-1}.

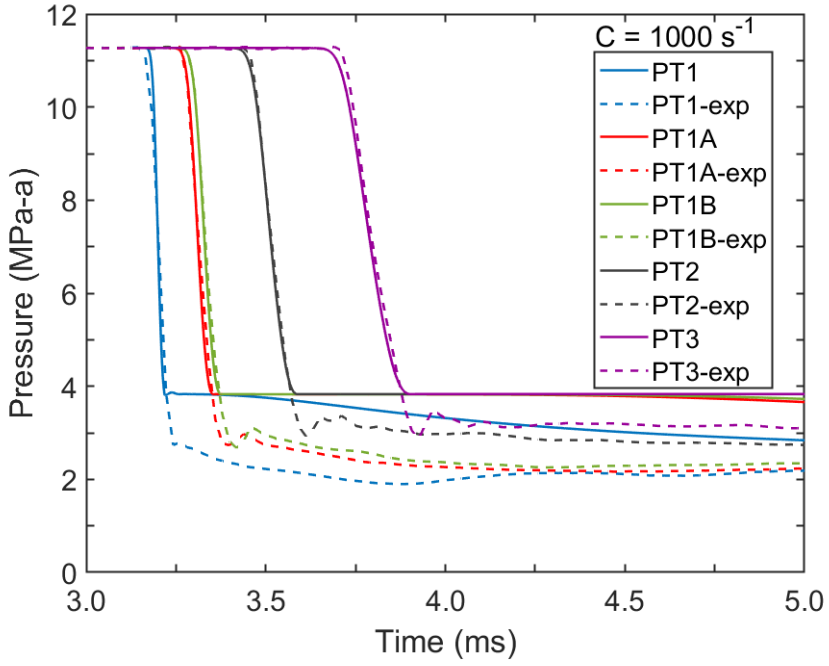

Figure 5-4. Comparison of predicted and experimental pressure-time curves at different positions, C = 1000 s^{-1}.

In terms of Figure 5-1 to Figure 5-4, each pressure-time curve is composed of three regions. Firstly, the region before the wave front arrival, where the initial pressure has not started to decrease, leading to a flat behavior. Secondly, the rapid pressure drop caused by the arrival of the decompression wave at the pressure transducer's location. And lastly, the formation of the pressure plateau, which indicates the beginning of the phase transition at that specific location.

Comparing the pressure-time traces predicted by the CFD model using correlations based on Span-Wagner EoS (Figure 5-1 to Figure 5-4) with the results implementing the Peng-Robinson EoS (Figure 4-1 to Figure 4-4), the main difference is on the region where the rapid pressure drop occurs, after the arrival of the decompression wave front. The model using PR EoS shows a significant delay with respect to the experimental results. When implementing the latter thermodynamic approach, the time taken by the wave front to arrive at each pressure transducer location is greater than the test results. This discrepancy increases for locations farther from the open-end. In contrast, the CFD model using SW correlations successfully predicts the region of fast pressure drop, and hence it does not show a delay in the wave front arrival.

Similar to the pressure-time traces obtained with PR, the predictions using correlations based on SW show that the time taken by the wave front to arrive at each pressure transducer location does not vary significantly for different values of the mass transfer coefficient (C). Since 'C' represents the nucleation rate in the mass and energy source terms for the vaporization process, its value should not have a significant impact before the phase transition starts. Therefore, 'C' may not have an important effect on the

arrival time of the decompression wave at the pressure transducers' locations. On the contrary, since the decompression wave speed is mainly driven by the speed of sound of the fluid, the accuracy of the prediction of this thermodynamic property has a direct effect on the wave front arrival. The improvement in the prediction of the liquid speed of sound when implementing SW correlations enhances the prediction of the arrival time of the decompression wave, and thus the rapid expansion region in the pressure-time curves matches the experimental results. In comparison to PR EoS, the speed of sound correlation based on SW EoS predicts higher values for the speed of sound of the liquid, improving the prediction of the CFD model.

The third region of the pressure-time traces in Figure 5-1 to Figure 5-4 is the pressure plateau region. It is observed that for the same value of mass transfer coefficient 'C', there are no significant differences between the prediction of the pressure plateau using SW correlations or PR EoS, when comparing the results at a specific pressure transducer location. Furthermore, the significant effect of the mass transfer coefficient on the pressure plateaus obtained with the PR EoS is also observed when implementing SW correlations. A higher C generates a pressure plateau at higher pressure, corresponding to a faster phase transition from liquid to vapor.

During the first 5 ms, the pressure-time traces predicted with the CFD model incorporating SW correlations show that the mass transfer coefficient that better predicts the pressure plateau at locations PT1A, PT1B, PT2 and PT3 corresponds to $C = 7\ s^{-1}$. In addition, the best C value that matches PT1 profile during this time interval is $C = 25\ s^{-1}$.

Figure 5-5 illustrates the pressure-time traces during 15 ms while implementing a mass transfer coefficient C = 7 s^{-1} in the CFD model that incorporates SW correlations. After 15 ms, the wave front has passed beyond PT9 location (5.1 m from open-end). In general, the model successfully predicts the region of rapid pressure drop in the curves. However, a slight difference between the model prediction and the experimental results is observed at PT8 and PT9 locations. The predicted wave front takes slightly less time to arrive at those two positions. In addition, this difference seems to increases as the pressure transducer is located farther from the outlet (larger difference at PT9 than PT8). This may indicate that the prediction of the decompression wave speed at locations farther from the exit plane is slightly higher than the experimental values. A possible reason for this behavior may be related to less frictional losses predicted by the CFD model.

Additionally, when analyzing the pressure plateaus in Figure 5-5, the model results suggest that the same 'C' value may not be adequate to predict the plateau at different locations. Besides, this coefficient may be time-varying, especially at locations closer to the outlet, as the system tends to return to the equilibrium saturation conditions that were exceeded due to non-equilibrium phase transition. Therefore, the mass transfer coefficient may be location-varying and time-varying when modeling the expansion process.

Lastly, it is worth noting that Figure 5-5 did not include the experimental results at PT4 location since these were not reported by Botros et *al.* (2015) [15]. Moreover, the uncertainty of each pressure transducer used in the shock tube experiment is ± 0.04 MPa.

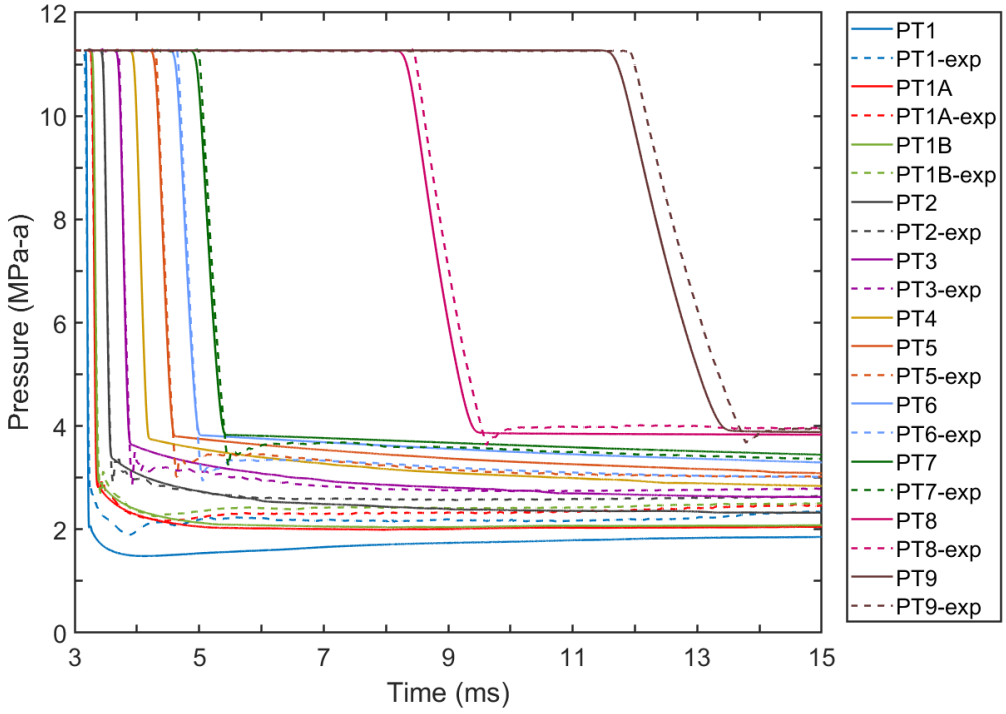

Figure 5-5. Comparison of predicted and experimental pressure-time curves, 15 ms, C = 7 s^{-1}.

5.2.2. Pressure-temperature trajectories

Figure 5-6 depicts the pressure-temperature trajectories predicted at PT1, PT1A, PT1B, PT2 and PT3 during the first 15 ms of the decompression, using C = 7 s^{-1} in the CFD model incorporating SW correlations. A comparison with P-T measured data is not performed since no experimental results for the temperature were reported by Botros *et al.* (2015) [15]. Since the model accuracy improved after including SW correlations (See Figure 5-1), the CFD simulations were conducted for a larger period of time in comparison to the PR model. This is the reason for the difference in time spans between Figure 5-6 (15 ms) and Figure 4-6 (10.5 ms).

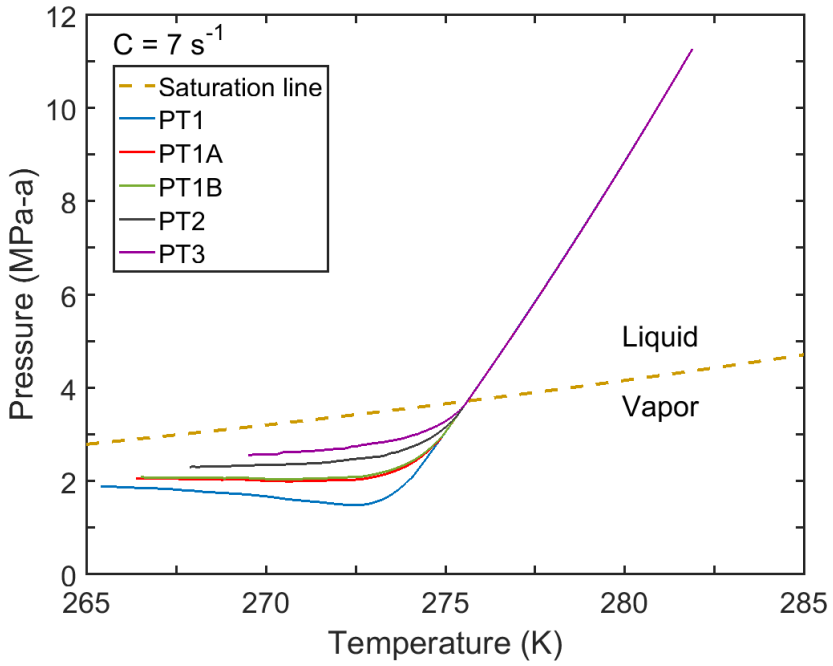

Figure 5-6. Pressure-temperature curves at various locations, 15 ms, C = 7 s^{-1}.

Similar to the pressure-temperature results obtained with PR, the predictions using correlations based on SW show identical thermodynamic trajectories from the initial conditions (11.27 MPa-a, 281.89 K) to the saturation line for different locations of pressure transducers. In addition, the model prediction shows discrepancies between the various locations after crossing the saturation line, obtaining a more pronounced deviation from equilibrium at locations closer to the pipeline outlet. This deviation is related to non-equilibrium phase transition. Therefore, there is a more prominent delayed nucleation with respect to the equilibrium saturation conditions at locations closer to the open-end, where a more abrupt expansion process occurs due to the proximity to the surroundings. This phenomenon is discussed in Section 4.2.2.

Figure 5-6 also shows a trend towards the recovery of equilibrium over time, as trajectories approach the saturation line in the last portion of the curves. During the first 15 ms of the expansion, this trend is more evident when analyzing the results at PT1 location.

In general, the pressure-temperature curves obtained with both thermodynamic approaches, PR EoS and SW correlations, show a similar trend before and after crossing the saturation line, using a constant mass transfer coefficient and varying the locations along the pipeline. However, it should be noted that a slightly different 'C' value is used in Figure 5-6 ($C = 7\ s^{-1}$) and Figure 4-6 ($C = 8\ s^{-1}$), as these numbers provided the best agreement during the model validation stage for each thermodynamic approach. Appendices F and G show the pressure-time curves using the PR EoS and SW correlations for different 'C' values ($C = 7\ s^{-1}$ and $C = 8\ s^{-1}$); these appendices provide insight into the selection of the most appropriate 'C' value for each CFD model.

Since the results implementing the PR EoS showed that the mass transfer coefficient has a significant effect on the pressure-temperature curves, Figure 5-7 illustrates the thermodynamic trajectories predicted at PT1 location during the first 15 ms of the decompression, using $C = 7\ s^{-1}$, $C = 25\ s^{-1}$, $C = 100\ s^{-1}$ and $C = 1000\ s^{-1}$ in the CFD model incorporating correlations based on SW EoS.

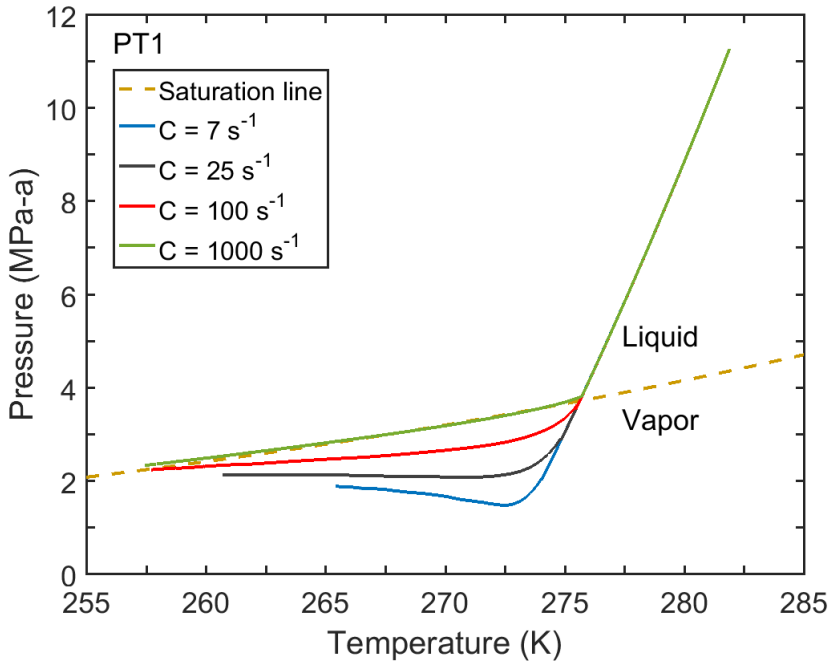

Figure 5-7. Pressure-temperature curves at PT1, 15 ms, C = 7, 25, 100 and 1000 s^{-1}.

As observed with the PR approach, the CFD model incorporating SW correlations shows identical trajectories from the initial conditions to the saturation line, for different values of the mass transfer coefficient. This is related to the fact that 'C' is the nucleation rate in the source terms representing the vaporization process. Therefore, this coefficient should not have an important effect on the P-T curves prior to the start of the phase transition. In contrast, the 'C' value has a significant impact on the trajectories after crossing the equilibrium saturation conditions. A smaller mass transfer coefficient predicts a larger deviation from the saturation line, this deviation represents the non-equilibrium evaporation process. In contrast, equilibrium vapor generation is predicted when C = 1000 s^{-1}. Lastly, a trend towards the recovery of equilibrium is observed as curves representing

mass transfer coefficients different than C = 1000 s^{-1} approach the saturation line over time.

Figure 5-8 illustrates a detailed comparison between the pressure-temperature curves obtained with PR and SW approaches at PT1 location. Since C = 25 s^{-1} predicts the best agreement with the experimental pressure-time profile at PT1 (Figure 5-2), the latter mass transfer coefficient is used in the comparison. When contrasting the P-T curves, it is observed that for the region corresponding to the pressure drop from the initial conditions to the saturation line, the slope of the SW prediction is steeper in comparison to the PR model. Consequently, a quicker expansion is obtained when implementing SW correlations. Evidence of this is provided by the comparison of the number of time steps to reach certain pressure in each approach. For example, when C = 25 s^{-1}, the CFD model incorporating SW takes 54 time steps to reach 8.5 MPa-a; on the other hand, when using PR, the CFD model spends 64 time steps to reach the same pressure at PT1 location. The previous comparison refers to the green boxes in Figure 5-8. Another example is highlighted in the purple boxes, the CFD model using SW crosses the saturation line at higher pressure and temperature than the model including PR EoS. The former spends 71 time steps to reach the equilibrium saturation conditions, while the latter takes 83 time steps to reach this state. It is worth noting that the number of time steps is obtained from the text files corresponding to the pressure monitor point at PT1 location, which represent some of the outputs of the CFD models in ANSYS Fluent.

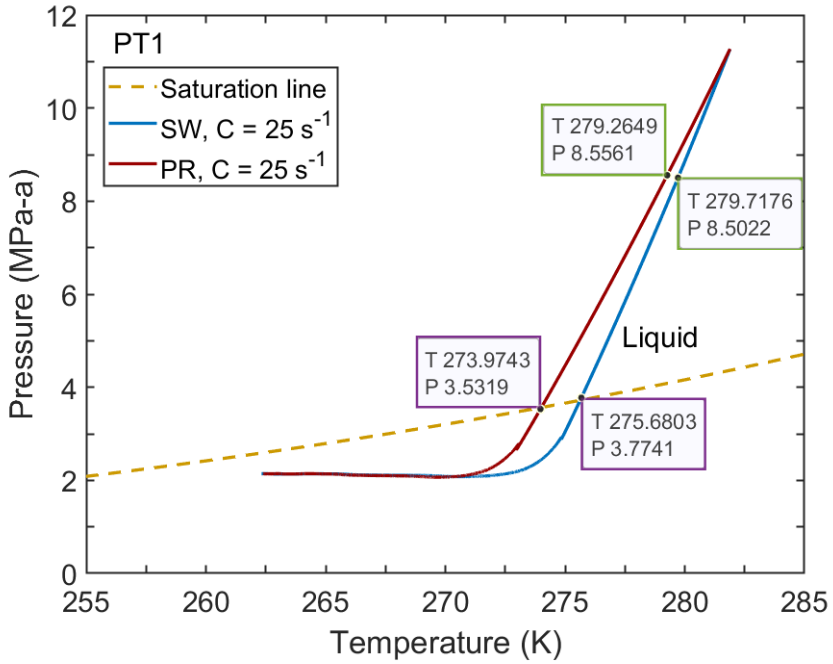

Figure 5-8. SW vs. PR: Pressure-temperature curves at PT1, 10.5 ms, C = 25 s^{-1}.

Although the pressure-temperature curves for both approaches show some differences in the initial phase of the expansion, the two CFD models lead to the same pressure plateau at PT1 location when using C = 25 s^{-1}. Therefore, similar to the pressure-time traces, the P-T trajectories emphasize that the pressure plateau is mainly driven by the value of the mass transfer coefficient in the vaporization source terms.

5.2.3. Average decompression wave speed

As discussed in Section 4.2.3, a shock tube test provides the average decompression wave speed through the calculation of the slopes for the 'location vs. time' plots at multiple isobars. The same method can be implemented using the predictions of the CFD model.

As an example of how to calculate the average decompression wave speed, Figure 5-9 illustrates the linear regression corresponding to 10 MPa-a, using the model predictions at the four closest pressure transducers to the outlet (PT1, PT1A, PT1B and PT2). The average decompression wave speed for this isobar corresponds to 592.84 m/s (slope), using the mass transfer coefficient C = 7 s^{-1} while implementing the CFD model with the SW thermodynamic approach.

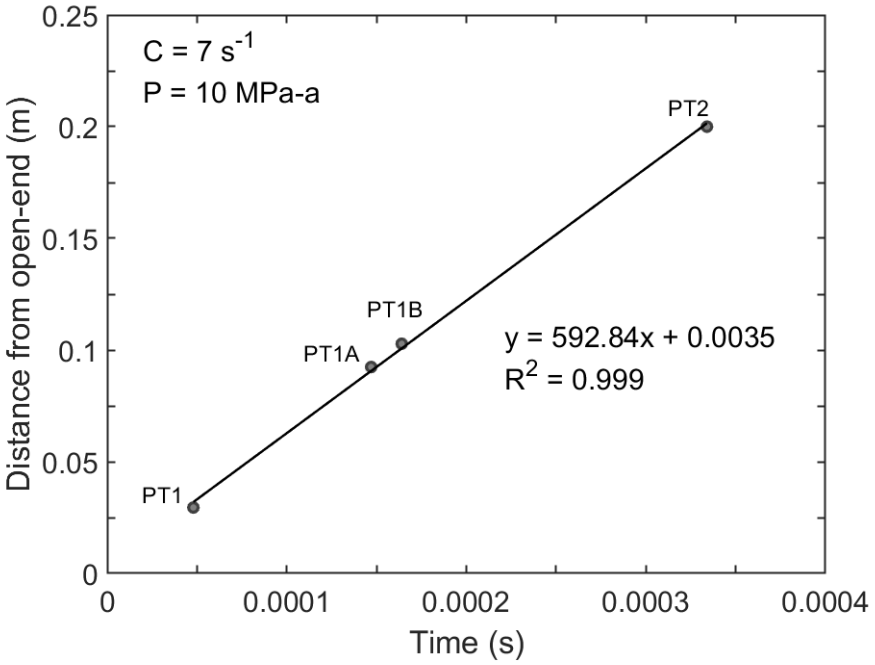

Figure 5-9. Example of linear regression to obtain average decompression wave speed at specific pressure.

Literature suggests that the results of the average decompression wave speed calculated with the slopes method depend on the number of pressure transducers' locations included in the linear regressions [65]. Figure 5-10 shows the pressure vs. average decompression wave speed curves calculated using 3, 4 and 5 pressure transducers'

locations closest to the open-end. For validation purposes, the average decompression wave speed reported by Botros *et al.* (2015) [15] for the shock tube test 32A is included in the comparison.

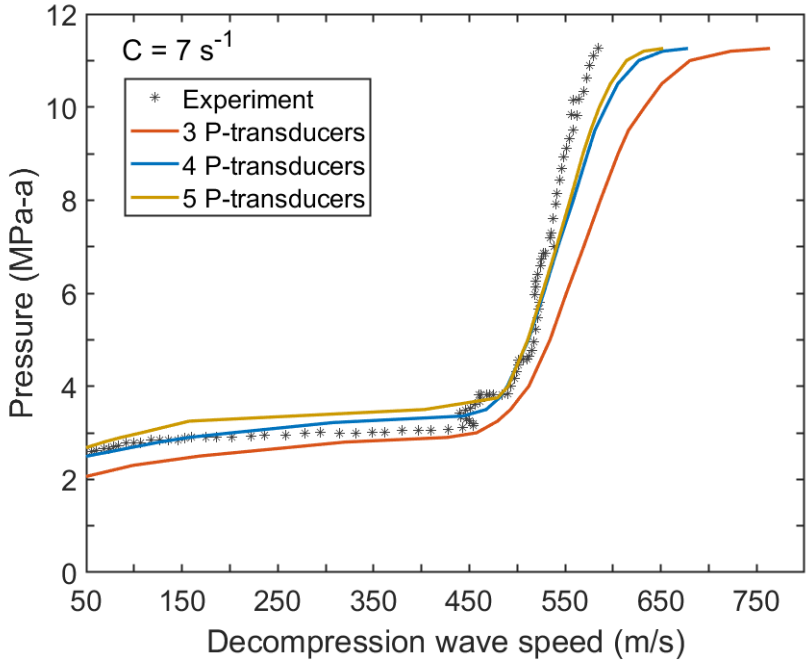

Figure 5-10. Average decompression wave speed prediction with different number of pressure transducers, C = 7 s^{-1}.

As the number of pressure transducers increases, more locations farther from the pipeline exit are included in the linear regressions, resulting in two different effects on the prediction of the average decompression wave speed in Figure 5-10. Firstly, a lower initial decompression wave speed is obtained since the expansion wave takes more time to arrive at pressure transducers farther from the open-end. Therefore, the slope of the 'location vs. time' plot will be less steep, predicting a lower value for the average speed of the expansion wave. Secondly, the pressure corresponding to the horizontal plateau becomes

higher. This is related to the 'rising plateau' phenomenon as less delayed nucleation with respect to the equilibrium saturation conditions occurs at locations further from the pipeline outlet. This translates into a higher plateau in the pressure-time profile at those locations (See Figure 5-1). Consequently, when increasing the number of pressure transducers incorporating locations that are more distant from the open-end, the 'average plateau' in the decompression wave speed curve tends to be higher.

Figure 5-10 depicts an underprediction of the plateau and a significant overprediction of the initial pressure drop region when including three pressure transducers' locations in the calculation of the average decompression wave speed. In contrast, an overprediction of the plateau is obtained when implementing the slope method with five locations. Lastly, the CFD model incorporating SW successfully predicts the plateau when implementing four locations. Since the prediction of the pressure plateau is crucial for decompression modeling, this work includes four pressure transducers' locations (PT1, PT1A, PT1B and PT2) for calculating the average decompression wave speed in Figure 5-11. It should be noted that the same number of pressure transducers is used in the average decompression wave speed study for the PR approach.

Figure 5-11 shows the comparison between the experimental average decompression wave speed and the predicted curves using different values for the mass transfer coefficient in the CFD model incorporating the SW approach. Similar to the pressure-time traces, the predicted and experimental curves in Figure 5-11 show an initial fast pressure drop followed by a pressure plateau. In comparison to the experimental results, the CFD model overpredicts the initial decompression wave speed. Independent

of the C value, an initial speed of 678 m/s is predicted by the model at 11.26 MPa-a. In contrast, the shock tube experiment reported an initial expansion wave speed of 585 m/s for this pressure. Despite the significant overprediction of one data point, there is a successful performance of the model when predicting the average decompression wave speed using C = 7 s^{-1}, especially for the period where the speed is lower than 540 m/s. In the region where the speed is higher than the latter value, the experimental pressure is higher than the predicted pressure, indicating that a faster depressurization is simulated by the CFD model.

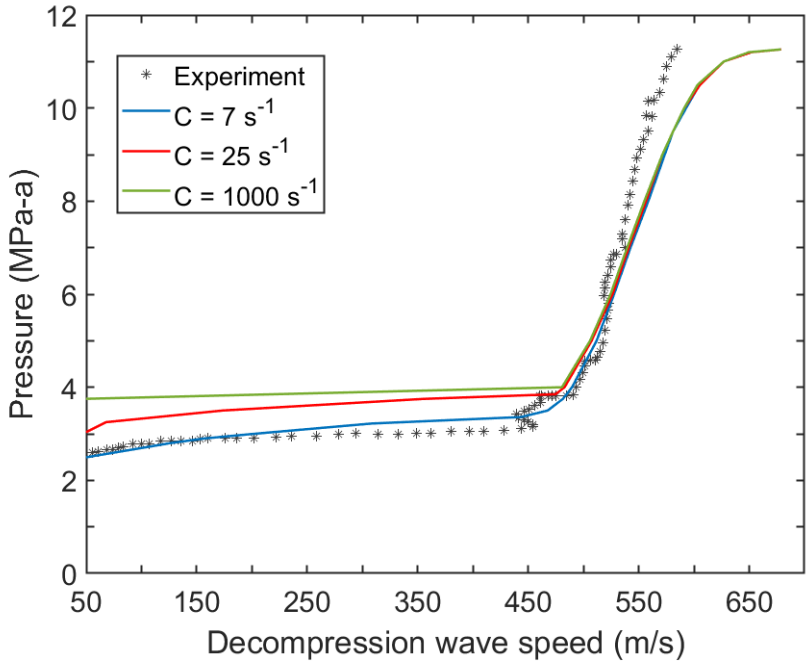

Figure 5-11. Comparison of predicted and experimental average decompression wave speed.

The effect of the mass transfer coefficient (C) on the prediction of the decompression wave speed curve is predominant in the pressure plateau region. Since

phase transition does not occur when the pressure is higher than the plateau, the mass transfer coefficient representing the evaporation rate does not have a relevant effect on the region corresponding to the initial fast pressure drop. Nevertheless, similar to the effect of C on the pressure-time traces, this coefficient significantly affects the prediction of the plateau in the decompression wave speed curve. A higher mass transfer coefficient leads to a plateau at higher pressure due to less deviation from equilibrium saturation conditions.

To better understand how the thermodynamic approach in the CFD model affects the prediction of the decompression wave speed, Figure 5-12 combines the results for the C value that generates the most accurate prediction in Figure 4-10 (PR, C = 8 s^{-1}) and the curve corresponding to the best model performance in Figure 5-11 (SW, C = 7 s^{-1}). Both decompression wave speed predictions were calculated using the slopes for different isobars, implementing four pressure transducers' locations. Since the value of the mass transfer coefficient (C) is proven to have an impact only on the plateau of the decompression wave speed curve, the model predictions for PR using C = 8 s^{-1} can be compared with the results for SW with C = 7 s^{-1}, being certain that a minor difference in the mass transfer coefficient only translates into a slight discrepancy in the pressure plateau, while it does not have an effect on the region corresponding to the initial fast pressure drop.

In general, based on the comparison shown in Figure 5-12, the SW approach predicts the fast pressure drop region more accurately than the CFD model using PR. The more accurate prediction of the liquid speed of sound when using SW may be the reason for the improvement in the prediction of this region. To illustrate the enhancement of the

model when incorporating the SW approach, it is worth to compare the pressure associated to some decompression wave speed values. For instance, an average decompression wave speed of 500 m/s is related to 4.3 MPa-a for both experimental and SW prediction; however, the pressure predicted by the PR model corresponds to 10 MPa-a. An additional example is the pressure associated to 540 m/s, which is 7 MPa-a in the case of the shock tube test and SW correlations, whereas the PR approach predicts 11 MPa-a. These results suggest that a significantly slower depressurization is simulated by the CFD model when incorporating the PR EoS. Although the general trend of the decompression wave speed improves when implementing SW, for a pressure higher than 7 MPa-a, the experimental pressure is higher than the predicted pressure, indicating that the simulated average decompression wave speed is larger than the experimental value.

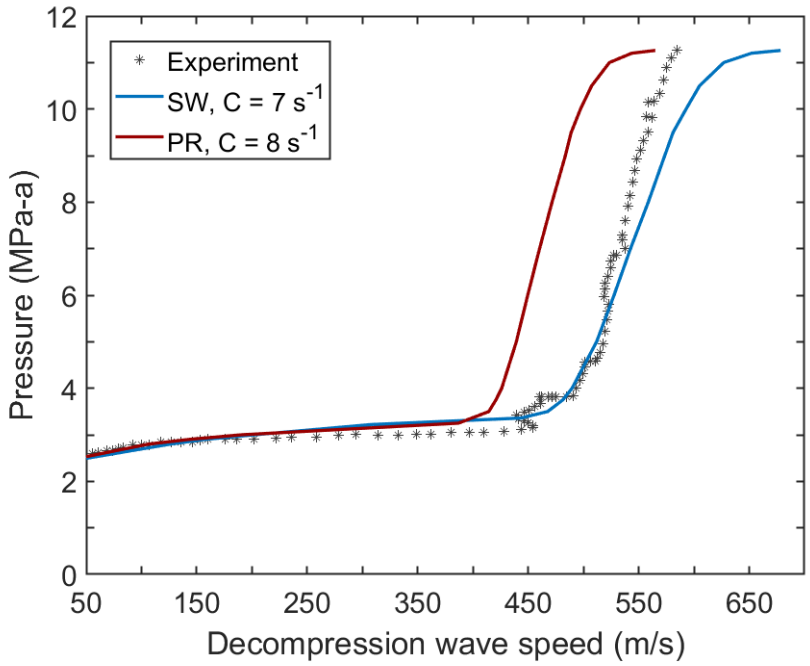

Figure 5-12. SW vs. PR: average decompression wave speed.

Despite the fact that the model prediction differs in the region of fast pressure drop depending on the thermodynamic approach, the pressure plateau for SW and PR match the experimental results very accurately.

5.2.4. Local decompression wave speed

Different from the average decompression wave speed which calculation involves the time and pressure readings of several pressure transducers' locations simultaneously, the CFD model can determine the local decompression wave speed at any specific location along the pipeline, subtracting the local outflow velocity from the local speed of sound of the fluid. Since the local and average decompression wave speeds are calculated using different methods, their comparison should be carefully conducted. In addition, it should be noted that the shock tube test does not provide local decompression wave speeds.

Figure 5-13 illustrates the model prediction for the local decompression wave speed and the speed of sound of the fluid at 0.2 m from the open-end (PT2 location). Besides, this plot includes the average decompression wave speed reported by Botros *et al.* (2015) [15] for the shock tube test 32A. A point-by-point comparison between the model prediction for the local decompression wave speed and the average decompression wave speed obtained from the experiment is not suitable since the behavior of the former varies with position (specifically the pressure plateau region of the curve). Nevertheless, the trend of both curves is very similar and the predicted local speed overlaps some portions of the average speed curve obtained from the experiment.

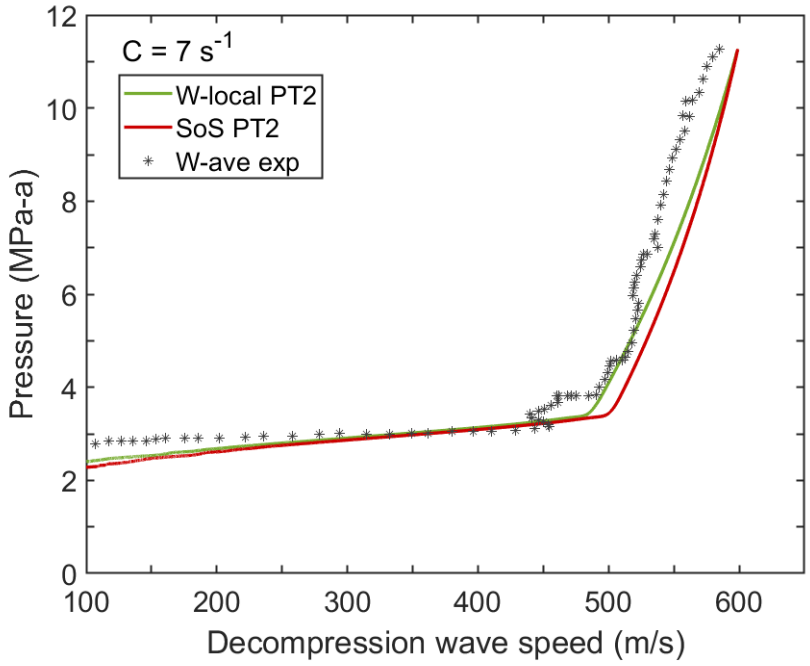

Figure 5-13. Comparison between decompression wave speed and speed of sound.

Contrasting the model prediction for the local decompression wave speed with the local speed of sound of the fluid, both show a very similar behavior along the expansion process. The initial value of these two variables is identical (around 600 m/s) since the initial conditions of the model dictate zero fluid velocity before the pipeline ruptures. In addition, for the region of rapid pressure drop from the initial conditions up to the formation of the plateau, the speed of sound of the system corresponds to the speed of sound of the liquid, since no phase transition occurs before reaching the plateau. Besides, this region shows that for a specific pressure, the local decompression wave speed is lower than the speed of sound, this occurs due to the subtraction of the fluid velocity from the latter to obtain the former. Lastly, the plateau of the local expansion wave speed in Figure 5-13 results from the discontinuity of the speed of sound due to the phase transition, since

the speed of sound of the two-phase mixture is commonly lower than the liquid sound speed.

In general, the decompression wave speed is predominantly governed by the speed of sound of the fluid. Therefore, when incorporating the SW approach into the multiphase CFD model, the more accurate calculation of the liquid speed of sound improves the prediction of the decompression wave speed, enhancing the modeling of the expansion process in contrast with the PR EoS. A better prediction of the decompression wave speed avoids the delay in the wave front arrival at different pressure transducers' locations, which is reported in the pressure-time traces when using PR. The significant improvement in the model predictions using SW is demonstrated when comparing Figure 4-1 with Figure 5-1.

5.2.5. Distribution of variables along the pipeline

Figure 5-14 depicts the distribution of pressure, temperature and liquid volume fraction for the SW and PR approaches after 10 ms along 8 m from the open-end, which corresponds to 34 m to 42 m location with respect to the closed-end of the pipeline. Both thermodynamic approaches incorporate a mass transfer coefficient $C = 7\ s^{-1}$.

The pressure distribution along the pipeline consists of four different regions. Firstly, the region where the decompression wave has not arrived and the pressure has not decreased from its initial value (11.27 MPa-a). Secondly, the region of fast pressure drop from the location of the decompression wave front (36 m for SW, 37 m for PR) up to the saturation pressure around 4 MPa-a. The third region comprises the plateau at saturation

conditions. Lastly, the fourth section extends from the location of the evaporation front to the pipeline outlet. A more robust analysis of the four regions is conducted later.

One of the most important observations when contrasting the pressure distribution predicted with the SW and the PR approaches is about the gap between the decompression (or expansion) wave front. After the pipeline ruptures, a decompression wave travels from the open-end (42 m location) to the closed-end (zero coordinate). The location of the expansion wave front for a specific time corresponds to the beginning of the pressure decrease, which is located at 36 m from the closed-end for the SW approach and 37 m when using the PR EoS. Therefore, the decompression wave has traveled 6 m after simulating 10 ms with the SW approach, and 5 m for the PR case. This gap between both predictions is related to the lower decompression wave speed calculated when incorporating PR into the CFD model, which is discussed in Section 5.2.3. and Section 5.2.4. After 10 ms, the difference between the location of the expansion wave front predicted by each approach is 1 m, however, this gap is expected to increase as time passes.

The arrival of the decompression front generates an immediate decrease in both pressure and temperature. Therefore, the four regions identified in the pressure distribution are also applicable when describing the temperature distribution along the pipeline. In addition, the specific locations limiting each of those sections match the temperature and pressure profiles.

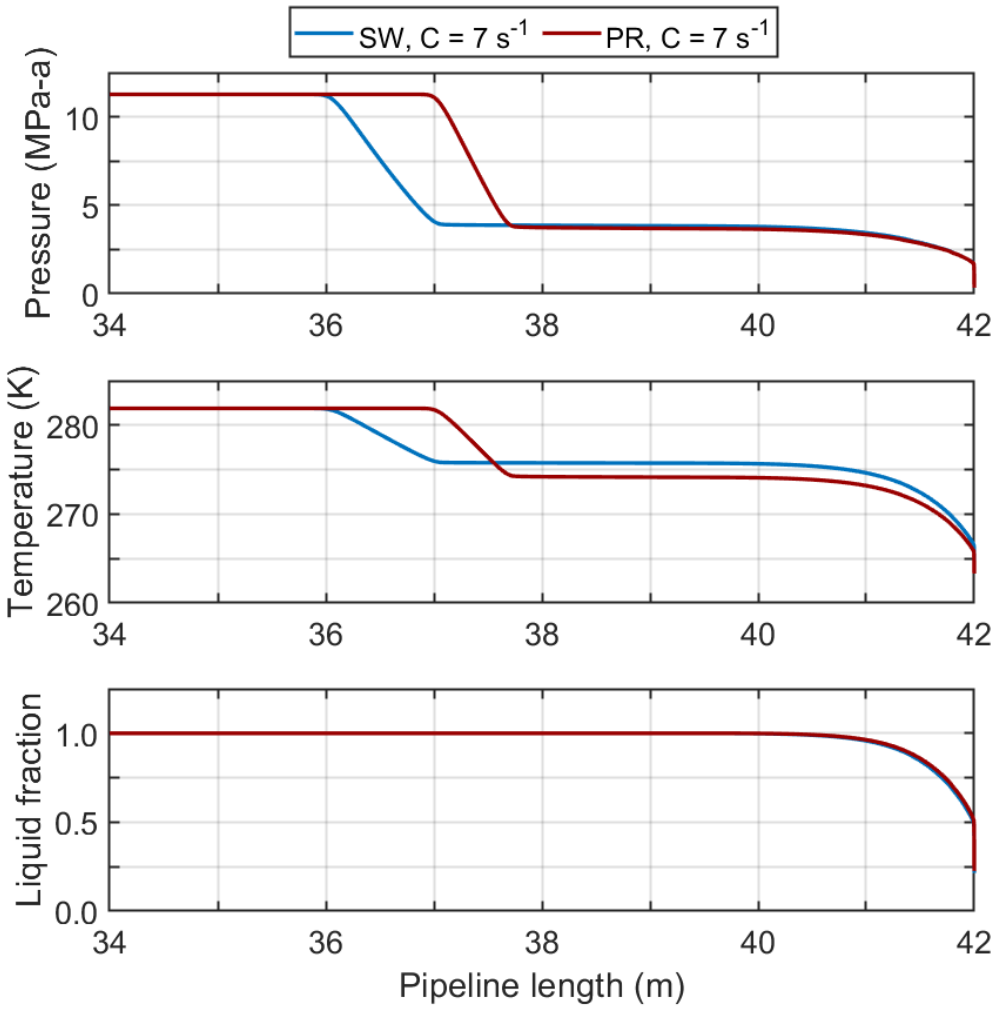

Figure 5-14. Distribution of pressure, temperature and liquid volume fraction along the pipeline at 10 ms.

The distribution of liquid volume fraction along the pipeline shows that the liquid phase predominates in the major part of the 8 m section illustrated in Figure 5-14. After 10 ms, the phase transition has started adjacent to the outlet, where the CFD model reports liquid volume fractions lower than one. Closer to the open-end, more vaporization occurs and lower liquid volume fractions are obtained. The SW approach reports a liquid fraction of 0.21 at the outlet, which corresponds to a vapor fraction of 0.79.

When contrasting the pressure and liquid volume fraction distributions, two different fronts are generated, the decompression wave front and the evaporation front. The latter corresponds to the location where the liquid volume fraction starts to show values lower than one [80]. Therefore, an evaporation front is usually treated as a discontinuity between liquid and a liquid-vapor mixture [81]. To clarify the exact location of the evaporation front, Figure 5-15 depicts the distribution of the source term representing the mass transferred from the liquid to the vapor during the evaporation process, when incorporating the SW correlations into the CFD model. This mass source term is defined as follows:

$$S_e = C\alpha_l\rho_l\frac{P_{sat} - P}{P_{sat}} \quad when\ P \leq P_{sat} \qquad \textbf{(5-1)}$$

Where S_e is the evaporation mass source term, C is the mass transfer coefficient representing the vaporization rate, α_l is the liquid volume fraction, ρ_l is the liquid density, P_{sat} is the saturation pressure and P is the system's pressure. As shown in the previous formula, when reaching the saturation conditions the evaporation mass source term becomes zero. Therefore, the mass and energy transfer involved in the evaporation starts when $P < P_{sat}$, which corresponds to superheated liquid. This evaporation criterion related to metastable conditions is applied by some authors [82, 83]. For a specific time, the distribution of the mass source term along the pipeline allows identifying the location of the evaporation front, since the start of the phase transition corresponds to the boundary between $S_e = 0$ (saturation conditions) and $S_e > 0$ (metastable conditions).

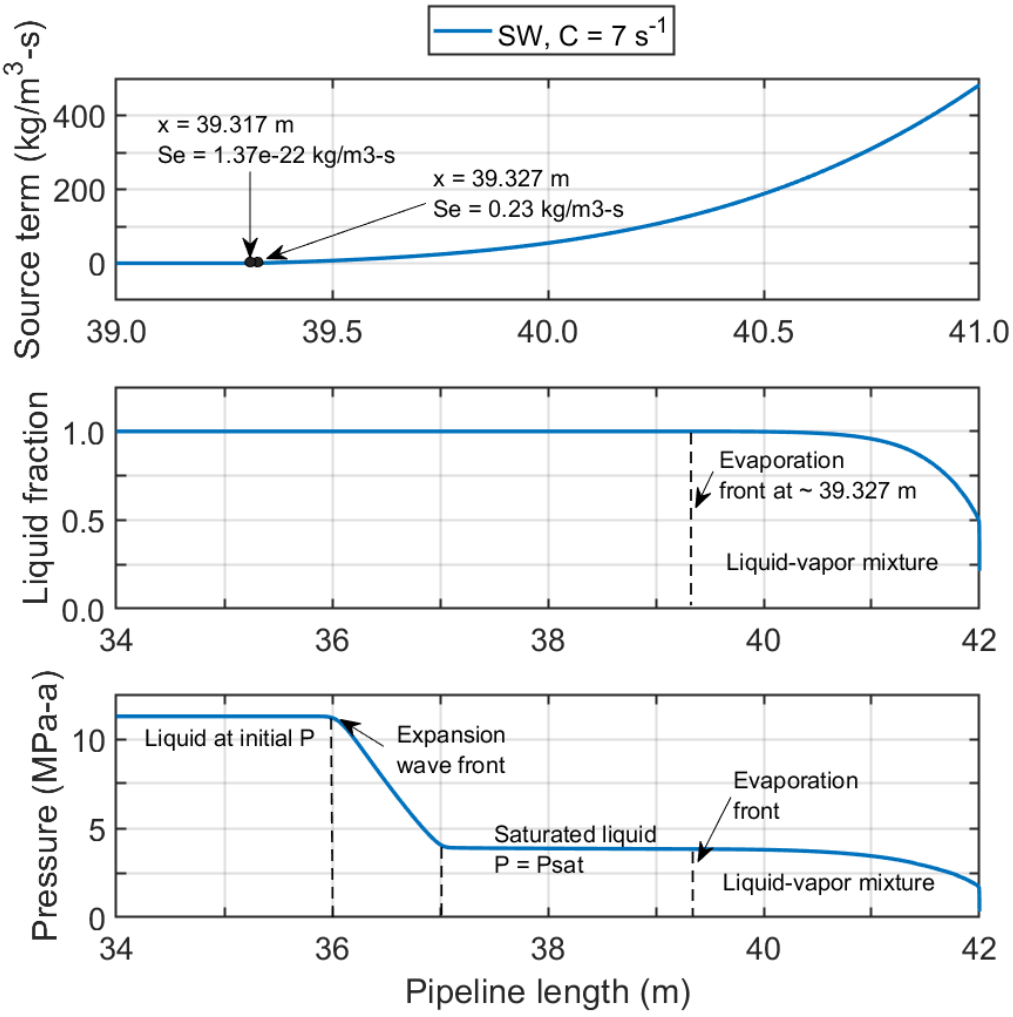

Figure 5-15. Distribution of evaporation mass source term along the pipeline, and location of expansion and evaporation front at 10 ms.

In terms of Figure 5-15, the mass source term representing the evaporation has an order of magnitude of 10^{-22} at x = 39.317 m. In contrast, the source term at x = 39.327 m is 0.23 kg/m^3-s. Hence, after 10 ms, the CFD model with SW predicts that the evaporation front is located near 39.327 m from the closed-end. It should be noted that in Figure 5-15, the horizontal axis for the mass source term distribution only presents data from 39 m to 41 m. Furthermore, the evaporation front is depicted in the plots corresponding to the

liquid volume fraction and the pressure distribution. A detailed description of different sections along the pipeline is shown in the latter. From left to right, the first region corresponds to the undisturbed liquid (34 m to 36 m); since the decompression wave has not arrived at this section of the pipeline after 10 ms, the pressure is equal to its initial value. The subsequent arrival of the decompression wave generates a rapid decrease in pressure from 36 m to 37 m. Then, saturation conditions are achieved, however, no phase transition has started in the present model due to the assumption of non-equilibrium evaporation, leading to a saturated liquid state until ~39.3 m. As the pressure decreases slightly below the saturation pressure, the phase transition starts. The beginning of non-equilibrium vapor generation matches the evaporation front. On the right side of this phase transition front up to the outlet, a region of liquid-vapor mixture is shown. Since $P < P_{sat}$, an irreversible mass transfer process occurs between metastable liquid and saturated vapor, as explained by Downar-Zapolski *et al.* (1996) [77]. It is worth to highlight that vapor volume fractions equal to one are not reached in the time scale simulated, indicating that total evaporation has not occurred.

A faster decompression wave in comparison to the evaporation front has been reported by several authors [80, 84-86]. As explained in Section 4.2.4. and Section 5.2.4., the decompression wave moves at the local speed of sound relative to the fluid velocity [87], resulting in the formula where the local outflow velocity (u) is subtracted from the local speed of sound of the mixture (c). Since the location of the decompression wave corresponds to the end of the undisturbed liquid region, the speed of this front is governed by the liquid sound speed at or close the initial pressure and temperature. Literature

suggests that the evaporation front can be treated as a second expansion wave, which speed also corresponds to $c-u$ [82]. Therefore, based on its location, the speed of the evaporation front is predominantly driven by the sound speed of saturated liquid. Since the speed of sound at saturation conditions is lower than the liquid sound speed at/close initial conditions, the evaporation front propagates at a lower speed than the decompression wave. To provide insight into the previous statement, Figure 5-16 illustrates the distribution of the mixture speed of sound along the pipeline. For the SW approach, the mixture speed of sound at 36 m corresponds to 598 m/s (equivalent to the liquid property since no vapor is present at this location), whereas the sound speed at 39.3 m (location of the evaporation front) is 509 m/s. In general, the discontinuity in the speed of sound results in a faster decompression wave in comparison to the evaporation front.

When modeling a depressurization case, the prediction of the speed of sound plays a prominent role, since it defines the speed of the decompression wave propagating along the pipeline. For the region corresponding to the liquid-vapor mixture (*e.g.*, x > 39.3 m after modeling 10 ms with the SW approach), the CFD model calculates the mixture speed of sound with the following expression [58]:

$$c = \sqrt{\frac{1}{(\alpha_l \rho_l + \alpha_v \rho_v)\left(\frac{\alpha_l}{\rho_l c_l^2} + \frac{\alpha_v}{\rho_v c_v^2}\right)}} \qquad \textbf{(5-2)}$$

Where α_l and α_v are the liquid and vapor volume fractions, ρ_l and ρ_v the liquid and vapor densities, c_l and c_v the liquid and vapor sound speeds, respectively. It should be noted that for the region where only the liquid phase exists, the mixture speed of sound

is the same as the liquid sound speed. As depicted in Figure 5-16, the prediction of the mixture speed of sound for the PR approach shows lower values than the SW formulation, especially in the region corresponding to the undisturbed liquid; the CFD model incorporating SW predicts a liquid sound speed of 598 m/s, while 495 m/s is obtained with the PR approach. In addition, the distribution of the mixture speed of sound illustrates the four regions identified in the description of the pressure and temperature distributions for both approaches. Since the two CFD models incorporate the same UDFs for modeling the gas phase properties, the difference between the sound speed predictions significantly reduces as the vapor volume fraction increases, this occurs in the vicinity of the pipeline outlet (x = 42 m).

The distribution of the mixture velocity in Figure 5-16 shows that the arrival of the decompression wave initiates the motion of the fluid at 36 m for SW and 37 m for PR. Also, both models present a very similar prediction for the mixture velocity at x > 37.5 m; this corresponds to an identical prediction of the pressure plateau when employing the same mass transfer coefficient (C) in both thermodynamic approaches.

Although Figure 5-16 shows a significant discrepancy in the prediction of the mixture speed of sound, there are no considerable differences between the prediction of the mixture density when incorporating SW or PR. It is interesting to note that this conclusion may result from the specific range of pressure and temperature handled in the simulation.

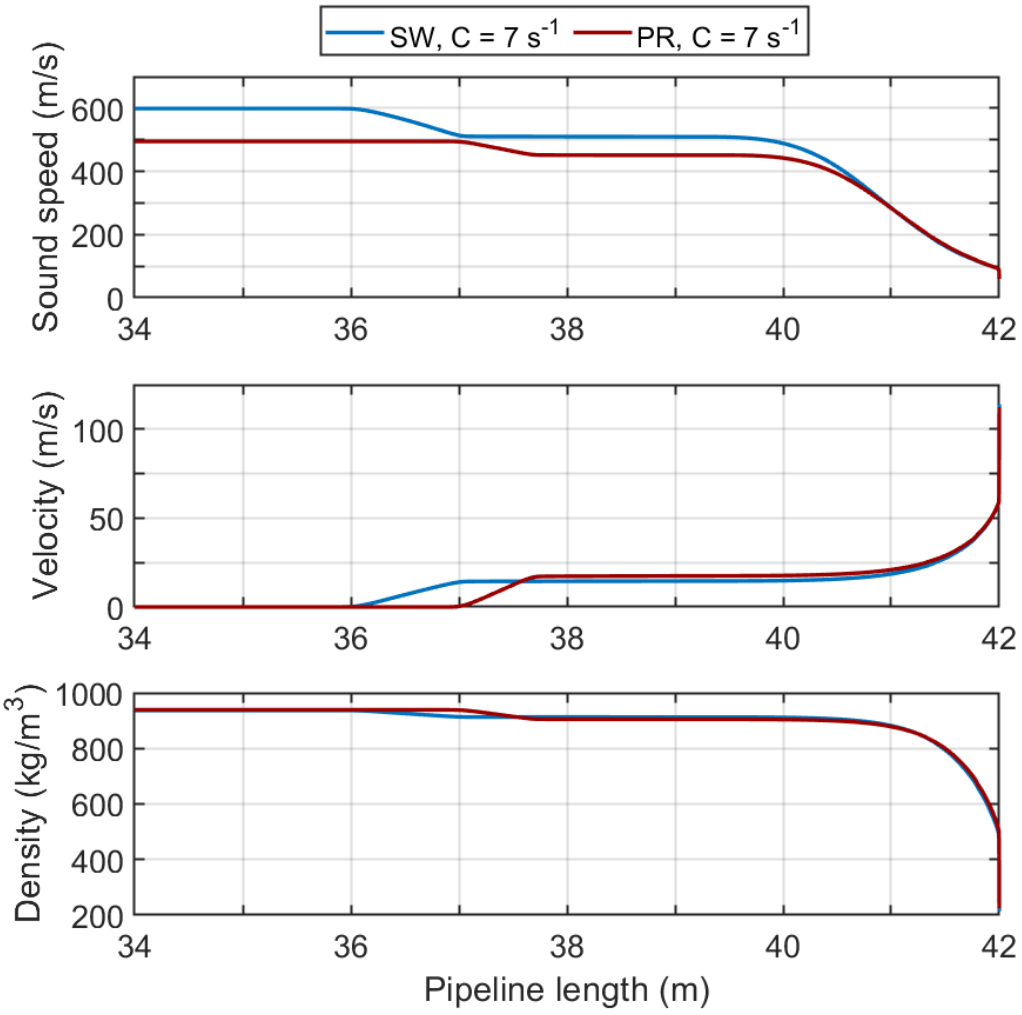

Figure 5-16. Distribution of mixture speed of sound, mixture velocity and mixture density along the pipeline at 10 ms.

5.3. Conclusions

In this work, the effect of the thermodynamic approach on the CFD decompression model was studied. Some of the most important findings are as follows:

- A more accurate CFD model was developed when implementing correlations based on data from the Span-Wagner EoS, in comparison to incorporating the Peng-Robinson EoS for the properties of the liquid phase. Through the

development of thermodynamic correlations, the prediction of the decompression wave speed was improved and therefore the progress of the expansion along the pipeline.

- The thermodynamic approach does not seem to have a significant effect on the prediction of the pressure plateau representing the phase transition. The pressure plateau is manly driven by the mass transfer coefficient (C) in the source terms.
- Both thermodynamic approaches show a faster decompression wave front in comparison to the evaporation front. This may be related to the discontinuity of the speed of sound along the computational domain.

In general, the accuracy of the thermodynamic properties of the primary phase (liquid) has a significant effect on the prediction of the decompression wave speed, and thus on the arrival of the expansion wave front at different locations along the pipeline. However, the pressure plateau is primarily governed by the mass transfer coefficient representing the evaporation rate (C).

6. CONCLUSIONS AND FUTURE WORK

6.1. Conclusions

A two-dimensional multiphase decompression model for pure carbon dioxide was developed using the CFD software ANSYS Fluent. This model incorporates non-equilibrium phase transition, in addition to a comparison of the performance of two thermodynamic approaches to predict the properties of the liquid phase, both including the metastable liquid region. The first corresponds to the Peng-Robinson EoS, while the second incorporates a series of correlations developed using data from the Span and Wagner EoS [37] obtained from NIST REFPROP [56]. For both approaches, the properties of the vapor phase are predicted with a virial expansion, together with correlations based on data from the Span and Wagner EoS.

The range of pressure and temperature where the liquid and vapor correlations show an accurate prediction of the thermodynamic properties was selected based on the results of the shock tube test 32A conducted by Botros *et al.* (2015) [15]. Therefore, one of the most important contributions of this work is that the methodology can be adopted to model any full-bore rupture depressurization with pure liquefied CO_2, implementing the appropriate set of thermodynamic correlations for the range of pressure and temperature associated with the experiment.

The main conclusions of this research are summarized as follows:

- *Effect of thermodynamic approach on the decompression model:* when contrasting the experimental results [15] with the predictions of the CFD model incorporating

the Peng-Robinson EoS (for the liquid phase) and the CFD model based on thermodynamic correlations, a more accurate prediction of the pressure-time curves along the pipeline and the average decompression wave speed was obtained when implementing correlations based on data from the Span and Wagner EoS. A more accurate prediction of the speed of sound when incorporating SW correlations leads to the improvement in the prediction of the decompression wave speed, and therefore the delay of the wave front arrival in the pressure-time curves predicted by PR (Figure 4-1) is not observed when implementing SW correlations (Figure 5-1). In general, the accuracy of the speed of sound predictions for the primary phase (liquid phase at early stages of the expansion) has a significant effect on the accuracy of the decompression model.

- *Effect of mass transfer coefficient (C) on the decompression model:* for both thermodynamic approaches, the coefficient representing the phase transition does not seem to have a significant effect on the arrival of the decompression wave front at different pressure transducers' locations; the wave front arrives approximately at the same time at a specific location when using different values of the mass transfer coefficient in the CFD model (See pressure-time curves for any thermodynamic approach).

  Similarly, the C value does not have an important effect on the fast pressure drop region of the pressure-temperature and the pressure-average decompression wave speed curves, and therefore different coefficients result in the same trajectory from the initial conditions to the equilibrium saturation conditions. This behavior may

be explained from the definition of this coefficient. Since 'C' represents the vaporization rate, its value would not have an effect before the phase transition starts, which is related to the initial fast pressure drop region of the curves.

In contrast, the C value proves to have a predominant impact on the pressure plateau, which represents the phase transition. A smaller mass transfer coefficient translates into a more pronounced delayed nucleation with respect to the equilibrium saturation conditions, and thus a plateau at lower pressure is expected. In this work, equilibrium vapor generation is obtained when the mass transfer coefficient is as high as 1000 s^{-1}.

When comparing the CFD model predictions with the experimental pressure-time traces and average decompression wave speed, the best prediction of the pressure plateaus for both PR and SW approaches are obtained using small values of the mass transfer coefficient (C = 8 s^{-1} and C = 7 s^{-1}, respectively), which highlights the importance of incorporating the non-equilibrium phase transition assumption when modeling a rapid CO_2 decompression. Since the experimental data evidenced this non-equilibrium vaporization during the first milliseconds of the expansion, a mass transfer coefficient significantly smaller than 1000 s^{-1} generates a model prediction that agrees better with the observed delayed nucleation.

Lastly, a trend towards the recovery of equilibrium is observed as curves representing different mass transfer coefficients approach the saturation line over time (See pressure-temperature curves for both thermodynamic approaches).

- *Distribution of variables along the pipeline:* The gap between the decompression wave front predicted by the CFD model incorporating the PR EoS and the CFD formulation implementing correlations based on the SW EoS is evidenced in the diagram 'pressure vs. pipeline length' reported in Section 5.2.5. This gap is related to the lower decompression wave speed calculated when incorporating the PR EoS. In addition to the decompression wave front, both thermodynamic approaches predict an evaporation front. The latter corresponds to the location along the pipeline where the liquid volume fraction starts to show values lower than one at a specific time. Since the location of the decompression wave corresponds to the end of the undisturbed liquid region, the speed of this front is governed by the liquid sound speed at or close the initial pressure and temperature; in contrast, the speed of the evaporation front is predominantly driven by the sound speed of saturated liquid at lower pressure and temperature. Since the latter is smaller than the former, the evaporation front propagates at a lower speed than the decompression wave. The discontinuity in the speed of sound along the computational domain results in a faster decompression wave in comparison to the evaporation front.

6.2. Future work

One of the most important efforts that may extend the scope of this research is the modeling and validation of CO_2 pipeline puncture scenarios, studying the effect of orifice size and initial conditions on the model predictions. One of the major challenges of the previous research initiative corresponds to capturing the potential transition of multiphase

flow patterns in the pipeline during the decompression. The multiphase mixture approach is specialized in dispersed bubbly or droplet flows. However, since the decompression tends to be slower for a puncture in comparison to a full-bore rupture, phase stratification may occur in the pipeline during the expansion process after the puncture occurs, as reported by Brown *et al.* (2013) [17]. Therefore, a potential transition from bubbly flow to a stratified regime (liquid phase flowing at the bottom and vapor at the top) should be modeled. This involves computational challenges since current multiphase approaches are applicable to a specific flow pattern. Thus, a well-known strategy when modeling regime transitions focuses on choosing the aspect of the flow that is of most interest, and implement the multiphase model specialized in that characteristic. If the phase stratification is the focus while modeling the puncture case, the Volume of Fluid (VOF) approach may be an adequate alternative to represent the decompression of CO_2 pipelines experimenting puncture fractures. Nevertheless, CFD models that can predict multiphase phenomena with a variety of flow patterns is an open research area, as highlighted by Bestion (2014) [88].

A second recommendation for future research consists of developing an expression for the mass transfer coefficient (C) representing the phase transition, potentially varying with time and the horizontal coordinate. For a specific location along the pipeline, the value of this coefficient may tend to increase with time due to the trend towards the recovery of equilibrium. In addition, because of the 'rising plateau' phenomenon explained in Section 4.2.2. (less delayed nucleation with respect to the equilibrium saturation conditions at locations farther away from the open-end), the mass transfer

coefficient C may also vary along the horizontal axis of the pipeline. Some researchers refer to this coefficient as a 'relaxation time factor' [5, 12]. Therefore, the potential relation between 'C' and the relaxation time, which is defined as the time taken by the system to return to equilibrium after the modification of a previous equilibrium state [78] may be investigated. It is worth to mention that empirical correlations for the CO_2 relaxation time are published in the literature [89].

Lastly, another potential area of future research is the implementation of the Eulerian multiphase approach to model the CO_2 decompression for a pipeline full-bore rupture case. In contrast to the multiphase mixture model, the Eulerian approach solves a continuity, momentum and energy conservation equations for each phase. Therefore, the liquid and vapor are not required to share the same pressure and temperature. A comparison of the results implementing a more robust multiphase approach (Eulerian model) with the predictions using the mixture model corresponds to an interesting research alternative.

REFERENCES

[1] F. Lees, Chapter 22 - Storage, in: S. Mannan (Ed.) Lees' Loss Prevention in the Process Industries (Fourth Edition), Butterworth-Heinemann, Oxford, 2012, pp. 1889-1985.

[2] C.J. Wareing, M. Fairweather, R.M. Woolley, S.A.E.G. Falle, Numerical Simulation of CO2 Dispersion From Punctures and Ruptures of Buried High-pressure Dense Phase CO2 Pipelines with Experimental Validation, Energy Procedia 63 (2014) 2500-2509.

[3] X. Liu, A. Godbole, C. Lu, G. Michal, P. Venton, Source strength and dispersion of CO2 releases from high-pressure pipelines: CFD model using real gas equation of state, Applied Energy 126 (2014) 56-68.

[4] X. Liu, A. Godbole, C. Lu, G. Michal, P. Venton, Study of the consequences of CO2 released from high-pressure pipelines, Atmospheric Environment 116 (2015) 51-64.

[5] X. Liu, A. Godbole, C. Lu, B. Liu, P. Venton, Multi-Phase CFD Modelling of CO2 Releases From High-Pressure Pipelines, Proceedings of the 2016 11th International Pipeline Conference, ASME, Calgary, Alberta, Canada, 2016, pp. V002T007A009.

[6] A. Elshahomi, C. Lu, G. Michal, X. Liu, A. Godbole, P. Venton, Decompression wave speed in CO2 mixtures: CFD modelling with the GERG-2008 equation of state, Applied Energy 140 (2015) 20-32.

[7] B. Liu, X. Liu, C. Lu, A. Godbole, G. Michal, A.K. Tieu, Multi-phase decompression modeling of CO2 pipelines, Greenhouse Gases: Science and Technology 7 (2017) 665-679.

[8] H.E. Jie, B.P. Xu, J.X. Wen, R. Cooper, J. Barnett, Predicting the Decompression Characteristics of Carbon Dioxide Using Computational Fluid Dynamics, Proceedings of the 2012 9th International Pipeline Conference, ASME, Calgary, Alberta, Canada, 2012, pp. 585-595.

[9] C.J. Wareing, M. Fairweather, S.A.E.G. Falle, R.M. Woolley, Validation of a model of gas and dense phase CO2 jet releases for carbon capture and storage application, International Journal of Greenhouse Gas Control 20 (2014) 254-271.

[10] R.M. Woolley, M. Fairweather, C.J. Wareing, S.A.E.G. Falle, C. Proust, J. Hebrard, D. Jamois, Experimental measurement and Reynolds-averaged Navier–Stokes modelling of the near-field structure of multi-phase CO2 jet releases, International Journal of Greenhouse Gas Control 18 (2013) 139-149.

[11] R.M. Woolley, M. Fairweather, C.J. Wareing, C. Proust, J. Hebrard, D. Jamois, V.D. Narasimhamurthy, I.E. Storvik, T. Skjold, S.A.E.G. Falle, S. Brown, H. Mahgerefteh, S.

Martynov, S.E. Gant, D.M. Tsangaris, I.G. Economou, G.C. Boulougouris, N.I. Diamantonis, An integrated, multi-scale modelling approach for the simulation of multiphase dispersion from accidental CO2 pipeline releases in realistic terrain, International Journal of Greenhouse Gas Control 27 (2014) 221-238.

[12] B. Liu, X. Liu, C. Lu, A. Godbole, G. Michal, A.K. Tieu, A CFD decompression model for CO2 mixture and the influence of non-equilibrium phase transition, Applied Energy 227 (2018) 516-524.

[13] A. Cosham, D. G. Jones, K. Armstrong, D. Allason, J. Barnett, The Decompression Behaviour of Carbon Dioxide in the Dense Phase, Proceedings of the 2012 9th International Pipeline Conference, ASME, Calgary, Alberta, Canada, 2012.

[14] K.K. Botros, E. Hippert, P. Craidy, Measuring decompression wave speed in CO2 mixtures by a shock tube, Pipelines Int. (2013) 22-26.

[15] K.K. Botros, J. Geerligs, B. Rothwell, T. Robinson, Measurements of Decompression Wave Speed in Pure Carbon Dioxide and Comparison with Predictions by EOS, Journal of Pressure Vessel Technology 138 (2015) 031302-031302-031308.

[16] K.K. Botros, J. Geerligs, B. Rothwell, T. Robinson, Measurements of Decompression Wave Speed in Binary Mixtures of Carbon Dioxide and Impurities, Journal of Pressure Vessel Technology 139 (2016) 021301-021301-021311.

[17] S. Brown, S. Martynov, H. Mahgerefteh, C. Proust, A homogeneous relaxation flow model for the full bore rupture of dense phase CO2 pipelines, International Journal of Greenhouse Gas Control 17 (2013) 349-356.

[18] C. Proust, D. Jamois, J. Hebrard, Experimental investigation of high velocity flow throughout a long pipe, Quantitative failure consequence hazard assesment for next generation CO2 pipelines: The missing link, Project CO2PipeHaz, 2013.

[19] R.M. Woolley, M. Fairweather, C.J. Wareing, S.A.E.G. Falle, H. Mahgerefteh, S. Martynov, S. Brown, V.D. Narasimhamurthy, I.E. Storvik, L. Sælen, T. Skjold, I.G. Economou, D.M. Tsangaris, G.C. Boulougouris, N. Diamantonis, L. Cusco, M. Wardman, S.E. Gant, J. Wilday, Y.C. Zhang, S. Chen, C. Proust, J. Hebrard, D. Jamois, CO2PipeHaz: Quantitative Hazard Assessment for Next Generation CO2 Pipelines, Energy Procedia 63 (2014) 2510-2529.

[20] S. Martynov, S. Brown, H. Mahgerefteh, V. Sundara, S. Chen, Y. Zhang, Modelling three-phase releases of carbon dioxide from high-pressure pipelines, Process Safety and Environmental Protection 92 (2014) 36-46.

[21] J. Brown, H. Holt, K. Helle, Large Scale CO2 Releases for Dispersion Model and Safety Study Validation, Energy Procedia 63 (2014) 2542-2546.

[22] DNV GL, CO2Pipetrans Phase 2 JIP WP1, Review of discharge data for CO2 pipe depresurisation experiments, 2014.

[23] C.J. Wareing, M. Fairweather, S.A.E.G. Falle, R.M. Woolley, A.M.E. Ward, High pressure CO2 CCS pipelines: Comparing dispersion models with multiple experimental datasets, International Journal of Greenhouse Gas Control 54 (2016) 716-726.

[24] S.M. Richardson, G. Saville, Blowdown of LPG Pipelines, Process Safety and Environmental Protection 74 (1996) 235-244.

[25] A. Oke, H. Mahgerefteh, I. Economou, Y. Rykov, A transient outflow model for pipeline puncture, Chemical Engineering Science 58 (2003) 4591-4604.

[26] D. Webber, M. Wardman, An investigation into the performance of the PipeTech computer code in calculating Isle of Grain pipeline blowdown tests, Health and Safety Laboratory, 2010.

[27] H. Mahgerefteh, S. Brown, G. Denton, Modelling the impact of stream impurities on ductile fractures in CO2 pipelines, Chemical Engineering Science 74 (2012) 200-210.

[28] W. Zheng, H. Mahgerefteh, S. Martynov, S. Brown, Modeling of CO2 Decompression across the Triple Point, Industrial & Engineering Chemistry Research 56 (2017) 10491-10499.

[29] E. Aursand, P. Aursand, M. Hammer, H. Lund, The influence of CO2 mixture composition and equations of state on simulations of transient pipeline decompression, International Journal of Greenhouse Gas Control 54 (2016) 599-609.

[30] S.T. Munkejord, M. Hammer, Depressurization of CO2-rich mixtures in pipes: Two-phase flow modelling and comparison with experiments, International Journal of Greenhouse Gas Control 37 (2015) 398-411.

[31] H. Mahgerefteh, P. Saha, I.G. Economou, Fast numerical simulation for full bore rupture of pressurized pipelines, AIChE Journal 45 (1999) 1191-1201.

[32] R.M. Woolley, M. Fairweather, C. Wareing, S. Falle, S. Brown, H. Mahgerefteh, S. Martynov, C. Proust, J. Hebrard, D. Jamois, Numerical Modelling of Heat Transfer Phenomena in Accidental CO2 Pipeline Releases with Experimental Validation, Proceedings of the Eighth International Symposium on Turbulence, Heat and Mass Transfer, Begell House Sarajevo, Bosnia and Herzegovina, 2015.

[33] H.W.M. Witlox, M. Harper, A. Oke, J. Stene, Phast validation of discharge and atmospheric dispersion for pressurised carbon dioxide releases, Journal of Loss Prevention in the Process Industries 30 (2014) 243-255.

[34] H. Versteeg, W. Malalasekera, An introduction to computational fluid dynamics : the finite volume method Second Edition ed., Pearson Education Limited, 2007.

[35] B. Sun, R.P. Utikar, V.K. Pareek, K. Guo, Computational fluid dynamics analysis of liquefied natural gas dispersion for risk assessment strategies, Journal of Loss Prevention in the Process Industries 26 (2013) 117-128.

[36] ANSYS, ANSYS FLUENT Theory Guide, ANSYS Inc., USA (2017).

[37] R. Span, W. Wagner, A New Equation of State for Carbon Dioxide Covering the Fluid Region from the Triple-Point Temperature to 1100 K at Pressures up to 800 MPa, Journal of Physical and Chemical Reference Data 25 (1996) 1509-1596.

[38] A. McGillivray, J.L. Saw, D. Lisbona, M. Wardman, M. Bilio, A risk assessment methodology for high pressure CO2 pipelines using integral consequence modelling, Process Safety and Environmental Protection 92 (2014) 17-26.

[39] S.T. Munkejord, M. Hammer, S.W. Løvseth, CO2 transport: Data and models – A review, Applied Energy 169 (2016) 499-523.

[40] U.K. Deiters, T. Kraska, Chapter 7 - Equations of State for Pure Fluids, in: U.K. Deiters, T. Kraska (Eds.) Supercritical Fluid Science and Technology, Elsevier, 2012, pp. 177-210.

[41] A.S. Teja, L.J. Holm, DISTILLATION | Vapour–Liquid Equilibrium: Theory, in: I.D. Wilson (Ed.) Encyclopedia of Separation Science, Academic Press, Oxford, 2000, pp. 1159-1169.

[42] D.-Y. Peng, D.B. Robinson, A New Two-Constant Equation of State, Industrial & Engineering Chemistry Fundamentals 15 (1976) 59-64.

[43] P. Aursand, M.A. Gjennestad, E. Aursand, M. Hammer, Ø. Wilhelmsen, The spinodal of single- and multi-component fluids and its role in the development of modern equations of state, Fluid Phase Equilibria 436 (2017) 98-112.

[44] M. Salimi, A. Bahramian, The Prediction of the Speed of Sound in Hydrocarbon Liquids and Gases: The Peng-Robinson Equation of State Versus SAFT-BACK, Petroleum Science and Technology 32 (2014) 409-417.

[45] O. Kunz, W. Wagner, The GERG-2008 Wide-Range Equation of State for Natural Gases and Other Mixtures: An Expansion of GERG-2004, Journal of Chemical & Engineering Data 57 (2012) 3032-3091.

[46] L.H.H.P. Pham, R. Rusli, A review of experimental and modelling methods for accidental release behaviour of high-pressurised CO2 pipelines at atmospheric environment, Process Safety and Environmental Protection 104 (2016) 48-84.

[47] C. Gough, L. O'Keefe, S. Mander, Public perceptions of CO2 transportation in pipelines, Energy Policy 70 (2014) 106-114.

[48] M. Wallace, L. Goudarzi, K. Callahan, W. R., A Review of the CO2 Pipeline Infrastructure in the U.S. , U.S. Department of Energy, Office of Fossil Energy, 2015.

[49] J.X. Wen, P. Le Fur, H. Jie, C.M.R. Vendra, Further development and validation of CO2FOAM for the atmospheric dispersion of accidental releases from carbon dioxide pipelines, International Journal of Greenhouse Gas Control 52 (2016) 293-304.

[50] C. Vianello, P. Mocellin, S. Macchietto, G. Maschio, Risk assessment in a hypothetical network pipeline in UK transporting carbon dioxide, Journal of Loss Prevention in the Process Industries 44 (2016) 515-527.

[51] X. Liu, A. Godbole, C. Lu, G. Michal, V. Linton, Investigation of the consequence of high-pressure CO2 pipeline failure through experimental and numerical studies, Applied Energy 250 (2019) 32-47.

[52] N.A. Azzolina, D.V. Nakles, C.D. Gorecki, W.D. Peck, S.C. Ayash, L.S. Melzer, S. Chatterjee, CO2 storage associated with CO2 enhanced oil recovery: A statistical analysis of historical operations, International Journal of Greenhouse Gas Control 37 (2015) 384-397.

[53] H. Mahgerefteh, S. Brown, S. Martynov, A study of the effects of friction, heat transfer, and stream impurities on the decompression behavior in CO2 pipelines, Greenhouse Gases: Science and Technology 2 (2012) 369-379.

[54] P. Joshi, P. Bikkina, Q. Wang, Consequence analysis of accidental release of supercritical carbon dioxide from high pressure pipelines, International Journal of Greenhouse Gas Control 55 (2016) 166-176.

[55] PHMSA, Pipeline Incident 20 Year Trends (Online Database), U.S. Department of Transportation, 2018.

[56] E.W. Lemmon, M.L. Huber, M.O. McLinden, NIST Standard Reference Database 23: NIST Reference Fluid Thermodynamic and Transport Properties - REFPROP (Version 9.1), U.S. Department of Commerce: Gaithersburg, Maryland (2013).

[57] S. Martynov, S. Brown, H. Mahgerefteh, V. Sundara, Modelling choked flow for CO2 from the dense phase to below the triple point, International Journal of Greenhouse Gas Control 19 (2013) 552-558.

[58] F. Giacomelli, F. Mazzelli, A. Milazzo, A novel CFD approach for the computation of R744 flashing nozzles in compressible and metastable conditions, Energy 162 (2018) 1092-1105.

[59] M. Labois, C. Narayanan, Non-conservative pressure-based compressible formulation for multiphase flows with heat and mass transfer, International Journal of Multiphase Flow 96 (2017) 24-33.

[60] I.J. Keshtiban, Belblidia, F., Webster, M.F., Compressible flow solvers for low mach number flows - A review, International Journal for Numerical Methods in Fluids 23 (2004) 77-103.

[61] K.C. Karki, S.V. Patankar, Pressure based calculation procedure for viscous flows at all speedsin arbitrary configurations, AIAA Journal 27 (1989) 1167-1174.

[62] C.W. Hirt, B.D. Nichols, Volume of fluid (VOF) method for the dynamics of free boundaries, Journal of Computational Physics 39 (1981) 201-225.

[63] Z. Yang, X.F. Peng, P. Ye, Numerical and experimental investigation of two phase flow during boiling in a coiled tube, International Journal of Heat and Mass Transfer 51 (2008) 1003-1016.

[64] H.L. Wu, X.F. Peng, P. Ye, Y. Eric Gong, Simulation of refrigerant flow boiling in serpentine tubes, International Journal of Heat and Mass Transfer 50 (2007) 1186-1195.

[65] K.K. Botros, W. Studzinski, J. Geerligs, A. Glover, Determination of Decompression Wave Speed in Rich Gas Mixtures, The Canadian Journal of Chemical Engineering 82 (2004) 880-891.

[66] C.-H. Lee, C. Xu, Z. Huang, A three-phase flow simulation of local scour caused by a submerged wall jet with a water-air interface, Advances in Water Resources 129 (2019) 373-384.

[67] A.B. Desamala, V. Vijayan, A. Dasari, A.K. Dasmahapatra, T.K. Mandal, Prediction of oil-water flow patterns, radial distribution of volume fraction, pressure and velocity during separated flows in horizontal pipe, Journal of Hydrodynamics, Ser. B 28 (2016) 658-668.

[68] M. Manninen, V. Taivassalo, S. Kallio, On the Mixture Model for Multiphase Flow, VTT Publications, 1996.

[69] M. Ishii, T. Hibiki, Thermo-Fluid Dynamics of Two-Phase Flow, 2 ed., Springer-Verlag, New York, 2011.

[70] A. Cosham, D.G. Jones, K. Armstrong, D. Allason, J. Barnett, Ruptures in Gas Pipelines, Liquid Pipelines and Dense Phase Carbon Dioxide Pipelines, (2012) 465-482.

[71] J.-h. Wei, L.-m. Pan, D.-q. Chen, H. Zhang, J.-j. Xu, Y.-p. Huang, Numerical simulation of bubble behaviors in subcooled flow boiling under swing motion, Nuclear Engineering and Design 241 (2011) 2898-2908.

[72] J.P. O'Connell, J.M. Prausnitz, Empirical Correlation of Second Virial Coefficients for Vapor-Liquid Equilibrium Calculations, Industrial & Engineering Chemistry Process Design and Development 6 (1967) 245-250.

[73] C. Tsonopoulos, An empirical correlation of second virial coefficients, AIChE Journal 20 (1974) 263-272.

[74] K.H. Kumar, K.E. Starling, The most general density-cubic equation of state: application to pure nonpolar fluids, Industrial & Engineering Chemistry Fundamentals 21 (1982) 255-262.

[75] V. Vesovic, W.A. Wakeham, G.A. Olchowy, J.V. Sengers, J.T.R. Watson, J. Millat, The Transport Properties of Carbon Dioxide, Journal of Physical and Chemical Reference Data 19 (1990) 763-808.

[76] A. Fenghour, W.A. Wakeham, V. Vesovic, The Viscosity of Carbon Dioxide, Journal of Physical and Chemical Reference Data 27 (1998) 31-44.

[77] P. Downar-Zapolski, Z. Bilicki, L. Bolle, J. Franco, The non-equilibrium relaxation model for one-dimensional flashing liquid flow, International Journal of Multiphase Flow 22 (1996) 473-483.

[78] R. Benintendi, Non-equilibrium phenomena in carbon dioxide expansion, Process Safety and Environmental Protection 92 (2014) 47-59.

[79] S. Gu, Y. Li, L. Teng, Q. Hu, D. Zhang, X. Ye, C. Wang, J. Wang, S. Iglauer, A new model for predicting the decompression behavior of CO2 mixtures in various phases, Process Safety and Environmental Protection 120 (2018) 237-247.

[80] Y. Fang, M. De Lorenzo, P. Lafon, S. Poncet, Y. Bartosiewicz, An Accurate and Efficient Look-up Table Equation of State for Two-Phase Compressible Flow Simulations of Carbon Dioxide, Industrial & Engineering Chemistry Research 57 (2018) 7676-7691.

[81] L.G. Hill, B. Sturtevant, An Experimental Study of Evaporation Waves in a Superheated Liquid, Springer Berlin Heidelberg, Berlin, Heidelberg, 1990, pp. 25-37.

[82] R. Saurel, F. Petitpas, R. Abgrall, Modelling phase transition in metastable liquids: application to cavitating and flashing flows, Journal of Fluid Mechanics 607 (2008) 313-350.

[83] A. Zein, M. Hantke, G. Warnecke, Modeling phase transition for compressible two-phase flows applied to metastable liquids, Journal of Computational Physics 229 (2010) 2964-2998.

[84] H. Lund, T. Flåtten, S. Tollak Munkejord, Depressurization of carbon dioxide in pipelines–Models and methods, Energy Procedia 4 (2011) 2984-2991.

[85] K.E.T. Giljarhus, S.T. Munkejord, G. Skaugen, Solution of the Span–Wagner Equation of State Using a Density–Energy State Function for Fluid-Dynamic Simulation of Carbon Dioxide, Industrial & Engineering Chemistry Research 51 (2012) 1006-1014.

[86] M. Hammer, Å. Ervik, S.T. Munkejord, Method Using a Density–Energy State Function with a Reference Equation of State for Fluid-Dynamics Simulation of Vapor–Liquid–Solid Carbon Dioxide, Industrial & Engineering Chemistry Research 52 (2013) 9965-9978.

[87] E. Aursand, S. Dumoulin, M. Hammer, H.I. Lange, A. Morin, S.T. Munkejord, H.O. Nordhagen, Fracture propagation control in CO2 pipelines: Validation of a coupled fluid–structure model, Engineering Structures 123 (2016) 192-212.

[88] D. Bestion, The difficult challenge of a two-phase CFD modelling for all flow regimes, Nuclear Engineering and Design 279 (2014) 116-125.

[89] W. Angielczyk, Y. Bartosiewicz, D. Butrymowicz, J.-M. Seynhaeve, 1-D Modeling Of Supersonic Carbon Dioxide Two-Phase Flow Through Ejector Motive Nozzle, International Refrigeration and Air Conditioning Conference, Purdue University (2010).

APPENDIX A

USER-DEFINED FUNCTION FOR MASS SOURCE TERM (LIQUID TO GAS)

```
/* UDF to define mass transfer based on Saturation Pressure.
The "from" phase is the liquid and the "to" phase is the gas phase  */
/* C=7 s-1 */

#include "udf.h"

DEFINE_MASS_TRANSFER(liquidtogas, cell, mixthread, from_index,
                     from_species_index, to_index, to_species_index)
{
   double mlg;
   double h1=-794.2273375;
   double h2=1230.757147;
   double h3=-730.1884841;
   double h4=156.4942757;
   double h5=144.5115827;
   double Tc=304.128; /*Kelvin*/

   Thread *liq = THREAD_SUB_THREAD(mixthread, from_index);
   Thread *gas = THREAD_SUB_THREAD(mixthread, to_index);

   double Tr=C_T(cell, mixthread)/Tc;
   double u=1.0/Tr;
   double MPa=h1+u*(h2+u*(h3+h4*u))+h5*Tr*Tr; /*MPa*/
   double P_SAT=MPa*1000000;   /*Pa*/

   mlg = 0.;
   if (C_P(cell, liq) <= P_SAT)      /*Evaporation*/
     {
       mlg = 7*C_VOF(cell,liq)*C_R(cell,liq)*
             fabs(P_SAT-C_P(cell,liq))/P_SAT;
     }
   if ((mlg == 0. ) && (C_P(cell, gas) > P_SAT))    /*Condensation*/
     {
       mlg = -7*C_VOF(cell,gas)*C_R(cell,gas)*
          fabs(C_P(cell,gas)-P_SAT)/P_SAT;
     }
      return (mlg);
}
```

APPENDIX B

USER-DEFINED FUNCTIONS FOR THE VAPOR- PHASE PROPERTIES

- User-defined function for density and speed of sound:

```
/* UDF to calculate vapor density */

#include "udf.h"

# define x1 -0.863785657850155
# define x2 1.95573550099636
# define x3 -2.34794489052861
# define x4 0.438702999993414
# define x5 0.127960990689650
# define Tc 304.128 /*Kelvin (From Fluent)*/
# define rhoc 10624.9 /* This is critical density in mol/m^3*/
# define R  8.3144598  /*Pa*m^3/mol K */
# define MW 44.00995 /*grams/mole (From Fluent)*/
# define PI 3.141592654
# define y1 67.582
# define y2 300.75
# define y3 -97.301
# define y4 -759.37
# define y5 579.11
# define y6 -12.035
# define y7 89.187

DEFINE_PROPERTY(VirialgasRho, c, t)
{
    double Tr, Tao, B, C;
    double Te = C_T(c,t);   /*This is to input the T from Fluent*/
    double Pre = C_P(c,t);   /*This is to input the P from Fluent*/
    double a1, a2, a3, a4;
    double a, b, d, Q, Q3, Re, M;
    double S2, T2, theta, r1, r2, r3;
    double root, rho;

    Tr=Te/Tc;
    Tao=1/Tr;
    B=x1+Tao*(x2+Tao*x3);
    C=x4+Tao*x5;

    a1=C*R*Te/(rhoc*rhoc);  /*a1, a2, a3 and a4 are the coeff of the polynomia*/
    a2=B*R*Te/rhoc;
    a3=R*Te;
    a4=-Pre;
```

```
    /*To calculate the roots */
    a=a2/a1;
    b=a3/a1;
    d=a4/a1; /*c was changed by d because c is a Fluent formal parameter*/

    Q=(a*a-3*b)/9;
    Q3=Q*Q*Q;
    Re=(2*a*a*a-9*a*b+27*d)/54;
    M=Re*Re-Q3;  /*Discriminant*/

    if (M>0) { /*The polinomial has only one root (Zone A or D)*/
     S2=(-Re/fabs(Re))*pow(fabs(Re)+sqrt(M), 1.0/3.0);
     T2=Q/S2;
     root=S2+T2-(a/3);
    }else{
    /*Let's continue with M<0 (Zone B or C)*/
     theta=acos(Re/(sqrt(Q3))); /*theta has to be calculated in radians*/
     r1=-(2*sqrt(Q)*cos(theta/3))-(a/3);
     r2=-(2*sqrt(Q)*cos((theta+2*PI)/3))-(a/3);
     r3=-(2*sqrt(Q)*cos((theta-2*PI)/3))-(a/3);

    if ((r1<r2) && (r1<r3)){
        root=r1;
      }else{
        if ((r2<r1) && (r2<r3)){
        root=r2;
        }else{
        root=r3;
        }
    }
    }
    rho=root*MW/1000;
    return rho;  /*kg/m^3*/
}


DEFINE_PROPERTY(sound_speed_gas, c,t)
{
    double Tr, Ass, Bss, Css, rhor, SoS;
    double Te = C_T(c,t);
    double den = C_R(c,t);  /*This is to try to get the density*/

    Tr=Te/Tc;
    Ass=y1+Tr*(y2+Tr*y3);
    Bss=y4+Tr*y5;
    Css=y6+Tr*y7;

    rhor=(den*1000)/(rhoc*MW);
    SoS=Ass+rhor*(Bss+Css*rhor); /* m/s */
    return SoS;
}
```

- User-defined function for specific heat capacity at constant pressure:

```
/* UDF to calculate vapor Cp at saturation conditions */

#include "udf.h"
# define z1 -26728.01441
# define z2 46229.37206
# define z3 -29992.16026
# define z4 6919.491991
# define z5 3579.667688
# define Tc 304.128 /*Kelvin (From Fluent)*/

DEFINE_SPECIFIC_HEAT(CpGasSat, T, Tref, h, yi)
{
    double Tr, u, Cp1, Cpgas;
    Tr=T/Tc;
    u=1/Tr;
    Cp1=z1+u*(z2+u*(z3+z4*u))+z5*Tr*Tr;  /*(kJ/kg K)*/
    Cpgas=Cp1*1000;
    return Cpgas;  /* J/kg K */
}
```

- User-defined function for thermal conductivity:

```
/* UDF to calculate vapor thermal conductivity at
saturation conditions (same approach as Cp) */

#include "udf.h"
# define j1 -4.74103
# define j2 16.61055
# define j3 -19.39789
# define j4 7.57694
# define Tc 304.128 /*Kelvin (From Fluent)*/

DEFINE_PROPERTY(ThermalConductGas, c, t)
{
    double Tr, Kgas;
    double Te = C_T(c,t); /*This is to input the T from Fluent*/
    Tr=Te/Tc;

    Kgas=j1+Tr*(j2+Tr*(j3+j4*Tr));  /*(W/m K)*/
    return Kgas;
}
```

- User-defined function for viscosity:

```
/* UDF to calculate vapor viscosity at
saturation conditions (same approach as Cp) */

#include "udf.h"
# define f1 -0.0076279
# define f2 0.0269916
# define f3 -0.0315466
# define f4 0.0123954
# define Tc 304.128 /*Kelvin (From Fluent)*/

DEFINE_PROPERTY(ViscosityGas, c, t)
{
    double Tr, M, Miugas;
    double Te = C_T(c,t); /*This is to input T from Fluent*/
    Tr=Te/Tc;

    M=f1+Tr*(f2+Tr*(f3+f4*Tr));  /*(g/cm s)*/
    Miugas=M/10.0;  /*(kg/m s)*/
    return Miugas;
}
```

APPENDIX C

COEFFICIENTS IN CORRELATIONS FOR UDRGM: LIQUID-PHASE PROPERTIES

Property	Coefficients in correlation		
Density (kg/m^3)	$x_1 = -2637.361$ $x_2 = 1237.836$ $x_3 = 3219.313$ $x_4 = -1256.590$ $x_5 = 2837.835$ $x_6 = -4286.871$	$x_7 = 1083.571$ $x_8 = -17.728$ $x_9 = -746.013$ $x_{10} = 1444.490$ $x_{11} = -758.946$	$x_{12} = 148.877$ $x_{13} = 415.360$ $x_{14} = 2315.628$ $x_{15} = -4353.894$ $x_{16} = 1350.169$
Enthalpy (kJ/kg)	$y_1 = -1.735 * 10^4$ $y_2 = 2.859 * 10^4$ $y_3 = -1.091 * 10^4$ $y_4 = 8.550 * 10^3$	$y_5 = -1.440 * 10^4$ $y_6 = 5.550 * 10^3$ $y_7 = -1.382 * 10^3$ $y_8 = 2.386 * 10^3$	$y_9 = -9.349 * 10^2$ $y_{10} = 1.221 * 10^4$ $y_{11} = -1.998 * 10^4$ $y_{12} = 7.485 * 10^3$
Entropy (kJ/kg-K)	$z_1 = -35.737$ $z_2 = 77.5134$ $z_3 = -52.969$ $z_4 = 11.075$	$z_5 = 11.496$ $z_6 = -26.931$ $z_7 = 20.342$ $z_8 = -4.982$	$z_9 = 21.662$ $z_{10} = -40.746$ $z_{11} = 17.533$
Specific heat (kJ/kg-K)	$m_1 = 7.696 * 10^3$ $m_2 = -1.610 * 10^4$ $m_3 = -1.158 * 10^4$ $m_4 = 1.408 * 10^3$ $m_5 = 1.921 * 10^4$ $m_6 = 5.497 * 10^1$	$m_7 = -1.067 * 10^4$ $m_8 = 2.290 * 10^1$ $m_9 = 6.159 * 10^3$ $m_{10} = -4.505 * 10^3$ $m_{11} = 1.080 * 10^3$ $m_{12} = -1.035 * 10^3$	$m_{13} = 1.054 * 10^3$ $m_{14} = -2.988 * 10^2$ $m_{15} = -1.015 * 10^3$ $m_{16} = -6.354 * 10^3$ $m_{17} = 1.507 * 10^4$
Speed of sound (m/s)	$n_1 = 0.916$ $n_2 = 28.607$ $n_3 = -28.949$ $n_4 = -12.062$ $n_5 = 2.126$	$n_6 = 9.547$ $n_7 = 6.876$ $n_8 = -6.763$ $n_9 = -1.119$ $n_{10} = 1.413$	$n_{11} = -0.306$ $n_{12} = 9.356$ $n_{13} = -34.312$ $n_{14} = 24.649$

Property	Coefficients in correlation		
$\left(\frac{\partial \rho}{\partial T}\right)_P$ $\left(\frac{\text{kg}}{\text{m}^3\text{K}}\right)$	$o_1 = -7.049 * 10^3$ $o_2 = 1.402 * 10^4$ $o_3 = -6.975 * 10^3$ $o_4 = 4.386 * 10^3$ $o_5 = -8.768 * 10^3$	$o_6 = 4.387 * 10^3$ $o_7 = -1.208 * 10^3$ $o_8 = 2.428 * 10^3$ $o_9 = -1.222 * 10^3$ $o_{10} = 1.242 * 10^2$	$o_{11} = -2.511 * 10^2$ $o_{12} = 1.272 * 10^2$ $o_{13} = 4.229 * 10^3$ $o_{14} = -8.369 * 10^3$ $o_{15} = 4.144 * 10^3$
$\left(\frac{\partial \rho}{\partial P}\right)_T$ $\left(\frac{\text{kg}}{\text{m}^3\text{MPa}}\right)$	$p_1 = 1.424 * 10^4$ $p_2 = -2.701 * 10^4$ $p_3 = 1.281 * 10^4$ $p_4 = -9.500 * 10^3$ $p_5 = 1.801 * 10^4$	$p_6 = -8.541 * 10^3$ $p_7 = 2.820 * 10^3$ $p_8 = -5.342 * 10^3$ $p_9 = 2.532 * 10^3$ $p_{10} = -3.141 * 10^2$	$p_{11} = 5.946 * 10^2$ $p_{12} = -2.816 * 10^2$ $p_{13} = -8.008 * 10^3$ $p_{14} = 1.519 * 10^4$ $p_{15} = -7.211 * 10^3$
$\left(\frac{\partial H}{\partial P}\right)_T$ $\left(\frac{\text{kJ}}{\text{kg MPa}}\right)$	$q_1 = -1.149 * 10^3$ $q_2 = 1.309 * 10^4$ $q_3 = 5.219 * 10^3$ $q_4 = -9.388 * 10^3$ $q_5 = -4.243 * 10^3$	$q_6 = -2.111 * 10^2$ $q_7 = 9.988 * 10^3$ $q_8 = -6.894 * 10^3$ $q_9 = 1.864 * 10^3$ $q_{10} = -2.505 * 10^3$	$q_{11} = 2.648 * 10^3$ $q_{12} = -8.077 * 10^2$ $q_{13} = -2.361 * 10^1$ $q_{14} = 3.680 * 10^3$ $q_{15} = -1.164 * 10^4$

APPENDIX D

COMPARISON OF PR RESULTS WITH GEOMETRIES OF DIFFERENT LENGTH

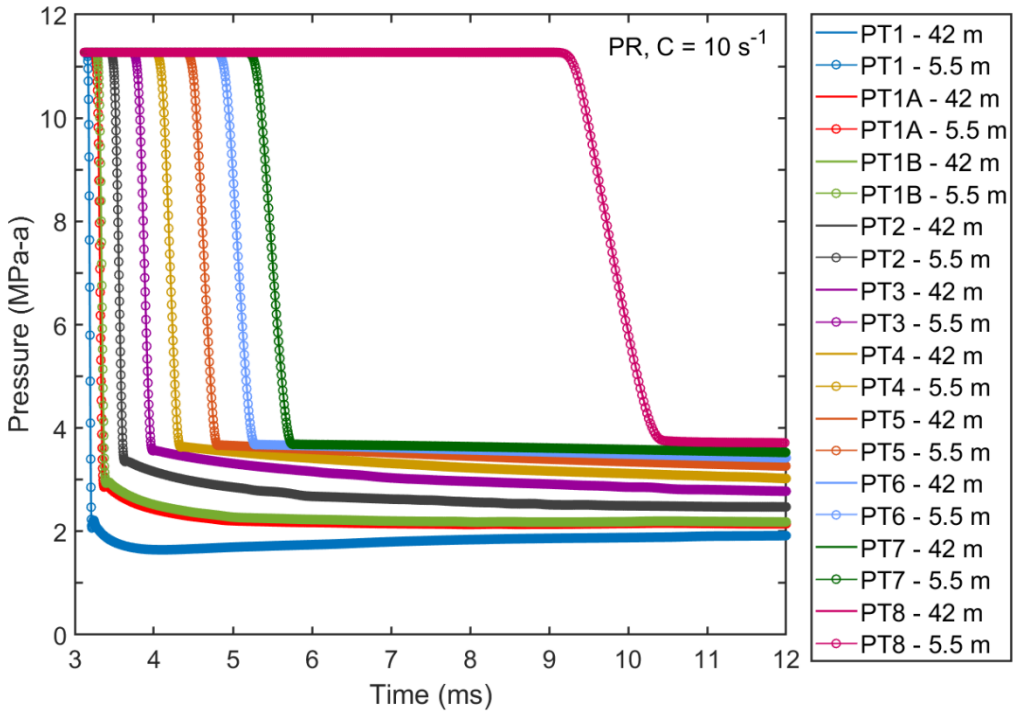

Figure D1. PR: Pressure-time traces with 42 m and 5.5 m long geometries, C=10 s^{-1}.

APPENDIX E

EFFECT OF C ON VAPOR VOLUME FRACTION

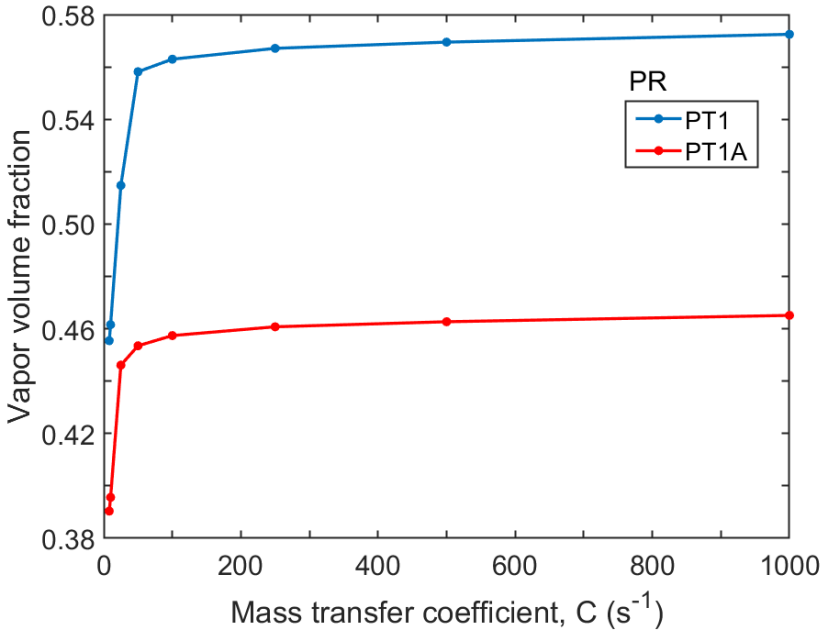

Figure E1. PR: Vapor volume fraction vs. mass transfer coefficient, 10.5 ms.

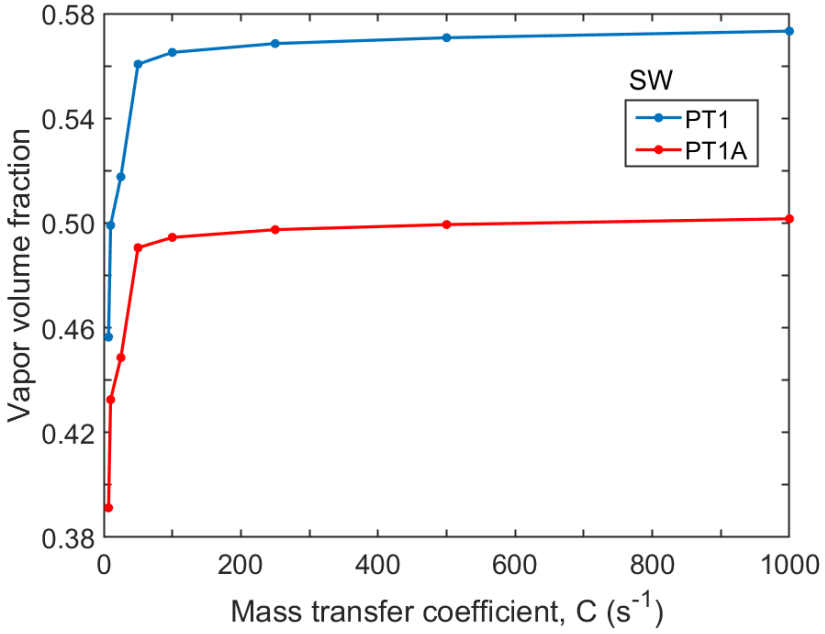

Figure E2. SW: Vapor volume fraction vs. mass transfer coefficient, 10.5 ms.

APPENDIX F

ADDITIONAL PRESSURE-TIME CURVES FOR PENG-ROBINSON MODEL

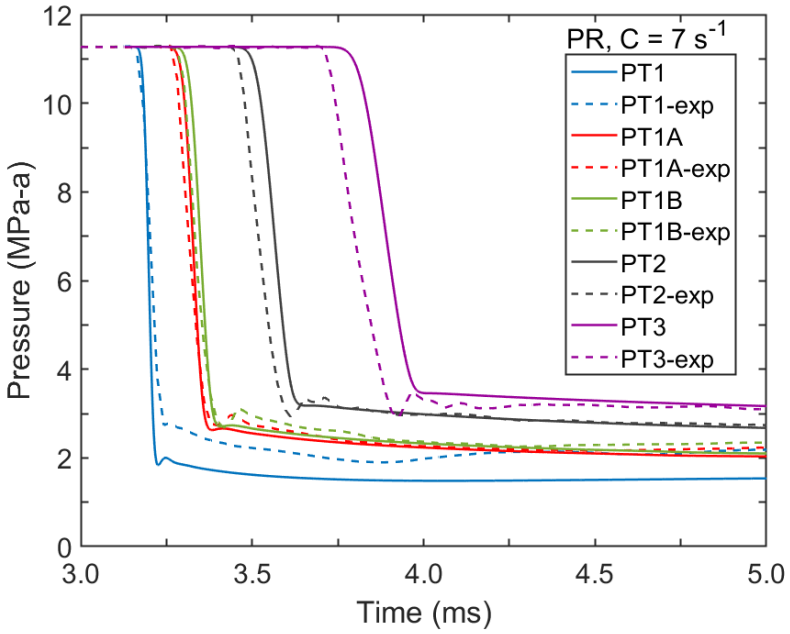

Figure F3. PR: Pressure vs. time, C=7 s^{-1}.

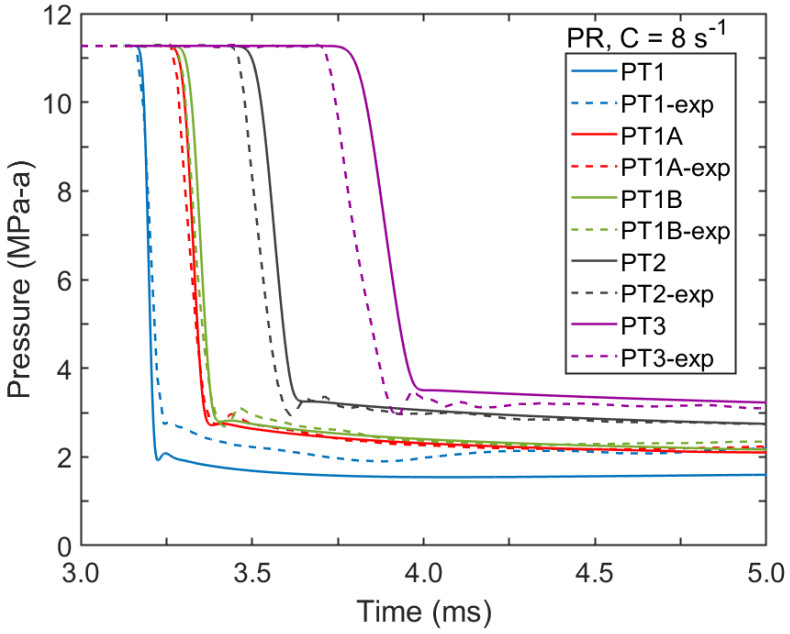

Figure F4. PR: Pressure vs. time, C=8 s^{-1}.

APPENDIX G

ADDITIONAL PRESSURE-TIME CURVES FOR SPAN-WAGNER MODEL

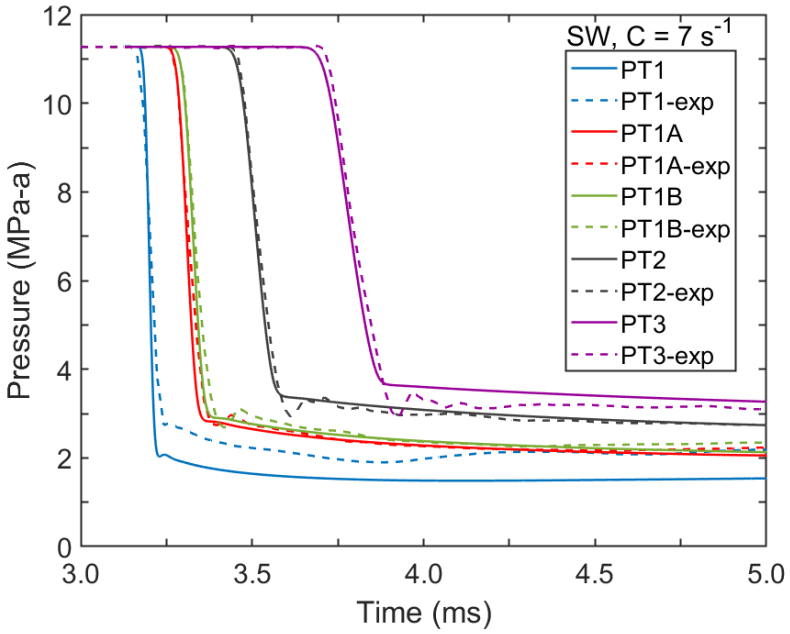

Figure G5. SW: Pressure vs. time, C=7 s^{-1}.

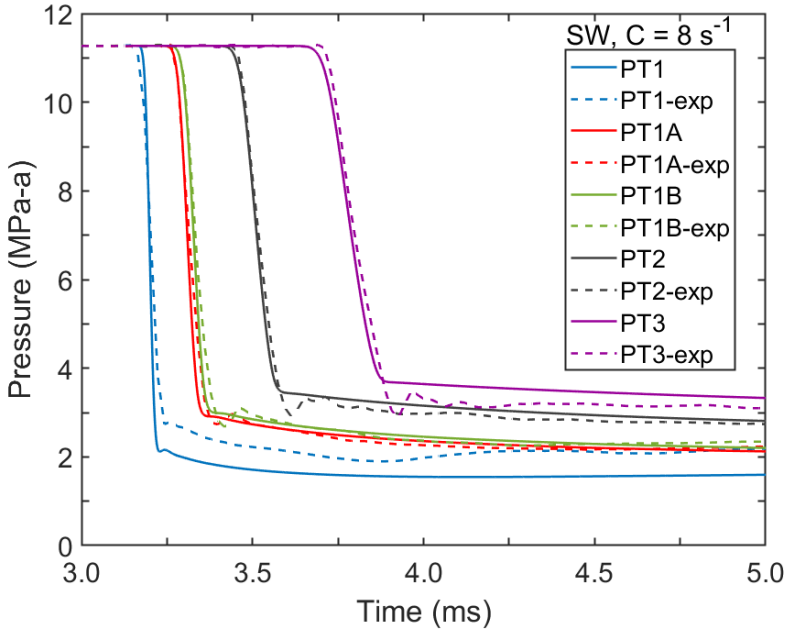

Figure G6. SW: Pressure vs. time, C=8 s^{-1}.